ABSTRACT

Title of Dissertation: DESIGN OF COMPLIANT NONLINEAR ARTICULATED SUSPENSION FOR EXTRATERRESTRIAL ROVING VEHICLES

Charles Hanner
Doctor of Philosophy, 2025

Dissertation Directed by: Professor David Akin
Department of Aerospace Engineering

Designing extreme-access planetary rovers requires advanced articulation mechanisms to traverse rugged terrain, conquer steep slopes, and reduce mission risk. These qualities involve balancing geometric constraints, load distribution, and passive compliance for astronauts on EVA. This dissertation develops a generalizable framework for creating compliant, articulated suspension systems with high degrees of articulation. By closely examining the relationships among kinematics, applied forces, and component-level constraints, the proposed methods address significant gaps in rover mobility research in the areas of systems design, dynamic formulation, and commonly overlooked real-world considerations. In particular, this work demonstrates a holistic approach that integrates quasi-static sum-of-moments tools with Lagrangian-based dynamic modeling and machine learning-driven parameter identification, ensuring robust performance throughout a wide range of operating conditions. The resulting methodology offers a scalable, adaptable framework for future rovers tasked with extreme-access missions.

DESIGN OF COMPLIANT NONLINEAR ARTICULATED SUSPENSION FOR EXTRATERRESTRIAL ROVING VEHICLES

by

Charles Hanner

Dissertation submitted to the Faculty of the Graduate School of the
University of Maryland, College Park in partial fulfillment
of the requirements for the degree of
Doctor of Philosophy
2025

Advisory Committee:
Professor David L. Akin, Chair/Advisor
Professor Craig Carignan
Professor Raymond Sedwick
Professor Michael Otte
Professor William Goldman

Preface

"He's got about two wheels on the ground. There's a big rooster tail out of all four wheels. And as he turns, he skids. The back end breaks loose just like on snow.... Man, I'll tell you, Indy's never seen a driver like this... Hey, that was a good stop. Those wheels just locked."

- Charlie Duke, Apollo 16

Dedication

To Chris Coche and Walter Hanner, whose passions for engineering ignited my own.

Acknowledgments

First and foremost, I must thank Dave for his continual ability to ensure I could stay in grad school, support my degrees, and dream up the multitude of hair-brained schemes I have been able to leap between in my years at the SSL. Your laboratory and your own way of encouragement has enabled me to push my passions into my career spanning from some of the best SCUBA diving there ever may be to spacesuits, habitats, rovers, robots, and just about anything else a space-obsessed young kid could look to the stars and imagine. Thank you.

Mom and Dad, thank you for the unending support and push behind me that kept me going and through the finish line. From Devo to Rusty, you always made sure I had everything I needed to let me do what I needed to do, and do it right. I just kept swimming and somehow we made it. But you saw the path, especially when I couldn't and it's taken a lot from each of us to get here. I sincerely appreciate it and I cannot thank you enough. *Sono Affamato*.

Sean, thank you for introducing me to the world of photography, for which many of my last-minute presentations and conference papers have greatly benefited, even though my hard drive space may not have. Oh, and for being a great brother and supporter.

Chris, thank you for being the person in my life who continually motivates me to work as hard as I possibly can towards the things I want in life. Your endless positivity, encouragement, and understanding self have helped me through each of my struggles in accomplishing this and I hope you know how much I appreciate all you've done for me. I look forward to the coming

years of us finding ways to teach ourselves the things we never knew how to do, and struggling through it together on Facetime.

Romeo and Rahul, I truly have you two to thank for making a large portion of this research possible. Without your software and willingness to support the data collection I needed, and stay up late or show up on weekends to help me get data and run the robots this absolutely would not have happened. But also thank you for being encouraging every time my model spat out nonsense, for leaving many a random thing on my desk, and for acting like the silly unserious friends I sometimes needed to keep the mood light and the project rolling forward. *Hours away* and *my software can support that* are now words I live by.

I must also thank all of the wonderful people (in no particular order) I have had the pleasure of working with over my years at the SSL. Lem, thank you for being the voice that took a chance on me and brought my into the lab. No, I won't stop, thank you very much. Thank you to Kate, Chris, and Nick for being the guiding voices and teaching me how the lab worked and how to write update slides very quickly on a Friday. I have had the great fortune of working with so many fellow graduate students over the years - thank you to all of you.

Some of you fellow grad students I have had the pleasure of seeing at 3:30am just a few too many times, so I fear I must now speak to you directly. Daniil and Nicolas, BioBot (and nearly every single other project I've worked on at the SSL) would not have been possible without you and I sincerely thank you.

There are so many other people that BioBot would not be what it is today without. Thank you to Meredith for being the best suit lead the team could have asked for and a ray of positivity within the project. Thank you Ryan for offering to help every single time you could have, and supporting the absolute best you possibly could.

To the array of undergraduate students who have dedicated their time and considerable efforts to the bettering of BioBot including but certainly not limited to Chandler, Spencer, Rowan, Ian, Robbie, and Wyatt and every other person who touched our project. Each one of you made BioBot better, and have made a lasting impact.

Lastly, thank you to all my friends, fellow graduate students in other labs, and everybody else who I had the opportunity to work, learn, and travel with. To everyone who supported me and encouraged me all these years, I am incredibly thankful.

Table of Contents

Preface ii

Dedication iii

Acknowledgements iv

Table of Contents vii

List of Tables ix

List of Figures x

List of Abbreviations xv

Chapter 1: Introduction 1
- 1.1 Suspension Architectures Review . . . 3
  - 1.1.1 Heritage Suspension Architectures . . . 4
  - 1.1.2 Prototype, Earth-Analogue, and Unflown Active Wheel-Articulation Focused Rover Suspension Systems . . . 7
  - 1.1.3 Suspension Architectures Summary . . . 13
- 1.2 Design Tools and Methodologies For Articulated Suspension Systems . . . 14
  - 1.2.1 Kinematic Simulation and Optimization . . . 15
  - 1.2.2 Spring Damper Inclusive Rover Suspension Analysis . . . 16
  - 1.2.3 Quasi-Static Assumption . . . 17
- 1.3 Earth-Analogue Vehicle Design Approaches for Mobility Systems Testing . . . 18
  - 1.3.1 Similarity Law . . . 19
  - 1.3.2 Equivalent Size, Equivalent Weight . . . 20
  - 1.3.3 Matched Capability . . . 20
- 1.4 Suspension Approaches Summary . . . 21

Chapter 2: System Design and Validation of Independently Articulated Suspension Using a Sum-of-Moments Framework for the BioBot System 24
- 2.1 Introduction . . . 25
  - 2.1.1 Articulating Extraterrestrial Roving Vehicle Concepts . . . 27
  - 2.1.2 Applications Beyond Spaceflight . . . 28
  - 2.1.3 Motivation and Contribution . . . 29
- 2.2 Modeling . . . 30
  - 2.2.1 VERTEX Suspension Development Issues . . . 31
  - 2.2.2 Motivation . . . 34
- 2.3 Method . . . 35

2.3.1 Series Elastic Actuator . . . 37
2.3.2 Parallel Spring (PS) . . . 40
2.3.3 Wheel Force Moment . . . 47
2.3.4 Total System Moment . . . 51
2.3.5 System Optimization . . . 52
2.3.6 As-Built System Upgrades . . . 56
2.4 Force Sensing and Validation . . . 60
2.4.1 Load Cell Integration and Calibration . . . 62
2.4.2 Data Collection and Analysis . . . 63
2.4.3 Operational Characteristics . . . 67
2.4.4 Validation of Kinematics and Regime Transitions . . . 70
2.5 Results and Discussion . . . 71
2.5.1 System Failure Mitigation . . . 71
2.6 Conclusion . . . 75

Chapter 3: Lagrangian Formulation 76
3.1 Introduction . . . 77
3.2 Method . . . 79
3.2.1 Kinetic Energy . . . 85
3.2.2 Non-Conservative Forces . . . 85
3.2.3 Potential Energy . . . 91
3.2.4 Compliance Mechanism Considerations . . . 100
3.2.5 Lagrangian Approach Summary . . . 104
3.3 Applied Kinematics . . . 106
3.3.1 Potential Energy - Gravity Offset Springs . . . 106
3.3.2 Sprung, Unsprung, and Swingarm - K.E. & P.E. . . . 107
3.3.3 Potential Energy - Series Elastic Element . . . 112
3.3.4 Non-Conservative Forces - Reaction Moments . . . 115
3.3.5 Non-Conservative Forces - Damping . . . 116
3.3.6 Bushing Contributions . . . 118

Chapter 4: Validation and System Improvement 122
4.1 Model Validation . . . 123
4.1.1 Quasi-Static Experiment . . . 123
4.1.2 ML-Based Parameter Identification . . . 127
4.1.3 Dynamic Validation . . . 136
4.1.4 ML-Based Optimization . . . 147

Chapter 5: Conclusions and Future Work 152
5.1 Contributions . . . 152
5.2 Lessons Learned . . . 153
5.3 Future Work . . . 155
A.1 Suspension Parameters . . . 158

Bibliography 161

List of Tables

2.1 Condensed table of slope statistics from the Lunar Surface Data Book's Example EVA Traverses. A = 7.3.1 Large Logistics Transfer, B = 7.3.2 Long Uncrewed Science Traverse, C = 7.3.3 Traverse into crater/PSR Table 0-3, D = 7.3.12 Traverse Table 0-4 29
2.2 Roll and pitch statistics from dataset in Figure 2.29 65
2.3 Variability between each swingarm range of motion. FR = Front Right, FL = Front Left, RR = Rear Right, and RL = Rear Left 65

3.1 Variables in Figure 3.4 from left to right 83
3.2 Regimes for the Lagrangian formulation based on pivot motion, crossover, and tension conditions. 105
3.3 Frame assignment logic for the reference frames as shown in Figure 3.15 112

1 Parameters used for the `Rover` class. 158
2 Parameters used for the `Prismatic_SEA` class. 159
3 Parameters used for the `Gravity_Offset_Spring` class. 160

List of Figures

1.1 SSL's Raven rover, built as an astronaut transport rover for analogue field testing. 4
1.2 BioBot during initial field testing on the UMD campus 4
1.3 US Patent No. 4,840,394 "ARTICULATED SUSPENSION SYSTEM" - held by NASA. Precursor suspension system to traditional rocker-bogie [2] 5
1.4 JPL's Mars Exploration Rover in testing, featuring Rocker-Bogie suspension [3] . 5
1.5 Lunokhod-1 annotated mockup vehicle [13] 6
1.6 Lunar Roving Vehicle mobility subsystem drawing [14] 6
1.7 NASA's VIPER rover demonstrating suspension articulation, leveling chassis on a rock in a testbed [18] 7
1.8 NASA's Resource Prospector active suspension with passive spring damping [20] 8
1.9 Annotated drawing of NASA's Chariot suspension system [21] 8
1.10 Articulating chassis design of the CMU Nomad rover [24] 9
1.11 CMU's SCARAB rover conforming to terrain during field trials [25] 9
1.12 Annotated diagram of the active SherpaTT suspension system [26] 10
1.13 Large articulation range of motion, hydraulically-driven, wheel concept for off-road logger/loader [29] 11
1.14 AWLFC concept showing a separated, active articulated rocker-bogie style logging suspenison concept [30] 11
1.15 Marsokhod rover in testing with NASA AMES [31] 11
1.16 Annotated drawing of the EX1 suspension design, featuring passive spring damping combined with a rocker suspension system. 12
1.17 Side profile of the VERTEX rover carrying the umbilical-tending arm (ARMLiSS), featuring it's high range of motion articulated suspension system with passive spring damping 14
1.18 ExoMars-style rover within the DRL ROT[41] 15
1.19 Lumped-parameters spring/damper model for LRV analysis [17] 16
1.20 Articulating suspension design, based on a 4-bar linkage - utilizes a linear assumption in the suspension analysis presented [51] 16
1.21 Nonlinear spring integration example with a swingarm-based suspension system [56] 17
1.22 Spring-damper drawing of the VERTEX suspension system 17
1.23 1/3 scale model of a rocker-style suspension rover [64] 19
1.24 Linear suspension model use in a scaled-rover context [65] 19
1.25 NASA's Chariot, a full-size analogue vehicle, in testing with two test subjects [21] 21
1.26 BioBot during testing with a test subject connected to the umbilical, ready to begin a surface traverse simulation 21

2.1 BioBot driving in a field with the umbilical-tending manipulator deployed to a nominal walking state. VERTEX drives alongside the test subject as they walk along a preplanned route. 25
2.2 VERTEX roving vehicle side profile showcasing suspension system. The fully independent suspension features a series-elastic actuator with a parallel dual-rate spring damper. 26
2.3 VERTEX first suspension system diagram. Note the suspension rotates a swingarm that which the linear actuator and gas strut are mounted on to achieve the range of motion. 31
2.4 Initial suspension system during preliminary VERTEX build stages with the first suspension system. 32
2.5 Example scenarios moving from negative to positive swingarm angle showing variability in sine losses between the gas strut and linear actuator. The swingarm is shown from left to right in this plot, moving from a 'low' position (as seen in Figure 2.3) to a 'high' position (as shown in Figure 2.4). The gas spring force and lever arm used to calculate its moment contribution are depicted in the image. 33
2.6 Sine loss effect on the moment the gas strut produces about the swingarm's pivot. 34
2.7 Spring-damper diagram of final BioBot suspension configuration. Labeled components: A) Series-elastic element, B) Linear actuator, C) Dual-rate spring system, D) Swingarm. Swingarm is at 0°, level with the chassis. Positive direction indicated by arrow around swingarm pivot. 36
2.8 Series elastic actuator side profile, with force path from elastic element to swingarm illustrated including sine loss angles and fulcrum lever arms at an example swingarm angle. Retention mechanisms to resist tension loading additionally present. 38
2.9 Maximum series-elastic actuator moment contribution across all swingarm angles 40
2.10 Maximum moment contribution as a function of preload and spring rate in the series-elastic element. 41
2.11 Deflection of the integrated dual-rate spring damper with finalized settings. . . . 43
2.12 Spring force and moment sum of the as-integrated dual-rate spring damper across swingarm angle 44
2.13 Sensitivity of the moment curve across a variety of preload (in) settings. 44
2.14 Effect of changing crossover (in) on the dual-rate spring damper moment sum . . 45
2.15 Bottom spring rate (lbf/in) adjustment effect on dual-rate moment contribution . . 45
2.16 Top spring rate (lbf/in) adjustment effect on dual-rate moment contribution 46
2.17 CAD drawing depicting the wheel position at maximum extension of the caster angle adjustment system 47
2.18 VERTEX rover during its first field excursion, showing the caster angle adjustment system is in its minimum angle state. 49
2.19 VERTEX at steady state on flat ground demonstrating a single wheel lift configuration 50
2.20 Total moment sum of the suspension model with the 200/400 lb-in rate dual-rate parallel spring damper integrated. 51

2.21 Generalized coordinates used to define component placements in the optimization scheme. The A, B, C labels correspond to the diagram in Figure 2.7, with the "U" subscript corresponding to upper mounting points, and "L" subscript to lower mounting points. (x, y) coordinates are measured from the swingarm pivot, and l coordinates are lengths measured down the swingarm from the same point. 53
2.22 Close perspective of the arrangement of the series-elastic elements on the VERTEX suspension system. For system compactness, these elements were placed offset of the main suspension plane and require careful consideration to ensure the nominal ranges of motion are not compromised. 54
2.23 Comparison between the best single-rate spring replacement and the best dual-rate spring replacement results. 56
2.24 Dual rate spring modification exhibiting lack of rebound and controllability at steady state conditions due to higher than expected sprung mass during electronics integration phase. Top rate 150 lb/in, bottom rate 200 lb/in. Increasing the dual-rate damper's preload returned the system to positive static stability. 57
2.25 Heavy chassis modifications required for upgraded suspension including removal of old structure and welding of new supports to support dual-rate spring dampers. 59
2.26 Chassis after modification to remove old mounts and create new structure 60
2.27 Compression/tension load cell sensor replacing the series-elastic element in the VERTEX suspension system 61
2.28 Calibration curve for transforming recorded voltages from the load cell and amplifier to forces exerted on the cell. The red Galil curve recorded voltages from the onboard Galil motion control system, and the blue Fluke curve used manually measured and recorded values from a Fluke 117 multimeter. 62
2.29 Subset of data collected on an experiment run, cycling the chassis between maximum and minimum height while maintaining as low pitch and roll values as possible. Note that startup and shutdown transients have been removed from the beginning and ending of the approximately 300 second run. In the labeling, "FR" designates the "Front Right" suspension corner, and "SW" abbreviated for "Swingarm". 64
2.30 Overlaid angles and angular rates for all four swingarms plotted across time from the dataset shown in Figure 2.29. FR = Front Right, FL = Front Left, RR = Rear Right, and RL = Rear Left 66
2.31 2D plot depicting relationship between swingarm angle and swingarm velocity, colorized by force experienced by load cell. Positive force is tension, and negative force is compression. 67
2.32 Strut length for the original gas struts plotted across swingarm angle showing varied rate in length change as swingarm travels upwards 68
2.33 Wheel moment and parallel spring-damper moment plotted together. Wheel moment is inverted to more clearly see the point of transition where the series-elastic actuator does not provide counteractive force to the wheel-moment and instead is placed under tension. 70
2.34 VERTEX suspension system at steady state with both series elastic elements removed from the vehicle's right side. This indicates the point of no-load in the series elastic element, and the point of transition between tension/compression. . 72

2.35 VERTEX during a crane lift to remove vehicle from trailer. 73
2.36 Failure of the linear actuator structural housing after crane lift. The two pieces of the linear actuator are highlighted within the ellipses. 74

3.1 BioBot concept during first field trial 78
3.2 VERTEX suspension system high-level diagram 81
3.3 BioBot alternate vide 82
3.4 Variable-Labeled BioBot Suspension Illustration 83
3.5 CG allocation diagram 84
3.6 Ground force vector decomposition to moments about the generalized coordinate 87
3.7 Stribeck's curve "Coefficient of friction (Reibungskoeffizienten) versus revolutions per minute (Umlaufe in 1 min) at different loads (T = 25° C, dia shaft = 70 mm, P_{Geom} = 0.1–2.0 MPa, oil for gas powered engines $\eta \approx$ 180 mPa s)." [79] . . 88
3.8 Illustration showing a set of example example linear, progressive, and digressive profiles [80] 89
3.9 Labeled photo of the gravity offset damper from Radflo Suspension Technology, Inc. 92
3.10 Gravity offset system near crossover point 94
3.11 Bushing elements shown in a perspective image of the suspension system. The bushings are seen at the top and bottom connectors for the series elastic element and at the central pivot point between the linear actuator and the SEE. 97
3.12 Flowchart for selecting which Lagrangian equation to use 105
3.13 Diagram of pertinent frames for the gravity offset spring system. 108
3.14 Frame assignments for the sprung and unsprung mass 109
3.15 Frame assignments for the series elastic actuator system 121

4.1 Load cell integration into the front-right suspension system on VERTEX, replacing the series elastic element. 124
4.2 Initial diagram comparing load cell sensed force (colored points) with predicted force in the series elastic element (black curve). Colorization of the points shows a force hysteresis is present and is dependent on swingarm velocity direction. . . 125
4.3 VERTEX's right side with no series elastic elements installed on the front and rear suspension while investigating the no-load condition. 126
4.4 Initial NN model attempt relying on forming multipliers for each numerical suspension parameter and bounding within a set multiplier boundary, shown as 0.1 in this example. 129
4.5 Final curve-matching result from using the ML approach to identify vehicle parameters 133
4.6 Magnified section of Figure 4.5 focusing on the transition region as the system nears crossover 134
4.7 Position of new equivalent swingarm tip position as indicted by the minimum loss result, overlaid to approximate scale onto as-built swingarm photo 136
4.8 Experimental setup for generating an approximate impulse-response scenario under driving conditions. VERTEX as pictured is in an abnormally high driving position. 137

4.9 Encoder mounting on swingarm pivot . . . 138
4.10 FR swingarm angle data pre-filtering, used for tuning model damping values. . . 139
4.11 Dataset from Figure 4.10 after outlier filtering . . . 139
4.12 Best fit for the training set of data found using the Ray-based optimization scheme in Python. The blue line shows filtered encoder data recorded onboard the BioBot rover, whereas the red line showcases the optimizer's best attempt at fitting the nonlinear dynamics to the real data by varying damping characteristics and the initially-applied step input. . . . 141
4.13 An early, not well fit optimization run with the old $\dot{\theta}$ impulse strategy - note the highly linear displacement trend in the first $\sim$0.15 seconds compared to the accelerative rise shown in the true data. In this case, the light blue data showcases the same training dataset as shown in Figure 4.12 and the magenta color shows the early simulated response. . . . 142
4.14 Test data run using same settings as identified in Figure 4.12, with parameter-based optimization for the step impulse magnitude and duration. . . . 145
4.15 Curve match to a set of partial dataset recovered from a run . . . 146
4.16 A third test dataset showing limitations of the model's ability to match to recorded curves, indicating further investigation into the nonlinear damping characteristics is needed. . . . 147
4.17 Spring rates over epochs during setting optimization run . . . 150
4.18 Improved force profile from ML-output settings plotted with the maxima and minima of the old settings . . . 151

5.1 BioBot. . . . 157

List of Abbreviations

ARMLiSS	Active Rover Mounted Life Support System
ATHLETE	All-Terrain Hex-Legged Extra-Terrestrial Explorer
CG	Center of Gravity
CMU	Carnegie Mellon University
EVA	Extravehicular Activity
JPL	Jet Propulsion Laboratory
KE	Kinetic Energy
LTV	Lunar Terrain Vehicle
NASA	National Aeronautics and Space Administration
PE	Potential Energy
PLSS	Portable Life Support System
SSL	Space Systems Laboratory
UMD	University of Maryland
VIPER	Volatiles Investigating Polar Exploration Rover
VERTEX	Vehicle for Extraterrestrial, Research, Transportation and Exploration
xEMU	Exploration Extravehicular Mobility Unit

Chapter 1: Introduction

Exploring planetary surfaces often involves traversing highly uneven terrain, supporting large or shifting payloads, and mitigating the risks associated with steep slopes. Rover suspension systems must not only provide adequate terrain adaptability, but also meet mission constraints in power, mass, and reliability. This dissertation focuses on suspension architectures that combine active articulation with passive spring damping, an approach that can significantly increase mobility and operator comfort while preserving slope compensation and load distribution advantages.

This dissertation specifically addresses the creation of a new design path and optimization of such suspension systems in high nonlinearity regimes, using developed methodologies that range from quasi-static sum-of-moments-based design to Lagrangian dynamics approach focused in tackling real-world considerations, and machine-learning-enabled parameter identification and optimization. The result is a cohesive framework that can be extended to many roving vehicles, including both Earth-analogue prototypes and future off-world platforms.

Rovers with actively articulated suspensions, especially those that incorporate passive spring damping, demonstrate advantages in slope compensation, high-speed traversal, and occupant/payload comfort. However, including damping introduces mechanical and analytical complexity to traditional rover design paths, specifically in the realm of nonlinear geometry. Conventional linearized

or kinematics-based methods are most often used in rover suspension design, but struggle to cohesively handle complex suspension systems like the experimental rover presented in this dissertation, VERTEX (Vehicle for Extraterrestrial Research, Transportation, and EXploration).

In this dissertation, a comprehensive analysis of suspension architectures is followed by a discussion of existing computational tools for rover design, highlighting where a quasi-static sum-of-moments method can fill gaps in early-stage system design. The dissertation then explores dynamic modeling using a Lagrangian-based formulation focusing on tackling real-world assumptions often made, using a machine learning (ML) approach for parameter identification and settings optimization of in-house-fabricated hardware. The VERTEX rover serves as a working platform to validate these concepts.

VERTEX is the roving vehicle component of the BioBot system. BioBot is an astronaut-assistance concept comprised of: **(1)** a highly-capable roving vehicle (VERTEX), **(2)** an umbilical-tending manipulator (named ARMLiSS - Active Rover Mounted Life Support System), and **(3)** a spacesuit with a variable-duration portable life support system (PLSS). The main goal of BioBot is to offload portions of the PLSS onto the roving vehicle and provide water, power, air, data, and communications to the astronaut through an umbilical in response to the growing expected mass of the xEMU (Exploration Extravehicular Mobility Unit). For more detail on the specific details behind the BioBot application case, please see the previous publication Hanner et al. [1].

This dissertation advances the design, modeling, and optimization of compliant articulated rover suspensions through three major contributions. First, a computationally efficient design approach was established, relying on quasistatic equilibrium and moment-based analyses to capture the large articulation angles often demanded by extreme-access rovers, applied to the BioBot vehicle. This framework focused on vehicle design for early stage space systems by systematically

assessing the suspension geometry and force profiles while retaining sufficient fidelity to ensure reliable performance in a wide range of operating regimes.

Second, a universal Lagrangian-based modeling approach was formulated to integrate both static and dynamic behaviors in rover suspensions. This approach explicitly incorporates real-world complexities such as damper force limitations, non-linear spring-damper relationships, and the inclusion of system bushings. Experimental validation on the VERTEX rover highlighted the model's ability to fully capture system responses, providing a versatile baseline to refine and predict highly nonlinear and compliant suspension performance.

Finally, a data-driven framework was introduced to reconcile the differences between the designed and as-built hardware. By incorporating machine learning algorithms into the identification efforts of the system, the presented method refines the parameter estimates to reflect the manufacturing variants and the true operational characteristics. The resulting approach was then applied to optimize BioBot's suspension system, producing a more linear force profile at the component level with reduced peak loads.

1.1 Suspension Architectures Review

Suspension systems play a critical role in planetary surface rovers as they directly influence a vehicle's stability, payload capacity, energy efficiency, and adaptability across varied terrains. In general, rover suspension systems can be classified by two Boolean characteristics: **(1)** presence of active articulation and **(2)** presence of passive spring damping. For example, a vehicle where both of these propositions are false would directly mount wheels or tracks to the vehicle chassis. The Raven vehicle built at the University of Maryland (UMD) Space Systems Laboratory (SSL)

as seen in Figure 1.1 is an example of this class of rover and has advantages in simplifying design, but limiting speed of travel and adaptability to terrain. In contrast, actively articulated suspensions with spring damping can enhance slope compensation and occupant comfort for a trade-off in system complexity, as shown with BioBot in Figure 1.2.

Figure 1.1: SSL's Raven rover, built as an astronaut transport rover for analogue field testing.

Figure 1.2: BioBot during initial field testing on the UMD campus

This dissertation aims to provide an analytical framework for designing and optimizing actively articulated suspension systems inclusive of passive spring damping, largely regardless of the selected articulation mechanism.

1.1.1 Heritage Suspension Architectures

Within the articulated and spring-damping categories, specific design decisions such as rocker vs. rocker-bogie or fully independent vs. multibogie must be aligned to mission requirements for mobility, load capacity, and reliability. The historic population of suspension design architectures from both flight missions and ground test rovers shows a notable evolution in suspension designs and objectives over time.

1.1.1.1 Rocker-Bogie Suspension

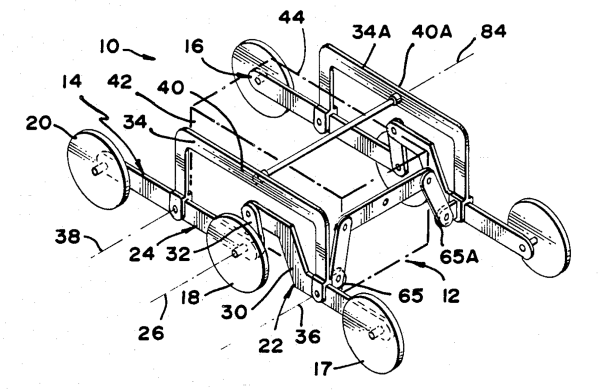

Figure 1.3: US Patent No. 4,840,394 "ARTICULATED SUSPENSION SYSTEM" - held by NASA. Precursor suspension system to traditional rocker-bogie [2]

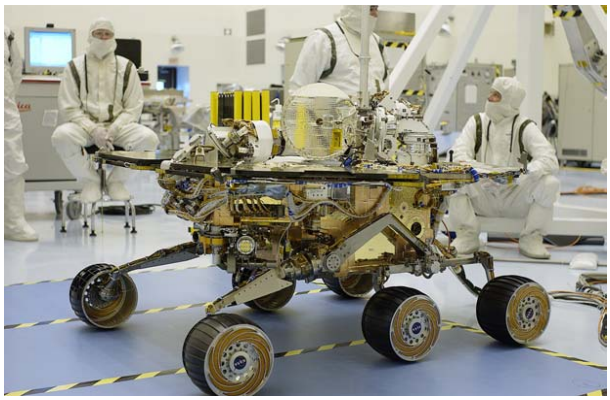

Figure 1.4: JPL's Mars Exploration Rover in testing, featuring Rocker-Bogie suspension [3]

Rocker-bogie suspension systems are the most prevalent type on vehicles deployed in extraterrestrial environments. NASA's Sojourner (1996) [4], Mars Exploration Rovers Spirit and Opportunity (2003) [5], Mars Science Laboratory: Curiosity (2011) [6], and Mars 2020: Perseverance (2020) [7] each feature a 6-wheeled rocker-bogie design. China's Yutu series of lunar rovers also adopt rocker-bogie [8–10]. A passive differential mechanism helps maintain continuous wheel contact and balanced loading at low speeds [11].

China's Zhurong Mars rover, launched in 2021, features a combination "active / passive" rocker-bogie suspension system. The design incorporates a clutch-operated angle adjustment mechanism, enabling operational freedom to modify the vehicle's kinematic configuration. Specifically, this allows for raising and lowering the rover chassis, adjust the distance of the front wheels with respect to the bogie, and altering the front wheel height all using the traction motors. This adjustability diversifies locomotive strategies and improves obstacle climbing performance

in varied terrain [12].

1.1.1.2 Independent Wheel Suspension

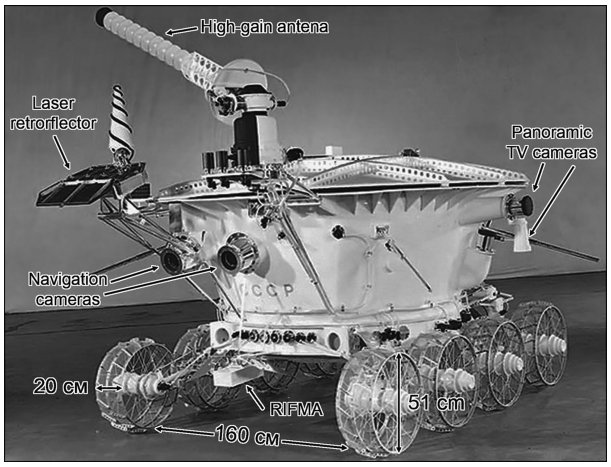

Figure 1.5: Lunokhod-1 annotated mockup vehicle [13]

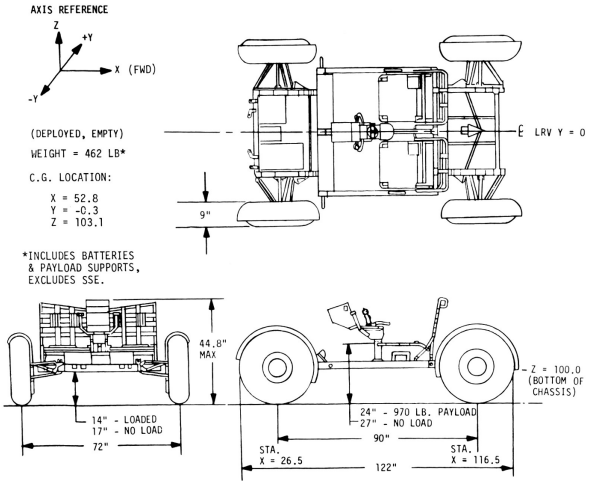

Figure 1.6: Lunar Roving Vehicle mobility subsystem drawing [14]

Russia's Lunokhod-1, as seen in Figure 1.5, launched in 1970 and featured a non-adjustable, elastic eight-wheel independent suspension employing torsion bars with an auxiliary ninth wheel for slip measurement [13, 15]. Lunokhod-2 followed in 1973, improving traction drives and achieving an extraterrestrial traverse record of 39 km in 4 months, only surpassed by Opportunity after a decade of driving [16]. Meanwhile, the Apollo-era Lunar Roving Vehicle (LRV), as seen in Figure 1.6, used a double-Ackermann steering layout combined with double wishbone suspension with torsion bars [14]. The four-bar linkage of the double wishbone system allows the wheel to respond when disturbed from steady state in a way that can be trivially linearized, simplifying the optimization problem to a series of linear springs and dampers translated into appropriate characteristic values [17].

1.1.2 Prototype, Earth-Analogue, and Unflown Active Wheel-Articulation Focused Rover Suspension Systems

The development of active and articulated rover suspension systems has seen steady growth in recent years. Research in this area has come from national space agencies across the world, university researchers, and corporations such as Venturi Astrolab, one of three providers currently developing LTV (Lunar Terrain Vehicle) concepts for Artemis. The development of prototype, Earth-analogue, and unflown rover systems provides a vital platform for testing and advancing suspension designs that address unique challenges posed by planetary surfaces learned from the experiences of planetary surface vehicles in history. These new vehicles broach innovative solutions to mobility, stability, and terrain challenges leveraging active and/or articulation mechanisms to overcome limitations found in traditional suspension platforms. Some systems balance articulation with passive spring damping; others focus on pure articulation to satisfy mission requirements.

NASA's Volatiles Investigating Polar Exploration Rover (VIPER), a ground-testing model of which can be seen in Figure 1.7, is a four-wheeled vehicle designed with independently articulated suspension alongside independent steering and traction drives. Originally slated to explore the lunar south pole ahead of the Artemis surface missions [19]. As of the time of writing, the future of

Figure 1.7: NASA's VIPER rover demonstrating suspension articulation, leveling chassis on a rock in a testbed [18]

VIPER's launch is still unclear, but no matter the outcome, the rover presents a huge step forward for flight-qualified articulated suspension. VIPER does not possess a dedicated passive spring damping system alongside the articulation, as the roll and pitch control of the chassis is largely focused on ice sample drilling operations. The VIPER team draws an interesting distinction, classifying the 10 Hz bandwidth of the suspension as actuated rather than active, a distinction that BioBot similarly makes. NASA intends to use the articulated suspension as an alternative mode of locomotion, as a mechanism to improve stability margins on slopes by leveling the chassis, and for finer intentional positioning of each wheel [18].

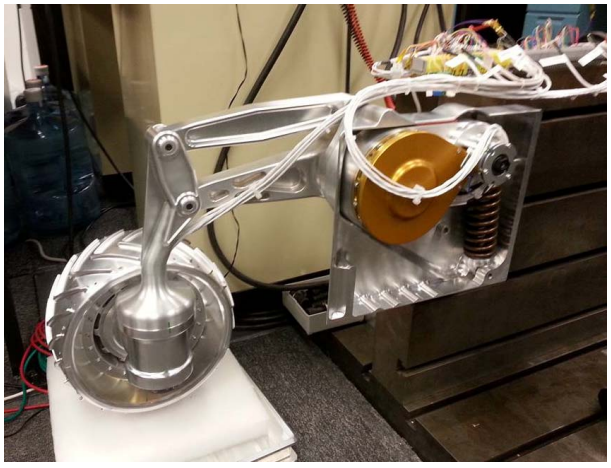

Figure 1.8: NASA's Resource Prospector active suspension with passive spring damping [20]

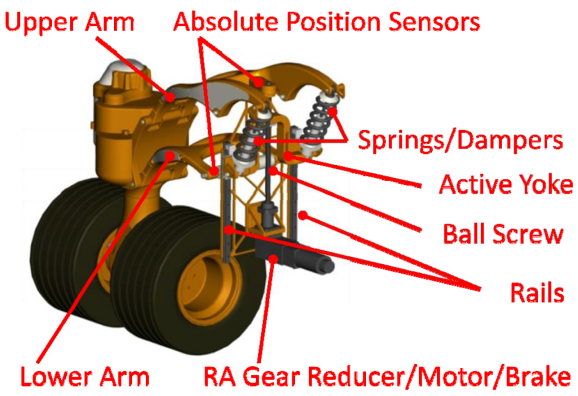

Figure 1.9: Annotated drawing of NASA's Chariot suspension system [21]

NASA's Resource Prospector and Chariot vehicles both have actively articulated independent suspension including passive spring damping. Resource Prospector utilizes a revolute actuator for control of its 4-bar linkage to actively control wheel position, hinged on a spring system as seen in Figure 1.8 [20]. The latter cleverly uses a ball screw instead to articulate the entire suspension mechanism, preserving the spring-damper characteristics in a very consistent way as shown in Figure 1.9. The ball screw mechanism is able to actuate across a range of 25" in vertical travel in just 9 seconds and features 11" of wheel deflection [21].

The Jet Propulsion Lab's (JPL) All-Terrain Hex-Legged Extra-Terrestrial Explorer (ATHLETE) rover uses 6 wheel-on-limb actuators to integrate rolling and walking gaits for greater efficiency during traversal operations on the lunar surface. The system uses a series of revolute actuators to create 6-DOF manipulators to strategically position the wheels and conquer more challenging terrain, setting records in rover suspension articulation range without passive impact attenuation [22].

Carnegie Mellon University (CMU) has developed innovative suspension systems on roving vehicles including the Nomad and Scarab vehicles. Nomad utilizes an expanding wheelbase, as shown in Figure 1.10, to influence the stability margins by creating a wider stability platform for the vehicle, and additionally increases tractive effort when climbing slopes [23]. Nomad also features a body-averaging suspension mechanism. Pivoting alongside the centerline of the chassis, the left and right halves of the vehicle are allowed to articulate, restricted by a differential averaging bar between the sides [24]. This combines active manipulation of stability margins with relatively simple yet effective suspension articulation.

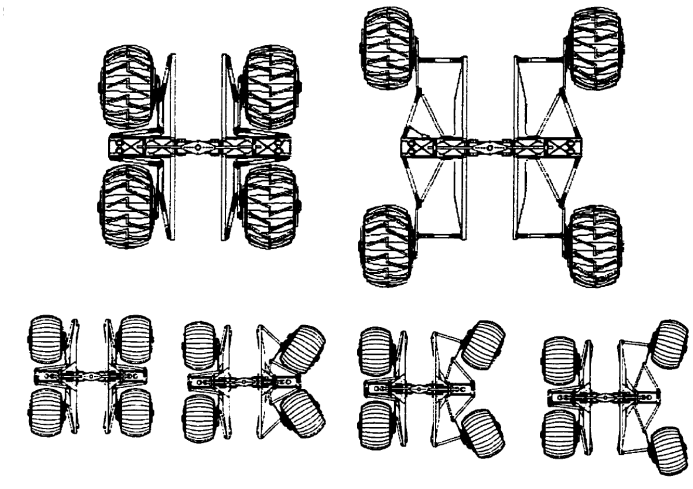

Figure 1.10: Articulating chassis design of the CMU Nomad rover [24]

Figure 1.11: CMU's SCARAB rover conforming to terrain during field trials [25]

CMU's Scarab rover, seen in Figure 1.11, somewhat similar to the ultimate design of VIPER uses an articulated suspension system without traditional spring damping to support stability control and drilling operations, but in a different mechanism. Scarab uses a body-averaging suspension linkage system, similar to Nomad in that the left- and right-hand systems are independent, but with linked front and rear main members on each side. This provides a mechanism for control of chassis roll and body height, and uses skid steer [25].

DFKI's (Deutsches Forschungszentrum für Künstliche Intelligenz) SherpaTT (the evolution from the original Sherpa rover - Figure 1.12) features a wheel-on-limb articulating suspension system, without traditional passive spring damping, that combines hybrid rolling/walking gaits to create a highly efficient and capable exploration chassis. Each of its four limbs use a revolute pan actuator, two linear actuators for effectively hip and knee extension and flexion, and finally a pair of revolute actuators for over-wheel steering and traction drive [26, 27]. A force-torque sensor is placed at each wheel along the wheel drive axis and allows for intentional distribution of force between each wheel [28].

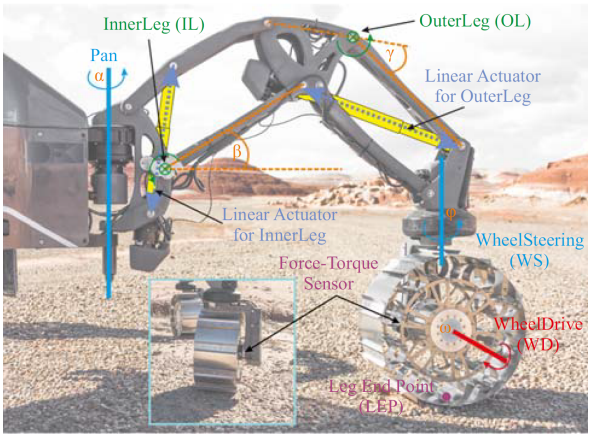

Figure 1.12: Annotated diagram of the active SherpaTT suspension system [26]

In terrestrial applications, forestry equipment uses both articulated body and independently articulated wheels via hydraulics to achieve large ranges of motion and a high degree of terrain compensation [29]. Guaranteed stability from these advantages guarantees stability in the highly variable terrain required to be engaged in forestry, but have little need for passive spring damping

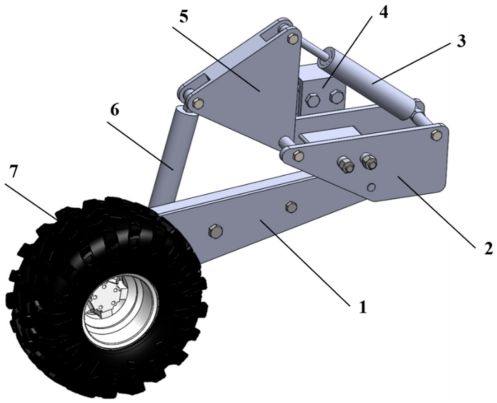

Figure 1.13: Large articulation range of motion, hydraulically-driven, wheel concept for off-road logger/loader [29]

Figure 1.14: AWLFC concept showing a separated, active articulated rocker-bogie style logging suspenison concept [30]

at the slow speeds required from these style vehicles. The availability of hydraulic actuators has allowed for innovative mechanisms to be created such as the Articulated Wheel-Legged Forestry Chassis (AWLFC), combining active four-bar linkage articulation with a separated rocker-bogie [30].

1.1.2.1 Alternate Suspension Articulation Configurations

Beyond the many creative ways in which rovers and terrestrial vehicles have focused on articulation of wheels with respect to the chassis, alternative creative configurations have been developed. One category of this would be articulated body vehicles. The ability to simplify attachment mechanisms between traction (and sometimes steering) actuators to rigid sections of a segmented chassis

Figure 1.15: Marsokhod rover in testing with NASA AMES [31]

may provide an avenue for simplified and stiffer actuation mechanisms. One type of articulated body vehicle is the Marsokhod-style design, which uses roll and pitch mechanisms between the front and rear wheel pairs relative to a central set of wheels to control both the level of the chassis and the steering conditions [**uropean˙space˙agency˙esa˙2012**, 32–35]. This design also allows wheel walking as an alternative locomotive strategy in challenging terrain or anomaly. The vast majority of articulated body platforms built in history are not in roving vehicles, but in the terrestrial mining, forestry, and construction industries, highlighting their adaptability [36]. Specifically, the design is common in dump trucks and in front loaders and rely on hydraulic systems for actuation [37, 38].

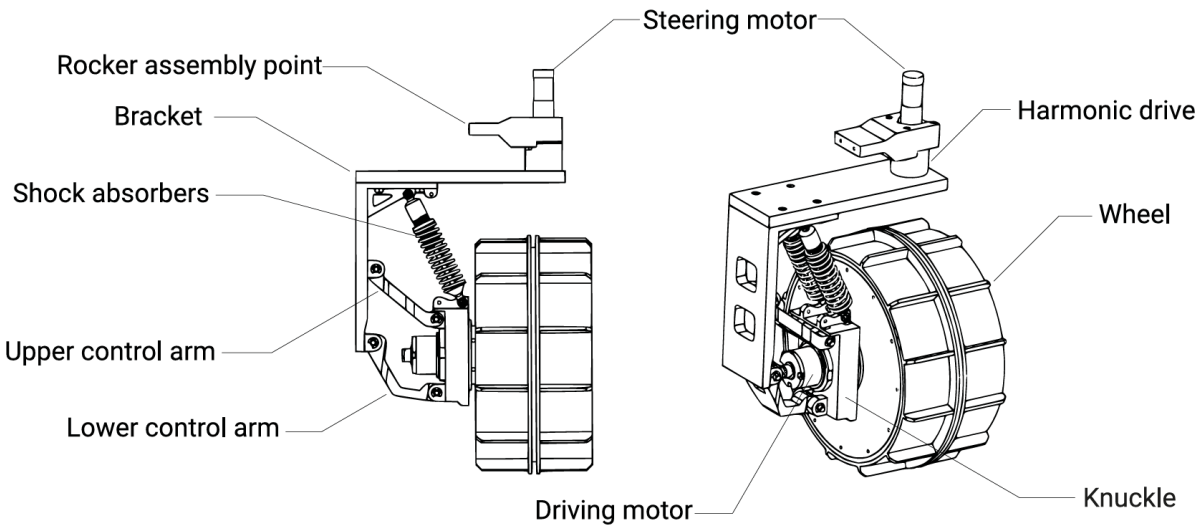

Figure 1.16: Annotated drawing of the EX1 suspension design, featuring passive spring damping combined with a rocker suspension system.

Other unconventional rover suspension design configurations include the EX1 vehicle from Tohoku University's Space Robotics Lab (SRL) in combining a traditional rocker articulation system with independent passive spring-damping suspension per each wheel (Figure 1.16), allowing for a higher traverse speed with lower vibration and harshness [39]. Another vehicle, the FWRA

(Four Wheel Rhombus Arranged) rover both places the wheels in more of diamond shape and utilizes a series of motors, an electromagnetic clutch, and optimized swingarm lengths to perform terrain compensation, allowing new approaches to slope climbing to be developed [40].

1.1.3 Suspension Architectures Summary

These examples highlight broad innovation in suspension systems, from purely kinematic linkages to fully active, compliance-rich articulations. However, no unified approach or previously built rover exists in building a suspension system capable of articulating a chassis to accommodate steep slopes ($\geq 30°$) while including passive spring damping in all configurations. In the coming age of return to human exploration, developing tools and rovers in this trade space is likely to augment more advanced planetary surface research through astronaut support, especially when looking towards metabolic impact of EVAs (Extravehicular Activities) on Mars.

In particular, the SSL's VERTEX rover stands out for its swingarm travel range of 58.8°, combined with passive spring damping for impact attenuation across the full range of motion. The large range of motion allows the vehicle to level its chassis on 40° cross-slopes, 30° upslopes and can raise and lower the chassis by over one meter. The suspension features both a custom series-elastic actuator system and a secondary spring system to offload force requirements from the prismatic joint under Earth gravity conditions. Due to the articulation method and wide range of motion, the system is highly nonlinear, mandating careful considerations of the vehicle's kinematics, sine loss effects, and real-world considerations for components such as tension-limited dampers. This dissertation focuses on the largely on a new 2-part design path taken to design VERTEX's final suspension system, comprised of a systems-level design tool

Figure 1.17: Side profile of the VERTEX rover carrying the umbilical-tending arm (ARMLiSS), featuring it's high range of motion articulated suspension system with passive spring damping

and a fine-detail Lagrangian dynamics scheme. The next sections examine the analytical and computational tools that have been deployed historically, clarifying why new techniques and approaches are necessary for vehicles like VERTEX.

1.2 Design Tools and Methodologies For Articulated Suspension Systems

Substantial prior work emphasizes kinematic optimization for rocker-bogie or other linked suspensions, while certain specialized studies address compliance or soil contact models. Yet for more complicated suspension design paths, these baseline models must be enhanced to manage nonlinear geometry and multi-spring constraints.

1.2.1 Kinematic Simulation and Optimization

Kinematic simulations are the foundation for modern rover suspension analysis. These simulations tend to use a simulated set of varying terrain topologies and often simulate and evaluate varying rover characteristics such as drawbar pull, stability, or load distribution while optimizing a set of vehicle parameters, usually in some form of a distributed-mass model [42–46]. As these types of simulations provide insight into the efficiency of kinematic designs in compensating for these uneven terrains, they focus on systems without dedicated spring-damper mechanisms therefore are largely applied to rocker and rocker-bogie configuration vehicles.

Figure 1.18: ExoMars-style rover within the DRL ROT[41]

The DLR-developed Planetary Rover Optimization Tool (ROT - shown in Figure 1.18) optimizes Rocker Bogie and ExoMars type rovers through geometric variability and includes a distributed mass approach to increase realism [47]. Other DLR-developed analysis tools utilize simulated performance of a vehicle's design to optimize mechanical structure and suspension design parameters [48]. Similarly, advanced simulation schemes that include surface contact dynamics modeling can be used to modify the rocker-bogie parameters of a vehicle with simulated drawbar pull [49]. These models have been validated using deterministic and stochastic parameter estimation methods, establishing correlations between predicted and experimental soil interaction parameters and increasing the reliability of performance simulations used in ve-

hicle design optimization [50]. Combining optimization schemes that are terrain-considerate, terramechanics-informed, contact dynamic tracking, and systems-focused allow rover suspensions to be optimized as a subsystem of a complete rover vehicle, usually looking to decrease system mass or required power [41].

1.2.2 Spring Damper Inclusive Rover Suspension Analysis

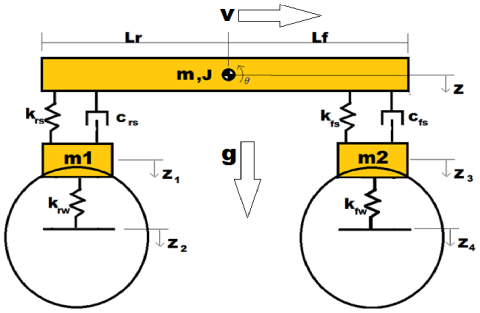

Figure 1.19: Lumped-parameters spring/damper model for LRV analysis [17]

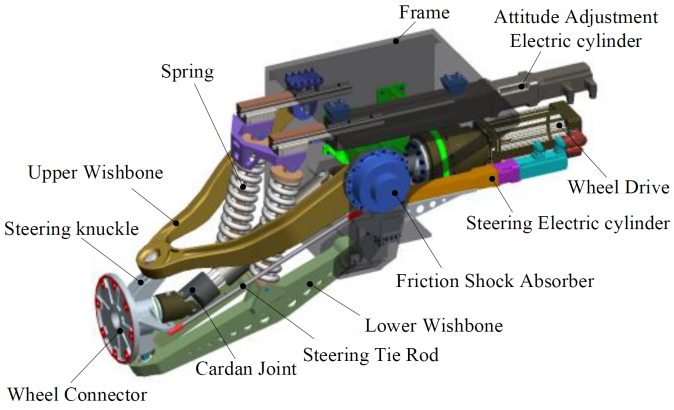

Figure 1.20: Articulating suspension design, based on a 4-bar linkage - utilizes a linear assumption in the suspension analysis presented [51]

Traditional analyses with passive damping often assume linear stiffness and damping [17, 51, 52], valid for short-travel double-wishbone setups. Figure 1.19 shows the traditional lumped parameter linear model that a large majority of sprung rovers use. Some advanced concepts (differential four-bar, parallel linkages, suspended bogies) incorporate partial compliance while targeting continuous wheel-ground contact [53–55].

In contrast, VERTEX's swingarm spans nearly 60°, linking multiple springs and an actuator with potentially large sine losses and tension restrictions. Simple linear approximations are insufficient. Some dynamic models exist for single swingarm-based suspension systems on

rovers [56], and efforts in non-linear components such as inerters or geometry-based compliance [55, 57] show promise but remain application-specific. The design approach presented in this paper accommodates arbitrary suspension mechanism configurations and component placements, provided that the kinematic relationships between the primary suspension axis, wheel position, and the states of individual components—including springs, dampers, and auxiliary joints (with friction)—can be clearly defined and traced.

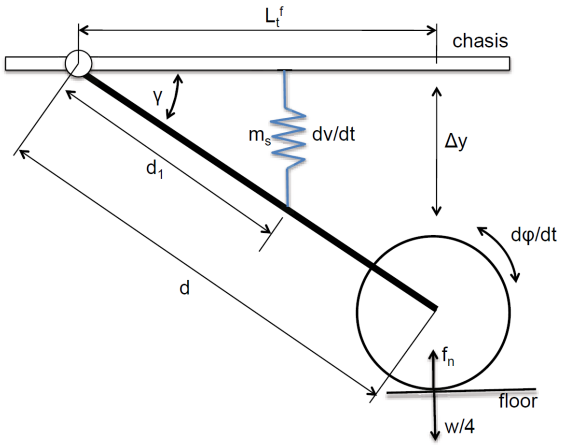

Figure 1.21: Nonlinear spring integration example with a swingarm-based suspension system [56]

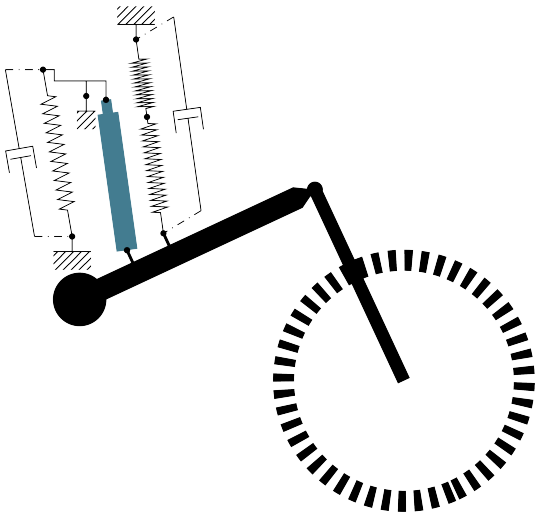

Figure 1.22: Spring-damper drawing of the VERTEX suspension system

1.2.3 Quasi-Static Assumption

Quasi-static analysis assumes that a system moves at a sufficiently slow rate such that inertia and damping effects can be neglected, reducing the problem to one of kinematics and static force equilibrium. This assumption is particularly relevant to planetary rovers, which typically operate at low velocities (leq10 cm/s), making dynamic effects negligible [58]. By treating motion as a sequence of static equilibria, quasi-static models simplify the design and analysis of

articulated suspensions, especially applicable early in the design process.

While quasi-static models effectively characterize slow rover motion, their assumptions become invalid at higher speeds or when transient effects such as impact forces or oscillations arise. The classical rocker-bogie suspension was explicitly designed to function under quasi-static conditions, but emerging high-speed rover concepts require a more detailed treatment of inertia and compliance [59]. When a rover begins to encounter rapid wheel-terrain interactions, dynamic effects dominate, requiring a transition to advanced system modeling [60, 61].

This dissertation adopts a hybrid approach: beginning with a quasi-static methodology for initial system design and transitioning to a Lagrangian framework for detailed dynamics modeling and parameter optimization. The integration of machine learning further refines parameter selection, bridging the gap between theoretical modeling and real-world system identification and optimization.

1.3 Earth-Analogue Vehicle Design Approaches for Mobility Systems Testing

Specifically, looking at the design of flight rovers with suspension systems designed to perform under the gravitational conditions of the moon or Mars, teams must consider how to best test on Earth. Looking beyond gravity-offload mechanisms such as pulleys and suspended masses, which can significantly limit testing, Earth-analogue rovers can be built to preserve specific aspects of a design and allow qualification and characterization efforts to occur in different areas [62]. Most often these vehicles sacrifice selected specific aspect pertinent to the flight vehicle in pursuit of accurate testing of various qualities of mobility; an acceptable trade-off as the focus of the experimentation is in evaluating the mobility system in one way or another. The dif-

ferent approaches to building an Earth-analogue vehicle are dependent on the testing goals and requirements, and the goal of this dissertation is to apply to all three categories.

1.3.1 Similarity Law

The first approach is to use what is known as the "Similarity Law" to scale rover mobility systems to evaluate items such as power consumption and peak torque requirements reflective of the deployed extraterrestrial counterpart vehicle [63]. This scaling factor is effectively the fractionalized ratio of gravity levels between the planetary or satellitic body and the testing gravity condition on Earth [64]. Testing with alternative gravity-level approaches such as half-G parabolic flights (rover for which is shown in Figure 1.23) allow the scaling factors to be doubled and thus reduce the scale proportions between the flight kinematics and the testing vehicle kinematics.

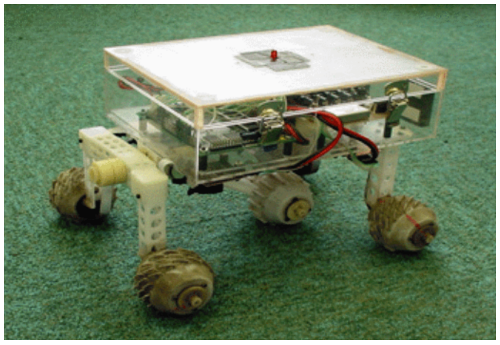

Figure 1.23: 1/3 scale model of a rocker-style suspension rover [64]

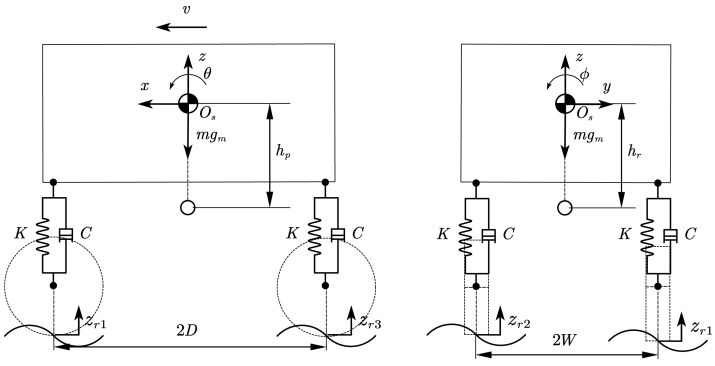

Figure 1.24: Linear suspension model use in a scaled-rover context [65]

This approach has been shown to provide very similar dynamic responses across different vehicle scales as long as the scaling factors are correctly translated into the scaled design parameters, allowing linear models to be easily maintained (example scaled linear model shown in Figure 1.24) [65]. Extending this generalized approach to more complex nonlinear approaches

will augment pathways to a wider variance in testing of extraterrestrial vehicles.

1.3.2 Equivalent Size, Equivalent Weight

The second approach is to maintain the testing vehicle at the same size as the flight version, with the same effective weight as would be experienced on the body of the study's surface. Often, this approach allows the test vehicle to be engineered with a center of mass and wheel force very similar to those of the flying rover, allowing the principles of terramechanics to be validated [66]. An example of this is the VIPER Moon Gravity Representative Unit (shown in Figure 1.7) as it has a ground-pressure equivalent variant that requires a weight offloading tether from the power system and a variant that preserves the center of gravity of the vehicle at the expense of greater wheel loading $\approx 30\%$ [18]. Some approaches within this category prioritize the use of the flight chassis and actuators to analyze mechatronic performance, adaptive control systems, or vehicle stability in flight-like conditions [67, 68].

1.3.3 Matched Capability

The third approach largely focuses on operational testing through the creation of a testing vehicle of equivalent size and equivalent mobility capabilities, thus requiring a higher mass compared to the lunar design. Systems involving the testing of human-related CONOPS in Earth conditions, such as Desert RATS and other analogue field trials, often follow this design approach to allow realistic payloads, slope climbing abilities, and system operations to be tested.

NASA's Chariot rover (Figure 1.25) was designed from the ground up to support Earth-gravity testing of that vehicle design. Tuning the springs, dampers, articulation actuator torques,

gearboxes, structures, etc. all for Earth gravity generates a heavier vehicle than would be needed for the lunar surface, but allows the concepts of operations surrounding that vehicle to be tested in high-fidelity analogue field events [69, 70].

Figure 1.25: NASA's Chariot, a full-size analogue vehicle, in testing with two test subjects [21]

Figure 1.26: BioBot during testing with a test subject connected to the umbilical, ready to begin a surface traverse simulation

BioBot strictly adheres to this design methodology. Maintaining scale is critical for refining the operational concepts that make these roving vehicles unique in paralleling fidelity to the final surface. It is especially important with BioBot to preserve scale as well as slope climbing/leveling abilities to understand how useful an extreme-access roving vehicle can be to supporting EVAs, a difficult task under scaled gravity from the Moon or Mars. Figure 1.26 shows the full scale of BioBot in preparation for an EVA simulation task, allowing the astronaut to walk when they want and drive when they do not.

1.4 Suspension Approaches Summary

Rover suspension architectures have evolved from simple passively articulated configurations to highly active spring-damped solutions designed to handle extreme slopes, loads, and terrain variability. Although historically prevalent systems such as the rocker-bogie favor low-speed

exploration and quasi-static design, emerging concepts for both terrestrial off-road applications and next-generation surface missions push toward higher speeds, greater slope compensation, and more extensive articulation. Such capabilities introduce significant design complexity, especially in nonlinear systems.

This dissertation focuses on bridging gaps in design methodology for these advanced suspensions. It begins by leveraging a quasi-static, sum-of-moments approach to handle early-stage system sizing and trade-offs, then integrates a Lagrangian-based modeling framework to capture higher-speed, real-world dynamics while tackling real-world considerations often overlooked. Finally, it uses machine learning-enabled parameter identification created for parameter identification, model refinement, and system optimization. VERTEX serves as the principal demonstration platform.

The ensuing chapters detail each step in this multi-layered approach, culminating in a flexible design framework that can be applied to a wide array of roving vehicles, ranging from Earth-analogue prototypes like BioBot to future off-world exploration platforms. By unifying quasi-static design, rigorous dynamic modeling, and data-driven refinement, this work aims to ease the path toward rovers that are simultaneously robust, high-performing, and adaptable to the rigorous demands of extraterrestrial terrain.

- **Chapter 2:** Presents the sum-of-moments design methodology in depth, including the original quasi-static models, design decisions, and validation results.
- **Chapter 3:** Introduces the Lagrangian-based dynamic model for articulated suspensions with passive compliance and application within the VERTEX kinematics.
- **Chapter 4:** Describes the ML-based parameter identification framework and shows how

as-built can deviate from as-designed in manufactured hardware, as well as the use of the framework for focused optimization. The dynamic validation method and results for the Lagrangian model are also presented.

- **Chapter 5:** Summarizes results and discusses future work.

Chapter 2: System Design and Validation of Independently Articulated Suspension Using a Sum-of-Moments Framework for the BioBot System

This chapter has been written as a stand-alone paper and is under second review in Acta Astronautica as of thesis submission. Please check for the final version to find any supplementary media or prose adjustments.

Contributions In This Chapter This chapter focuses in the development of a quasi-static computationally-efficient approach for articulated suspension design with passive spring damping. A key assumption is presented in this chapter as the ”full-contribution assumption”, allowing system stability and stiffness to be evaluated very quickly between suspension configurations. The goal in this chapter is to provide a workflow to design these articulated systems in a reliable way that guarantees stability even with nonlinear systems.

2.1 Introduction

BioBot is a versatile Earth-analogue roving vehicle and umbilical-tending manipulator pairing designed, manufactured, and assembled in-house at the University of Maryland's Space Systems Laboratory. The rover component, named VERTEX (Vehicle for Extraterrestrial Research, Transportation, and EXploration), is built to simulate full-duration Extravehicular Activities (EVAs) in Earth conditions, specifically targeting a reduction in astronaut metabolic strain by transferring a majority of the mass of the astronaut's portable life support system (PLSS) onto the vehicle. Figure 2.1 depicts BioBot operating during field trials with a test subject attached via the actively-tended umbilical.

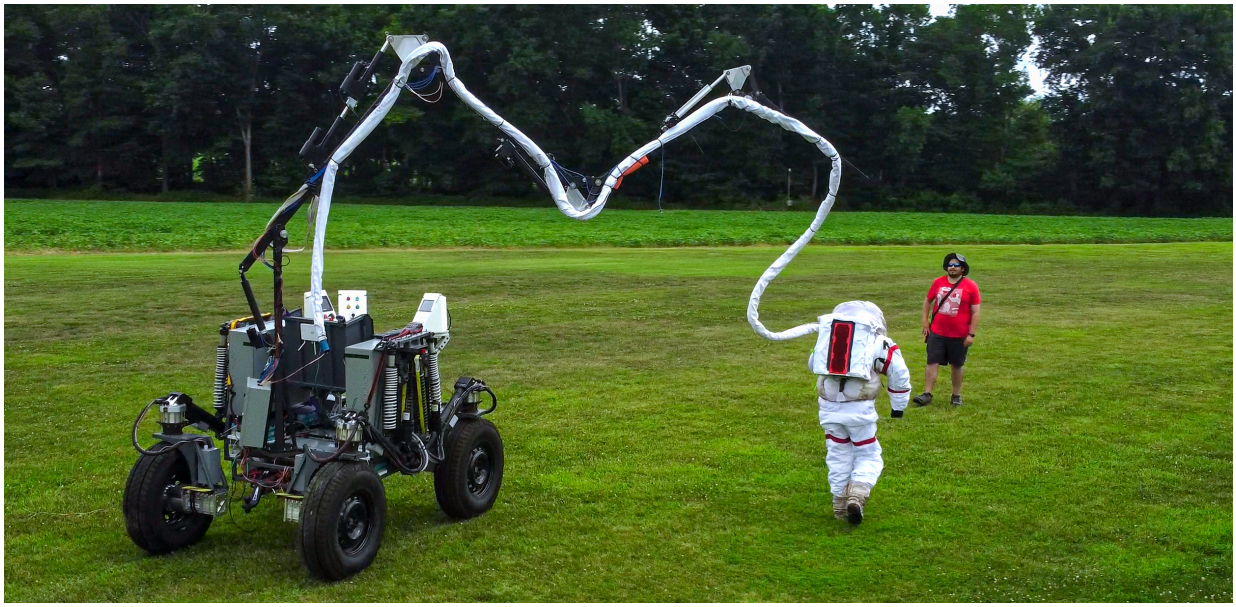

Figure 2.1: BioBot driving in a field with the umbilical-tending manipulator deployed to a nominal walking state. VERTEX drives alongside the test subject as they walk along a preplanned route.

VERTEX is capable of climbing slopes up to 30°, and leveling the chassis on such slopes using a combination of parallel and series-elastic actuator systems. The rover can steer each

wheel independently with a range of $\pm 180°$ and supports a 5-meter-long umbilical-tending robotic manipulator. More detailed information regarding BioBot's design path, methodology, and initial field trials is available in recent work Hanner et al. [1]. Known as the Vehicle for Extraterrestrial Research, Transportation, and Exploration (VERTEX), the rover component is designed for flexibility in field trials, supporting a multitude of payloads and mission configurations across a wide variety of analogue environments.

Figure 2.2: VERTEX roving vehicle side profile showcasing suspension system. The fully independent suspension features a series-elastic actuator with a parallel dual-rate spring damper.

VERTEX has a uniquely broad range of motion among independently articulated planetary surface rovers, featuring a kinematically-limited 58.8° of movement and passive spring damping compliance at all articulation angles. The chassis can compensate 30° in pitch, 40° in roll, and over 1 meter of chassis height variation. This articulating flexibility allows payloads whether

it be an umbilical-tending manipulator, scientific sampling devices, or astronauts to navigate geologically diverse and steep terrains without compromising vehicle stability. Additionally, for particularly challenging payloads such as BioBot's 5-meter long umbilical tending manipulator, requirements for control of its free-spinning yaw joint can be reduced or eliminated through the active pitch and roll control. If unwieldy payloads remain unaffected by slopes, especially important with BioBot as the astronaut is attached to the manipulator arm via the umbilical, safety of the operator and the rover can be better guaranteed and requirements for mounting and control of these payloads can be reduced.

2.1.1 Articulating Extraterrestrial Roving Vehicle Concepts

Articulated suspension systems enable rovers to adapt to and better explore rugged and uneven terrains. NASA's Chariot [21], ATHLETE [22], Resource Prospector [20], and VIPER [18] rovers incorporate independently articulated suspension systems, allowing each wheel to adjust position relative to the chassis for improved stability and mobility. Similarly, academic prototypes, including CMU's Scarab [25], Nomad [23], and DFKI's Sherpa/SherpaTT [26], employ unique articulation systems tailored for specific mission goals such as terrain compensation, stability enhancement, and sampling.

Common to these designs is a focus on articulating wheels relative to the chassis. This approach enables precise adjustments to wheel height and in some configurations steering angle, effecting measurable and intentional positioning of the CG relative to stability margins. In contrast, articulated *body* rovers move entire sections of the vehicle chassis to accommodate terrain. Examples include the Marsokhod series: Lama by Alcatel Space Industries [32], Eve and IARES

by CNES [33], and a Marsokhod rover from NASA Ames [34]. These articulated body rovers utilize roll and pitch control across wheel pairs, relative to central wheels, to achieve effective terrain compensation and steering capabilities. Most of the articulated-body vehicles in existence are focused in mining, forestry, or construction [36]. Often this architecture is commonly present in front loaders and dump trucks, and relies on hydraulic actuators [37, 38].

The EX1 rover from Tohoku University's Space Robotics Lab incorporates passive suspension at each wheel to overcome speed limitations in traditional rocker/rocker-bogie systems. Dubbed the "Mechanically Hybrid Suspension" (MHS), EX1's passive spring damping lowers suspension forces, minimizes harsh impacts, and improves dynamic stability when traversing obstacles [39].

Highlighting the necessity of these terrain-adaptive designs, NASA's Lunar Surface Data Book emphasizes the operational challenges of the extreme-access EVA conditions expected to be seen in the Artemis missions including steep slope navigation, payload management, and crew safety [71]. Table 2.1 shows a condensed overview of slope conditions seen across the four example EVA routes outlined in the document. Working to best prepare roving vehicles to compensate for the large slopes present will likely have positive downstream effects on the success of surface EVA goals, motivating the large articulation range in VERTEX.

2.1.2 Applications Beyond Spaceflight

Articulated suspension systems are equally valuable in terrestrial fields like forestry and construction, where equipment often combines body articulation with independent wheel adjustments facilitated by hydraulic systems. Forestry harvesters and forwarders use such systems to

Table 2.1: Condensed table of slope statistics from the Lunar Surface Data Book's Example EVA Traverses. A = 7.3.1 Large Logistics Transfer, B = 7.3.2 Long Uncrewed Science Traverse, C = 7.3.3 Traverse into crater/PSR Table 0-3, D = 7.3.12 Traverse Table 0-4

EVA	**Max.**	**Mean**	**Std. Dev.**
A.1	9.76°	3.26°	1.88°
B.1	20.51°	5.17°	4.01°
B.2	28.26°	5.24°	4.69°
C.1	28.71°	8.4°	7.15°
C.2	11.66°	3.3°	2.03°
C.3	41.55°	7.8°	6.02°
D.1	23.64°	5.28°	4.03°
D.2	17.5°	5°	3.74°
D.3	36.12°	11.65°	6.91°

prevent tipping on uneven ground under heavy loads [29]. In construction, vehicles like articulated dump trucks [37] and loaders [72] often leverage single-axis body articulation to gain advantages in steering and turning radii. Other construction equipment leverages wheel-articulation for stability advantages, including multi-DOF articulation for walking excavators including hydraulic force sensing [73]. The use of quasi-statics in the design of articulated suspension vehicles is a common approach, and has extensions into both wheeled and tracked sprung suspension systems [74]. A plethora of terrestrial experience with articulating vehicle systems allows for an evolutionary rather than a foundational step in the development of extraterrestrial vehicles.

2.1.3 Motivation and Contribution

Of the articulating extraterrestrial roving vehicle concepts, Resource Prospector and Chariot are the roving vehicles who include both active articulation and passive spring damping in

their design. The decision to include both of these items in the VERTEX rover was focused in the comfort of the operator, and the inclusion of passive spring damping was included as a level 1 requirement. Existing system examples of articulated suspension systems that include passive spring damping do not

The focused contribution of this work is in creating a computationally-efficient, high-level systems analysis framework for the design of nonlinear articulated suspension systems with passive compliance.

This work uses a quasi-static assumption for estimating the stability of the system and is intended to be a first step in the full suspension design process where a more in-depth dynamics-focused approach is undertaken to fine-tune system details and responses. This follow-on work on the creation of a Lagrangian-based dynamic system is shown later in Chapters 3 and 4.

2.2 Modeling

Modeling rover suspension as a quasi-static articulation system allows for the use of a sum-of-moments-based approach [75]. Traditionally, vehicle suspension modeling relies on specialized simulation packages that are not adaptable to the extensive variability in actuators and structural configurations required in early-stage space systems design. Although these packages typically emphasize dynamic responses, the approach used in this generated approach focuses specifically on quasi-static stability, accurate force estimation, and payload support. This quasi-static assumption is justified by the linear actuators selected for the VERTEX project, which exhibit relatively low bandwidth and slow response compared to traditional active suspension actuators. Specifically, VERTEX requires approximately 60 seconds to complete a complete

articulation cycle spanning the $\approx 58.8°$ range of motion.

2.2.1 VERTEX Suspension Development Issues

Initial design requirements highlighted the need for passive spring damping to enhance operator comfort. Prior SSL-built rovers featured rigid suspensions, resulting in uncomfortable operator experiences and motivating the adoption of passive damping for VERTEX. In particular, all three Lunar Terrain Vehicle (LTV) prototype providers contracted in 2024 incorporate passive spring-damped suspensions, with Astrolab FLEX explicitly featuring independently articulated suspension [76]. The inclusion of independently articulated suspension with passive compliance enhances BioBot's applicability to the extreme-access activity foci of the Artemis missions and beyond.

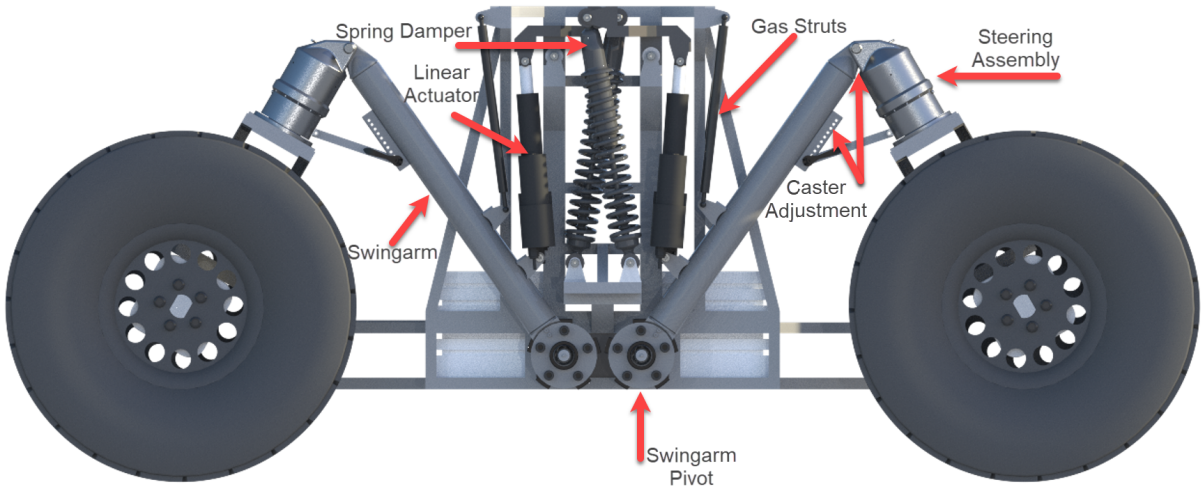

Figure 2.3: VERTEX first suspension system diagram. Note the suspension rotates a swingarm that which the linear actuator and gas strut are mounted on to achieve the range of motion.

The first iteration of VERTEX's articulated suspension system employed force-based modeling, aiming to optimize linear actuator mounting locations to minimize actuator force demands while maximizing suspension range of motion. Initial modeling relied upon preliminary vehicle

mass estimates and assumed a fixed upper actuator mounting point, as the series-elastic part of the system was still under development. The optimization scheme incorporated a pair of 250 lb constant force gas springs (often referred to as ”gas struts”) to offload physical requirements from the linear actuator, allowing faster articulation, lower forces, and reduced cost and is shown in Figures 2.3 and 2.4.

Figure 2.4: Initial suspension system during preliminary VERTEX build stages with the first suspension system.

Testing revealed that while linear actuators could achieve full articulation throughout the specified range, payload capacity varied significantly. At low swingarm angles, with the chassis in a raised position (Figure 2.4), the suspension could support both a test subject and additional payload with stability. However, at higher swingarm angles and lower chassis heights (Figure 2.3), the suspension could support less than 20 lbs of additional payload before sagging.

Suspension sagging occurs when payload exceeds suspension capability, causing compression of series-elastic element in line with the linear actuator in a quasi-static scenario. Under these conditions, the chassis sinks toward the compressed elements without rebound capability unless payload is removed. Adjustments of the linear actuator length proportionally compress the elastic elements without significantly altering the angle of the swing arm, thereby reducing the controllability and stiffness of the suspension.

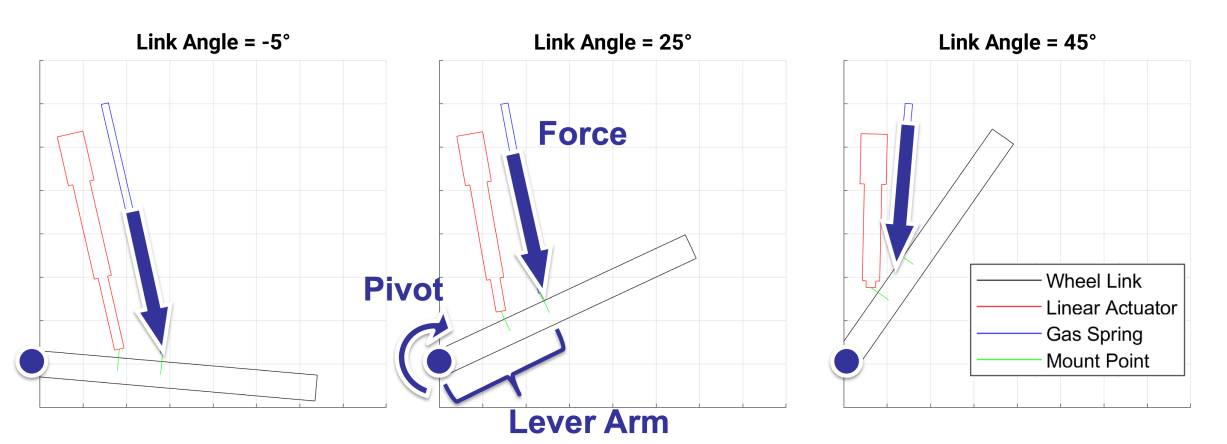

Figure 2.5: Example scenarios moving from negative to positive swingarm angle showing variability in sine losses between the gas strut and linear actuator. The swingarm is shown from left to right in this plot, moving from a 'low' position (as seen in Figure 2.3) to a 'high' position (as shown in Figure 2.4). The gas spring force and lever arm used to calculate its moment contribution are depicted in the image.

This issue primarily arises due to "sine loss," defined here as the reduction in effective torque resulting from the angle at which the actuator or gas strut applies force relative to the swingarm. Specifically, if these components apply force at angles other than perpendicular to the swingarm, part of the applied force is redirected along the swingarm itself (compression or tension) rather than producing rotational torque. In this application, torque is generated by the suspension components applying force at their respective mounting points along the swingarm. The linear distance from the pivot to the mounting point acts as the lever arm, converting applied

linear forces into moments about the swingarm pivot.

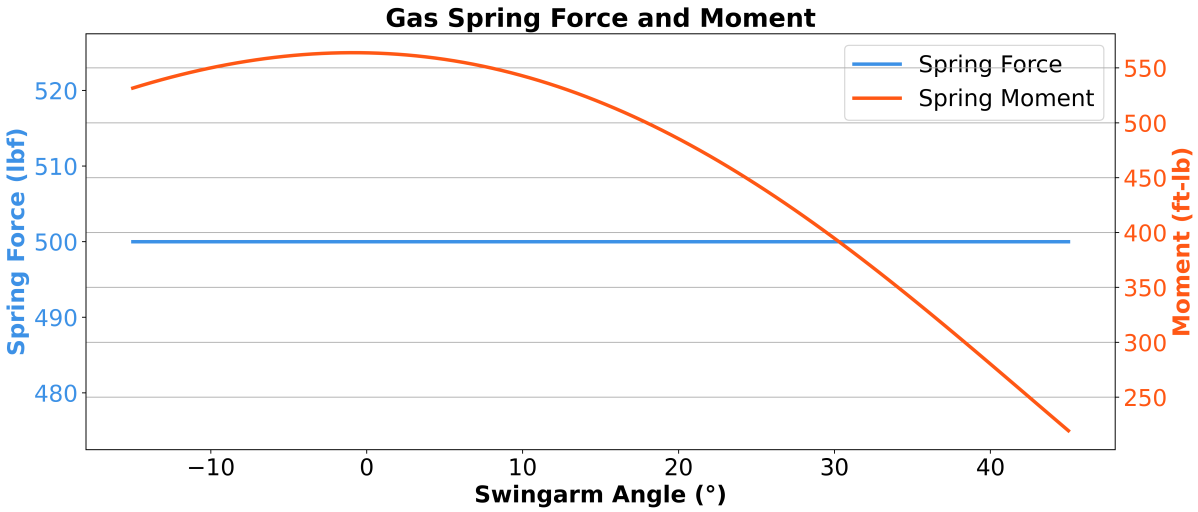

Figure 2.6: Sine loss effect on the moment the gas strut produces about the swingarm's pivot.

Figure 2.5 illustrates the position of the linear actuator and the gas strut at three angle angles of the swingarm, showing the force profile transitioning through the perpendicular state of maximum moment. Consequently, the torque contributions of these components decrease significantly at high angles, limiting suspension performance.

Figure 2.6 depicts the moment quantity that the gas strut generates as a function of swingarm angle. It should be noted the gas strut's force is independent of the swingarm angle and acts with a constant value. At the upper 45° limit the moment has decreased to less than 50% of the peak value due to the sine loss. This lack of moment to counteract the vehicle's weight is what led to the rover's lack of static stability.

2.2.2 Motivation

The key issues and limitations identified in the initial suspension configuration are summarized below.

- **Limited payload capacity at high swingarm angles:** Reduced effective torque due to sine loss leads to insufficient payload support and sagging.
- **Loss of suspension rebound:** Excessive compression of the series elastic element without adequate torque recovery capability.
- **Reduced controllability and stiffness:** Lower torque generation significantly compromises suspension performance, failing articulation requirements.

Addressing these limitations required a redesign focused on optimizing the suspension system to generate a more stable and performative system, evaluating the significant nonlinearities within the system and the sine loss effects. This combination of effects results in unstable compression of the elastic element as the reactive moment from the gas struts continues to decline and places a greater compressive force on the SEE. This formed the primary motivation and starting point for subsequent modeling and suspension design iterations detailed in this manuscript.

2.3 Method

A statics-based approach was employed to quantify and relate the moment contributions from the suspension components, enabling optimization of an upgraded system that ensures stability over all swingarm angles and a broad range of payloads. A stable configuration in this application is defined as a suspension system that does not sag, i.e. does not compress the series-elastic element in quasi-static scenarios.

By modeling the suspension as a sum of moments in static steady-state scenarios, the collective contributions of each subsystem are examined to evaluate overall system stiffness and

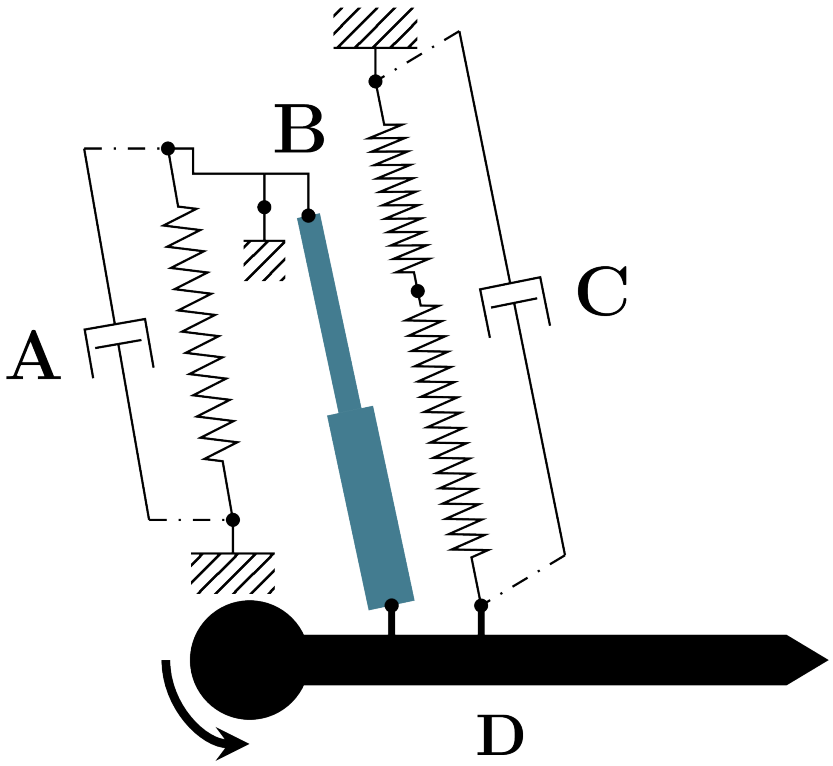

Figure 2.7: Spring-damper diagram of final BioBot suspension configuration. Labeled components: A) Series-elastic element, B) Linear actuator, C) Dual-rate spring system, D) Swingarm. Swingarm is at 0°, level with the chassis. Positive direction indicated by arrow around swingarm pivot.

rebound capability. The modeling process began by defining the three primary suspension subsystems:

- **Series Elastic Actuator** - comprised of **A** and **B** in Figure 2.7
- **Parallel Spring** - component **C**'s configuration in Figure 2.7
- **Wheel Forces** - applied at the swingarm endpoint

The moment of each subsystem is calculated about the main pivot axis of the suspension, the rotational pin joint at the swingarm base as indicated in Figure 2.7.

Figure 2.7 shows a spring-damper model diagram of the VERTEX suspension system in its final configuration. Initially, as mentioned before, the suspension employed two 250 lb gas struts instead of the dual-rate spring damper (component **C**) as shown in Figure 2.4. The system modeling, analysis, and optimization presented in this publication identified this replacement as the best configuration to resolve the issues presented in section 2.2.2. The specific details behind the model, configuration considerations, and optimization criteria are discussed in the following sections.

2.3.1 Series Elastic Actuator

The Series Elastic Actuator (SEA) consists of a Progressive Automation PA-17 8-inch linear actuator, which can provide up to 2000 lbf, and a spring-damper that compresses above 550 lbf. Since the series-elastic element is not rated for tension loads, two retention systems were implemented to minimize tension in the suspension. Figure 2.8 illustrates these: a yellow circumferential retention strap serves as the primary restraint, and a secondary mechanism of rubberized hard stops plus plate steel housing serves as a backup.

These elements are joined by a fulcrum with unequal moment arms on each side, allowing the actuator force to be partially reduced before reaching the series-elastic element. Some sine loss occurs at each interface with the fulcrum axes, enabling a compact layout. In the as-built mechanism, the series-elastic spring dampers extend between the front and rear halves of the vehicle. To reduce the system's footprint, they are offset slightly outside the plane of main suspension travel, as can be seen in Figure 2.8 with the series-elastic elements forming an 'X'.

The moment contribution of the SEA is modeled at its *maximum* value for any given angle

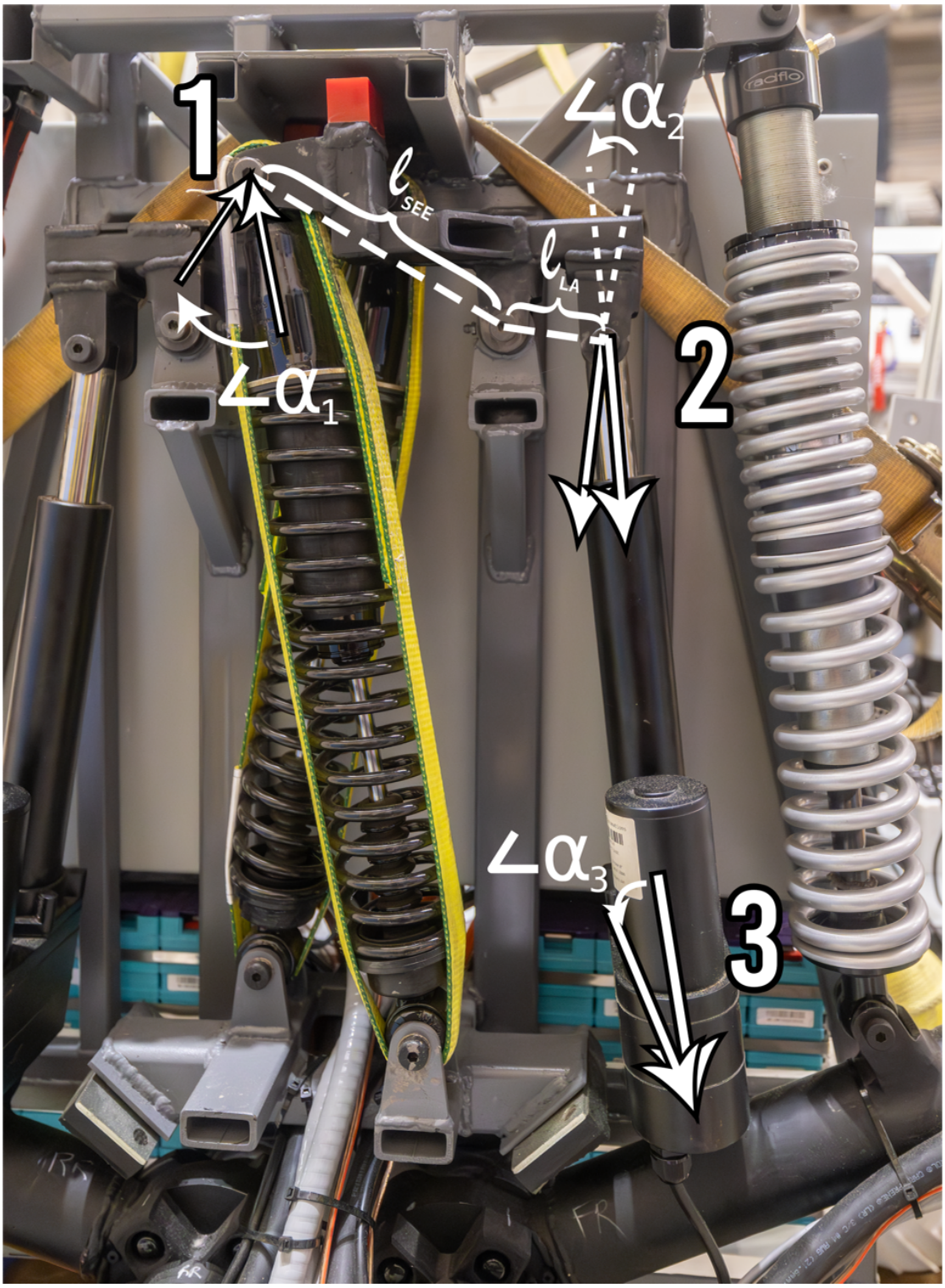

Figure 2.8: Series elastic actuator side profile, with force path from elastic element to swingarm illustrated including sine loss angles and fulcrum lever arms at an example swingarm angle. Retention mechanisms to resist tension loading additionally present.

of the swingarm. This key assumption creates an effective method for predicting if a suspension configuration will remain stable (i.e. the series elastic element remains uncompressed) and controllable in any given quasi-static scenario. The maximum contribution from the SEA subsystem can be defined as follows:

$$M_{SEA} = \frac{F_{SEE}\cos(\alpha_1) * l_{SEE}}{l_{LA}\cos(\alpha_2)}\cos(\alpha_3) * l_{B_L} \tag{2.1}$$

where F_{SEE} depends on the specific spring-damper selected for the elastic element within SEA. l_{B_L} is defined as the length down the swingarm the linear actuator is mounted as shown in Figure 2.21.

The quantity F_{SEE} depends on the characteristics of the selected elastic element. For this component single-rate (SR) spring dampers are used as a wide variety of commercial components are available to select from and can be made to fit within the suspension system. The force of SR dampers is relatively simple to calculate, accounting for a set preload distance the force model is as shown in equation 2.2. Preload controls the initial deflection of the springs before the damper experiences deflection, increasing the amount of force required to be applied before it begins to compress.

$$F_{SEE} = k_1(d_{preload} + d_{deflection}) \tag{2.2}$$

Here $d_{preload}$ is the amount of preload applied and $d_{deflection}$ is any compression of the damper from external forces. $d_{deflection}$ is 0 for stable quasi-static scenarios.

Figure 2.9 depicts the maximum SEA moment across all swingarm angles for the elastic element shown in Figure 2.8 with $F_{SEE} = 550$ lbf under the full contribution assumption.

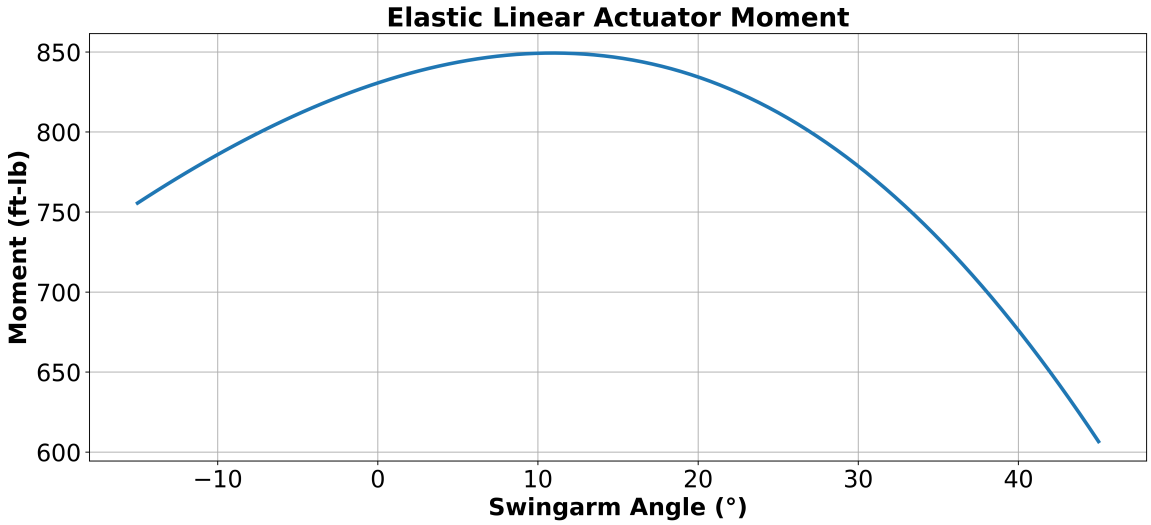

Figure 2.9: Maximum series-elastic actuator moment contribution across all swingarm angles

2.3.1.1 Spring Rate and Preload Impact on Moment

To illustrate how the single-rate spring parameters affect the full-moment contribution of the series elastic actuator system, Figures 2.10 depict the sensitivity of the torque generated over the swingarm range across a variety of spring rates and preload values. It should be noted in Figure 2.10 that all curves presented have a very similar shape to that of the moment presented in Figure 2.9 but due to the difference in magnitude the lower rate and preload curves appear to have a more linear shape.

2.3.2 Parallel Spring (PS)

The parallel spring system, whether originally implemented with gas struts or ultimately replaced by another spring system, reduces the load borne by the SEA. Its moment is defined as:

$$M_{PS} = F_{PS} * cos(\alpha_{PS}) * l_{PS} \tag{2.3}$$

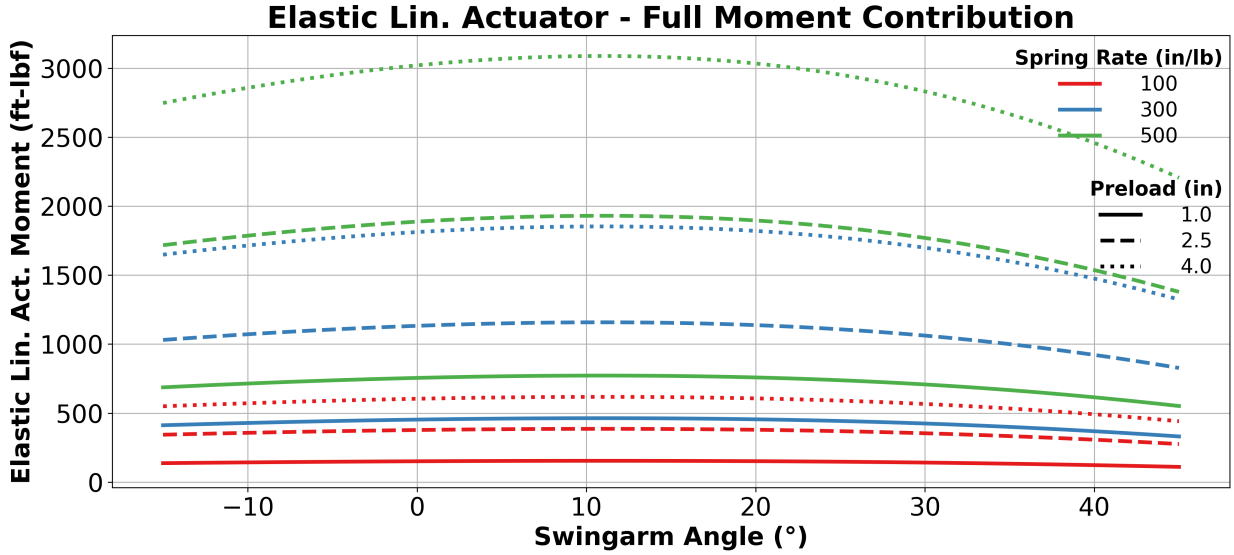

Figure 2.10: Maximum moment contribution as a function of preload and spring rate in the series-elastic element.

where α_{PS} is the angle between the force direction of the spring and the lever arm of the swingarm, analogous to α_3 in Figure 2.8. In the first suspension design, the gas struts contributed a constant F_{PS} of 500 lbf (two 250 lb struts), producing the moment curve as shown in Figure 2.6.

Due to the extended stroke length required for a component placed in a location similar to gas springs, only one category of consumer-available replacement component was found to be viable: a dual-rate spring damper. The order of magnitude for the required deflection length is approximately 14 inches or greater, depending on the final component placement. Stroke lengths of this magnitude are only found in commercial dampers that include more than one spring, and a wide variety of dampers were found specifically in the two-spring configuration referred to here as ”dual-rate” (DR) dampers.

Dual-rate shock absorbers use two *different* spring rates, commonly referred to as “top” and “bottom” rates, and feature a customizable crossover point to transition between the combined

spring rate and the lower rate. This transition point occurs when the carrier between the two springs contacts a set of adjustable arresting rings on the damper body, not allowing the top spring to deflect any further.

2.3.2.1 Dual-Rate Spring Mechanics

The force of the dual rate springs can be modeled as a piecewise function as shown in Equation 2.4, depending on the crossover settings and the deflection of the damper at the current swingarm state. The damper deflection, $d_{deflection}$, can be derived from the kinematic distance between the damper's chassis and swingarm mounting points. The variable labels for the preload, deflection, and crossover distances are shortened to the first letter for brevity (d_p - preload distance, d_d - damper displacement, d_c - crossover distance, k_c - combined spring rate, k_2 - lower spring rate).

$$F_{DR} = \begin{cases} k_c(d_p + d_d) & \text{if } d_\mathrm{d} < d_\mathrm{c}, \\ k_c(d_p + d_c) + k_2(d_d - d_c) & \text{if } d_\mathrm{d} \geq d_\mathrm{c}. \end{cases} \tag{2.4}$$

The combined spring rate is defined from the conventional series spring equation $k_c = 1/(\frac{1}{k_1}\frac{1}{k_2})$. The crossover deflection value needs careful consideration of the arresting mechanism and shifts by:

$$\Delta d_{crossover} = \frac{d_{preload} * k_c}{k_2} \tag{2.5}$$

Due to the preload compression of both springs, the floating spring carrier is repositioned downwards away from the crossover rings. This distance must be added to any crossover setting

initially set to create d_c. These equations are ultimately converted into functions of the swingarm angle θ using the DH parameters. Figure 2.11 highlights the behavior of the dual-rate shock model, showing deflection as a function of the swingarm angle for each spring and the system total.

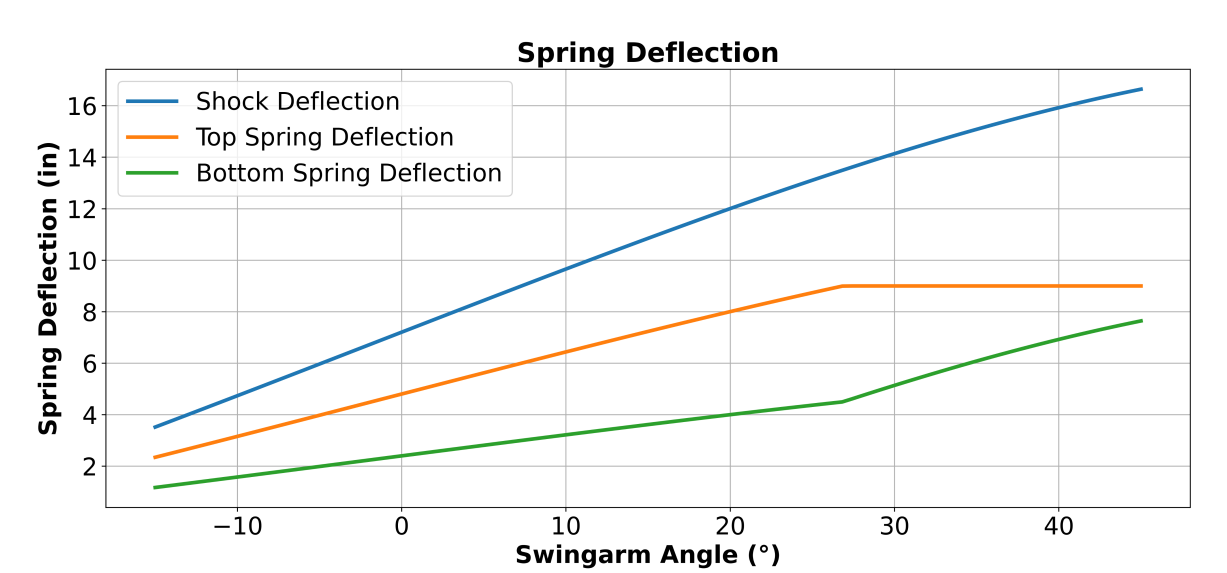

Figure 2.11: Deflection of the integrated dual-rate spring damper with finalized settings.

The force and moment contributions of the dual-rate damper model are shown in Figure 2.12. Note that while the spring force is increasing, the generated moment is decreasing at high swingarm angles despite the aggressive force slope transition due to the sine loss, highlighting the nonlinearity challenge.

2.3.2.2 Rates, Preload, and Crossover Moment Impact

To fully characterize the performance envelope of the dual-rate spring damper, one can examine how variations in preload, crossover distance, and individual spring rates influence the overall moment contribution. During the optimization process (see Section 2.3.5), these parameters are systematically adjusted to identify configurations that improve stability and load carrying

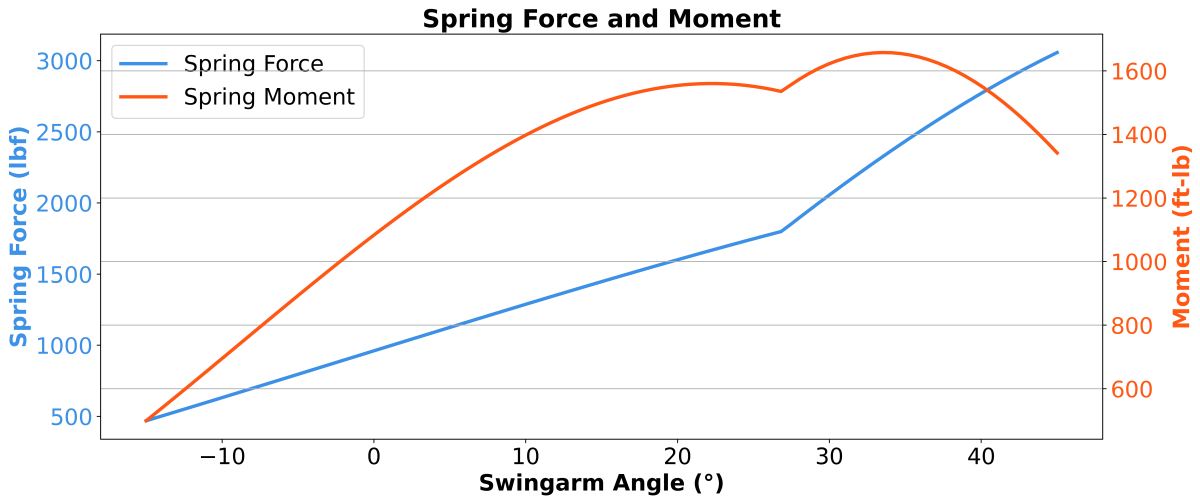

Figure 2.12: Spring force and moment sum of the as-integrated dual-rate spring damper across swingarm angle

capacity.

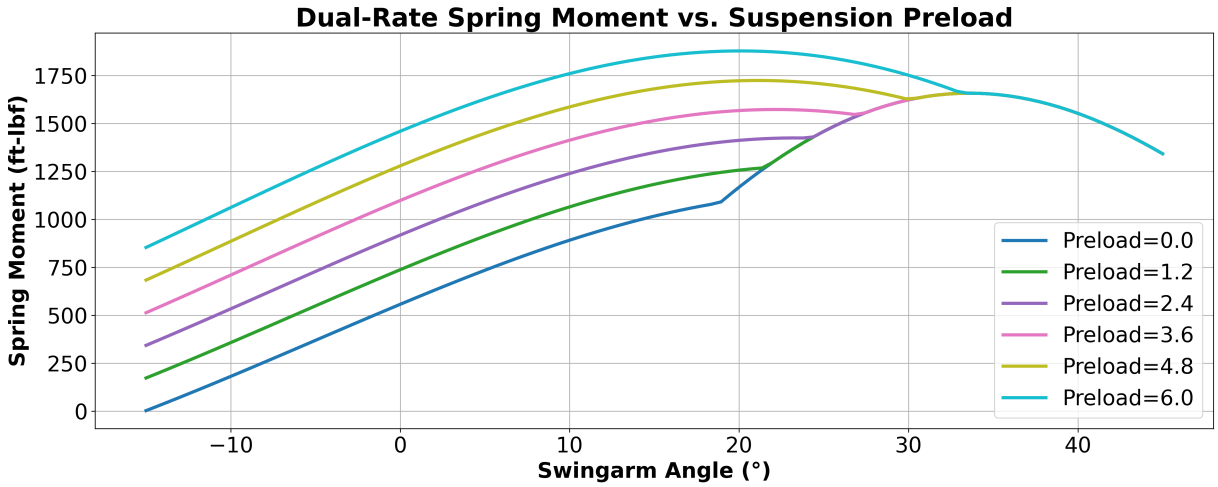

Figure 2.13: Sensitivity of the moment curve across a variety of preload (in) settings.

Figure 2.13 illustrates how changes in preload shift the moment curve. Increasing the preload increases the initial spring force, thus elevating the overall moment profile. Mechanically, higher preload translates the spring carrier downward and away from the crossover point, delaying the onset of the stiffer spring regime. Consequently, the transition point is shifted to higher swingarm angles.

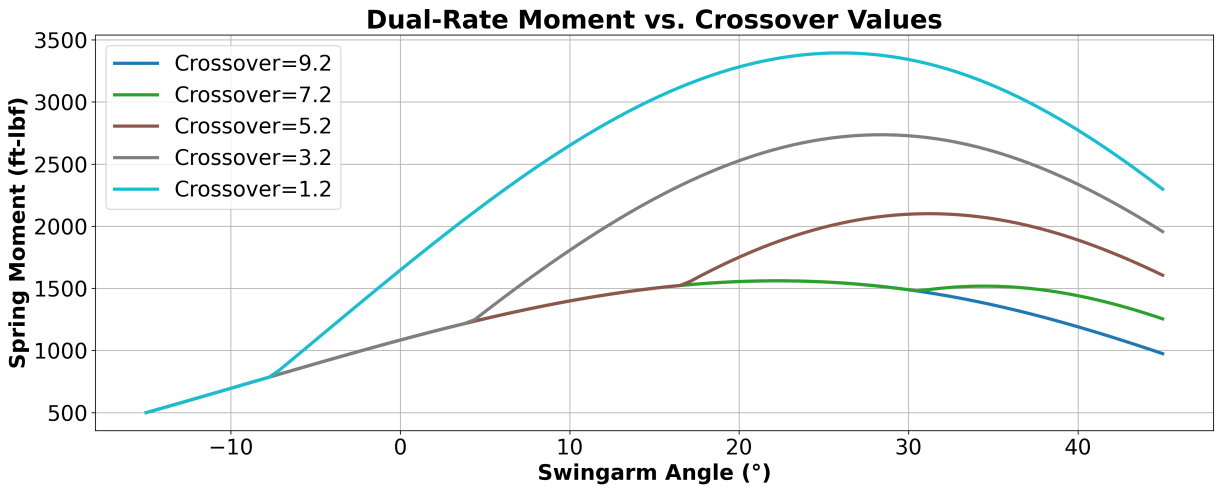

Figure 2.14: Effect of changing crossover (in) on the dual-rate spring damper moment sum

Figure 2.14 demonstrates the impact of adjusting the crossover distance while keeping the preload and spring rates constant. The crossover distance determines where the upper spring is effectively locked out, causing the damper to deflect only the lower spring. As a result, a shorter crossover distance initiates the higher rate regime sooner, whereas a larger distance extends the combined spring rate region to higher angles.

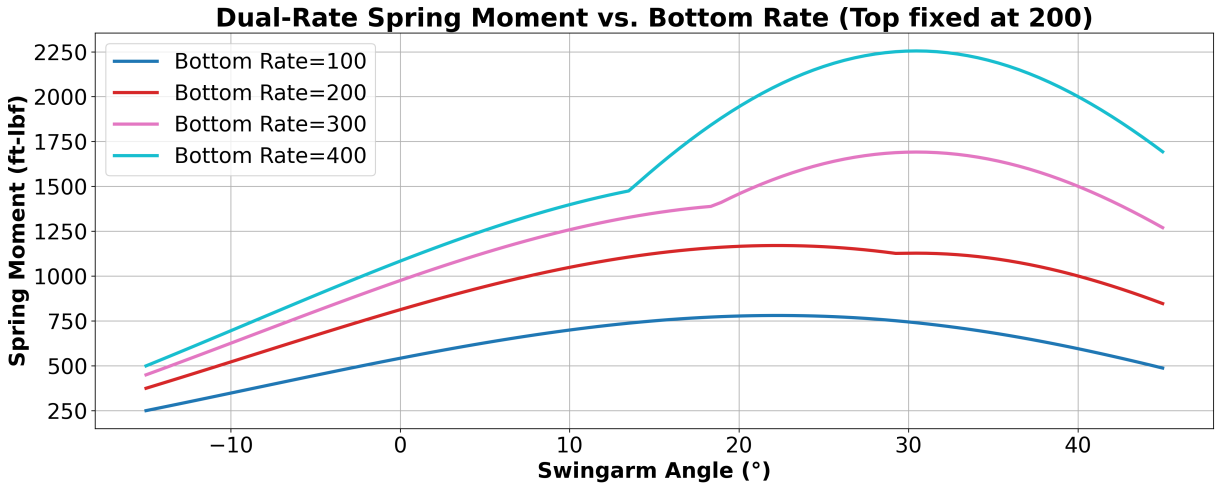

Figure 2.15: Bottom spring rate (lbf/in) adjustment effect on dual-rate moment contribution

Figure 2.15 shows how altering the bottom spring rate modifies the final higher-rate portion

of the moment curve. In particular, changing the bottom rate also affects $\Delta d_{crossover}$, influencing when the crossover event occurs. In many automotive and off-road applications, it is typical for the lower (bottom) spring rate to exceed the upper (top) rate to provide additional resistance against bottoming out. However, in the optimization routine of this study, no restriction is imposed that would mandate a larger lower rate.

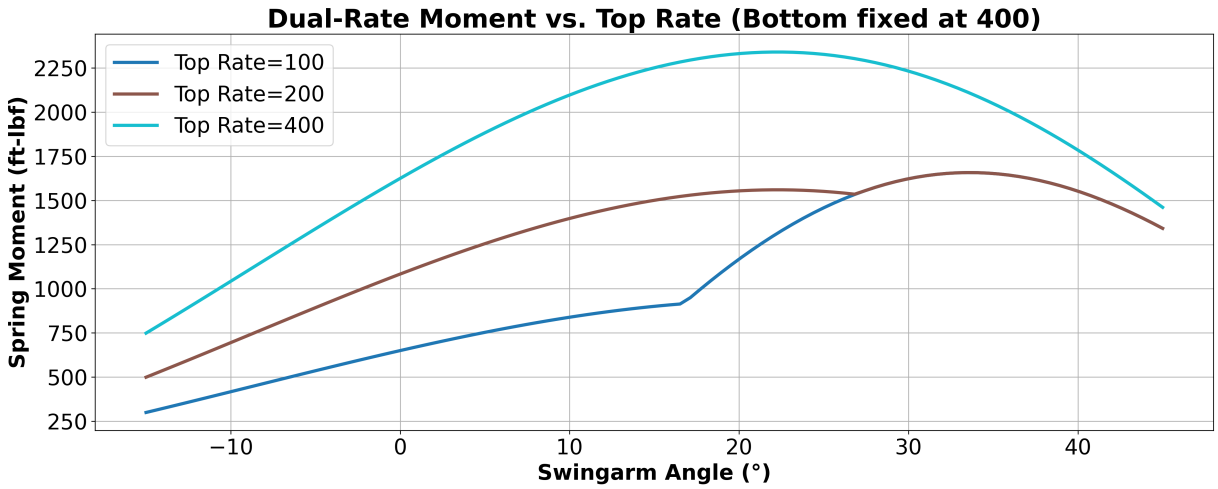

Figure 2.16: Top spring rate (lbf/in) adjustment effect on dual-rate moment contribution

Finally, Figure 2.16 illustrates the effect of varying the top spring rate. Altering this parameter modifies the combined rate in the region before crossover occurs, thus shifting the pre-crossover portion of the moment curve. Once the damper transitions beyond the crossover point, the system behavior converges to the lower spring rate and remains unaffected by changes to the top rate.

By examining these parameter sweeps, one can identify how preload, crossover distance, and the individual spring rates interact to produce a range of stiffness behaviors under quasi-static loading. This insight is helpful in tuning the dual-rate system to manage a variety of payloads or terrain conditions.

2.3.3 Wheel Force Moment

During the initial upgrade analysis phase, the rover was still being designed and constructed (see Figure 2.4), which required several assumptions about its final swingarm geometry, sprung mass, and unsprung mass. To accommodate these unknowns, a constant-moment approximation for ground reaction forces was employed, providing a conservative estimate of the torque imparted by the wheel-ground interface on the swingarm.

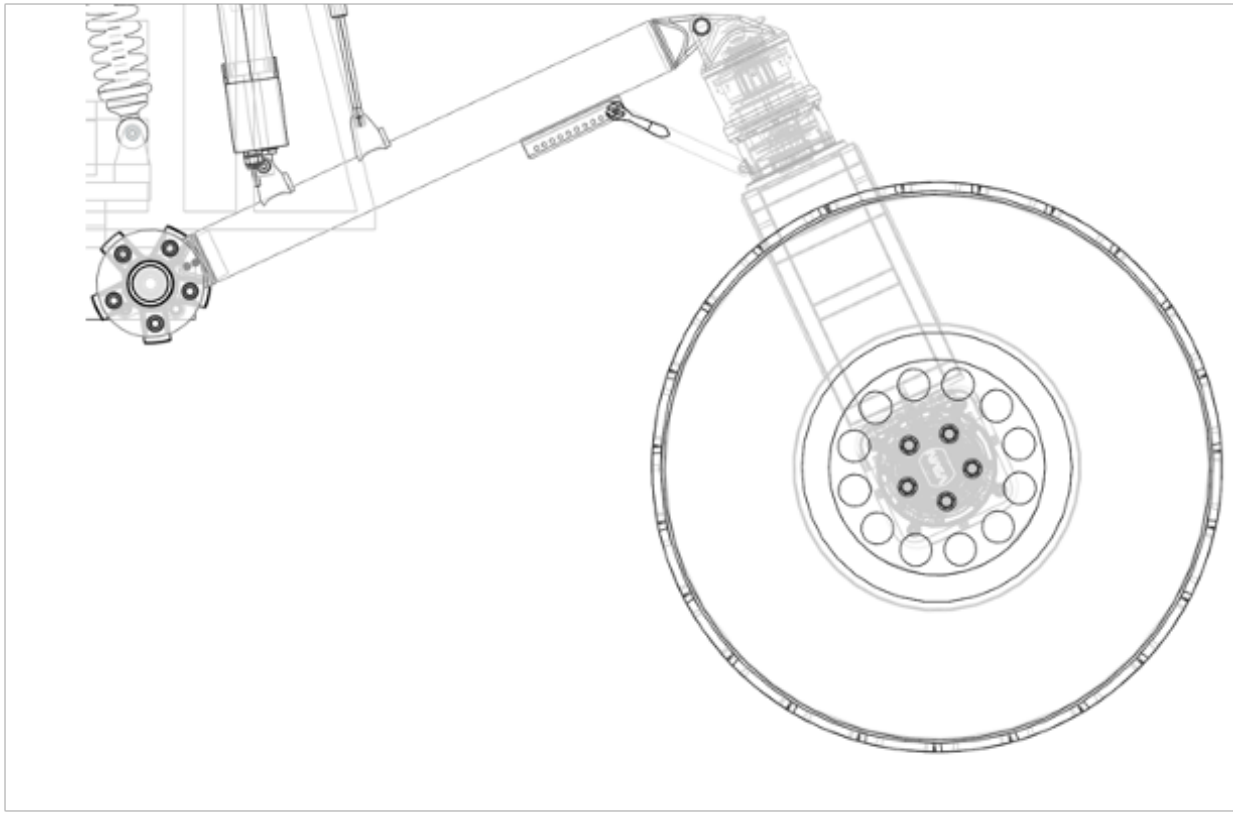

Figure 2.17: CAD drawing depicting the wheel position at maximum extension of the caster angle adjustment system

Figure 2.17 illustrates the adjustable caster system at its maximum extension, which increases the moment arm for the ground reaction forces acting against the suspension. In this extended configuration, the reaction force is assumed to act at a distance equal to the nominal

length of the swing arm plus a 30% margin. This additional 30% accounts for sloped terrains and various caster angle settings, providing a conservative buffer to ensure the suspension retains sufficient capacity under worst-case loading conditions.

Several factors justify this constant-moment approach:

1. The independently articulated suspension described herein can actively level the chassis on inclines, redistributing loads and aiding in equalizing the forces at each wheel.

2. The focus of this study is primarily on quasi-static scenarios, where transient dynamics play a lesser role.

3. The 30% margin on swingarm length effectively provides a payload reserve in less extreme caster settings. If the actual contact patch lies closer than $1.3l_{swingarm}$, the system can tolerate a correspondingly higher ground-reaction force without exceeding design limits.

Subsequent subsystem testing and field tests revealed the caster angle adjustment is often maintained at its minimum extension (Figure 2.18), where the chassis is at its lowest ride height with a caster angle (defined as the angle between the steering axis and the ground normal) of approximately 0°. Consequently, the system rarely approaches the worst-case lever arm for wheel force, further reinforcing the conservatism of the constant-moment assumption.

To ensure that the final design can accommodate the ultimate vehicle weight and diverse payload scenarios, the total (sprung + unsprung) mass was varied between 1,800 lbf and 3,600 lbf. This range captures potential payloads and the uncertain mass of late-stage subsystems (e.g., electronics, umbilical arm). Although the final rover mass is approximately 2,600 lbf ($\approx$1,180 kg-Earth), well within this range, the 30% margin at the minimum extension of the caster provides

Figure 2.18: VERTEX rover during its first field excursion, showing the caster angle adjustment system is in its minimum angle state.

the capacity for an additional 1,000 lbf payload before approaching the conservative limit of the model.

$$M_{mass} = (1.3 l_{swingarm})(m_{total} - n * m_{unsprung})/n \tag{2.6}$$

Equation 2.6 represents the wheel-force moment, where m_{total} is the gross vehicle mass, $m_{unsprung}$ is the mass of each wheel assembly, n is the the number of wheels in contact with the

ground, and $l_{swingarm}$ is the baseline lever arm from the pivot to the tip of the swingarm. The unsprung mass was estimated early on to be $\approx$ 250 lbf from the CAD as the unsprung systems were some of the first to be developed, and this aligns very closely with the final weight of 250 ± 2 lbf measured.

Although operating on fewer than four wheels ($n < 4$) is not expected for extended intervals, incorporating n into the model provides useful information on load distribution if and when wheel lift occurs.

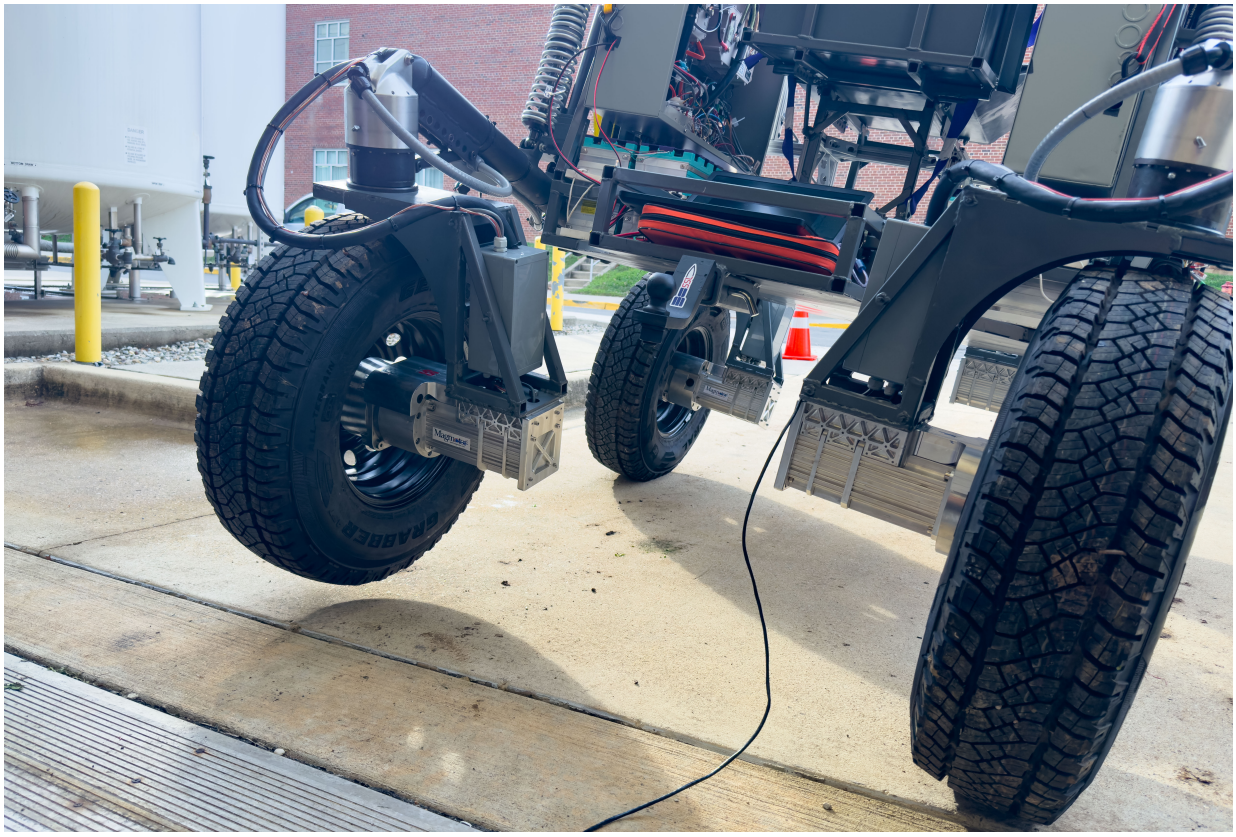

Figure 2.19: VERTEX at steady state on flat ground demonstrating a single wheel lift configuration

Figure 2.19 shows the rover without its umbilical-tending manipulator, balanced at rest on three wheels. Despite the reduced support points, the suspension remains stable, indicating that the constant-moment assumption of the model - augmented by the 30% margin - provides a

robust design basis for quasi-static loading scenarios.

2.3.4 Total System Moment

After computing the moment contribution of each subsystem, the overall suspension moment is obtained by summing these contributions, as shown in Equation 2.7:

$$M_{Total} = M_{SEA} + M_{PS} - M_{mass} \tag{2.7}$$

The plot of M_{Total} on the entire travel of the swing arm, as in Figure 2.20, provides key insights into the quasi-static behavior of the suspension and the design margins.

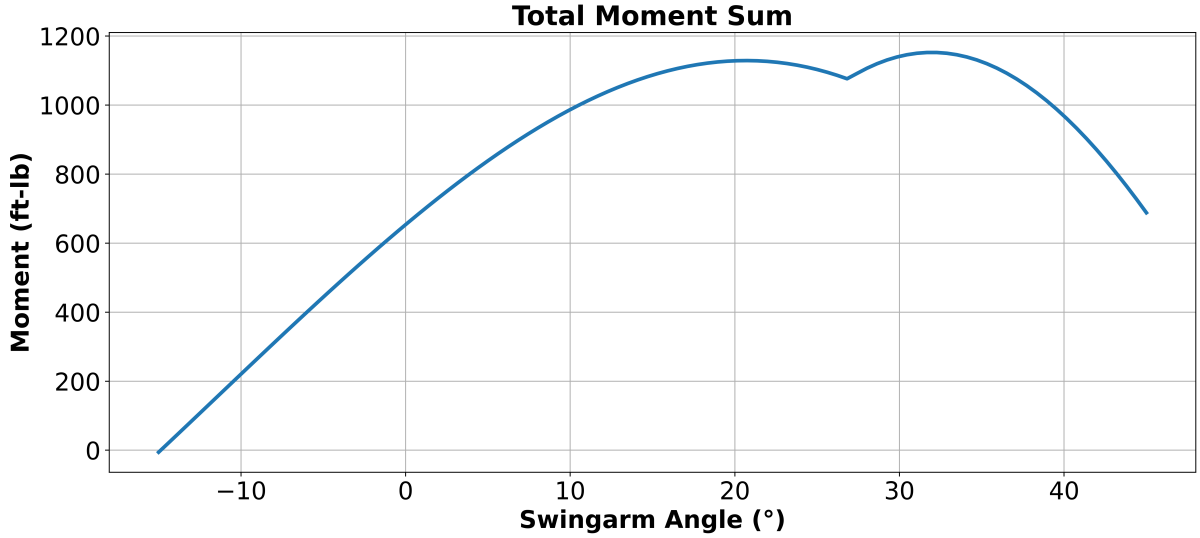

Figure 2.20: Total moment sum of the suspension model with the 200/400 lb-in rate dual-rate parallel spring damper integrated.

A primary metric of interest is *system stability*. Because the series-elastic actuator (SEA) is modeled as providing its full rated force (Section 2.3.1), any negative value in M_{Total} indicates that the SEA would compress under static loading and fail to rebound in equilibrium. Hence, verifying that $M_{Total}(\theta) \geq 0$ for all swingarm angles θ ensures the suspension does not sag and

remains stable.

Moreover, this approach also quantifies the suspension's *stiffness margin*. The amount by which M_{Total} exceeds zero at a given angle represents the additional external moment required to compress the SEA. For example, if the rover traverses an obstacle at speed, the dynamic load must surpass the quasi-static M_{Total} to deflect the spring-damper system. A larger positive margin implies a stiffer response (greater resistance to deflection), while a smaller margin allows increased compliance under transient loads.

2.3.5 System Optimization

The sum-of-moments model served as the evaluation metric within an optimization scheme aimed at re-engineering the suspension for enhanced quasi-static stability. The primary objective of the optimization was to achieve stability across a wide range of rover masses and payload scenarios while simultaneously minimizing implementation costs and development time. Due to budget constraints, only one component between the series-elastic element and parallel spring system was allowed to be modified or replaced at a time. Initially, the linear actuator was also considered for replacement; however, altering the actuator alone would not address the fundamental issue of inadequate spring response tuning and its existing specifications already satisfied the vehicle's kinematic requirements across the suspension's range of motion. Consequently, it was excluded from further consideration in this analysis. Instead, it was included as a constraint requiring the suspension configurations to keep the force in the linear actuator beneath its operating range of $\pm$ 2000 lbf. It should be noted that the model and methodology presented are fully capable of evaluating multiple simultaneous component adjustments and is capable of supporting

broader and more complex system-level optimization in future work. The available budget was the driving constraint to limit the number of adjustments.

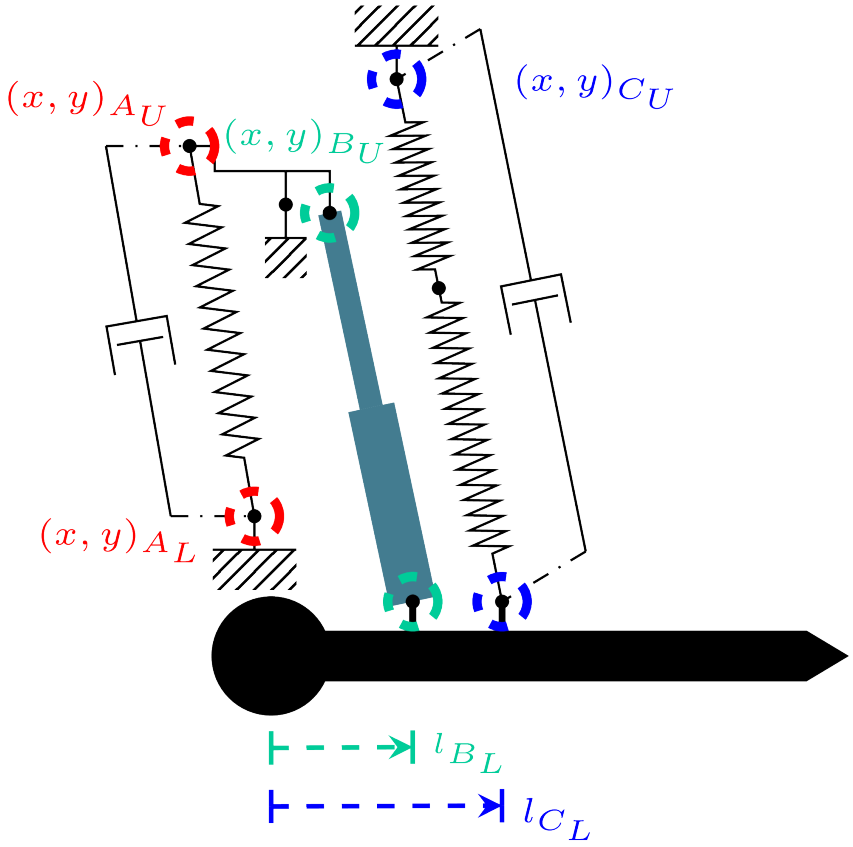

Figure 2.21: Generalized coordinates used to define component placements in the optimization scheme. The A, B, C labels correspond to the diagram in Figure 2.7, with the "U" subscript corresponding to upper mounting points, and "L" subscript to lower mounting points. (x, y) coordinates are measured from the swingarm pivot, and l coordinates are lengths measured down the swingarm from the same point.

Optimization was performed using a structured grid search method, systematically exploring combinations of component placement and suspension parameters. The initial placements of the components began from the original suspension configuration, after which the upper and lower mount positions were incrementally adjusted in a grid-wise pattern. Figure 2.21 illustrates the coordinate systems used to define these positional adjustments, with all coordinates

referenced from the swingarm pivot centerpoint. This point is also the common reference point for calculating moments within the suspension system. Components mounted directly to the swingarm utilized standardized load-rated weldable brackets at predetermined heights, simplifying the optimization task to linear offsets from the pivot axis.

Following each positional adjustment, geometric validation was performed via two tests. First, the suspension's range of motion was verified to confirm that each component's minimum and maximum extensions remained within allowable limits. Second, a mirrored setup emulating the front-to-rear symmetry of the suspension system ensured that modifications would not cause interference between opposing series elastic actuators (SEAs). The critical area of potential interference is shown in Figure 2.22, showing spatial restrictions and underscoring the necessity of maintaining compactness for operational clearance.

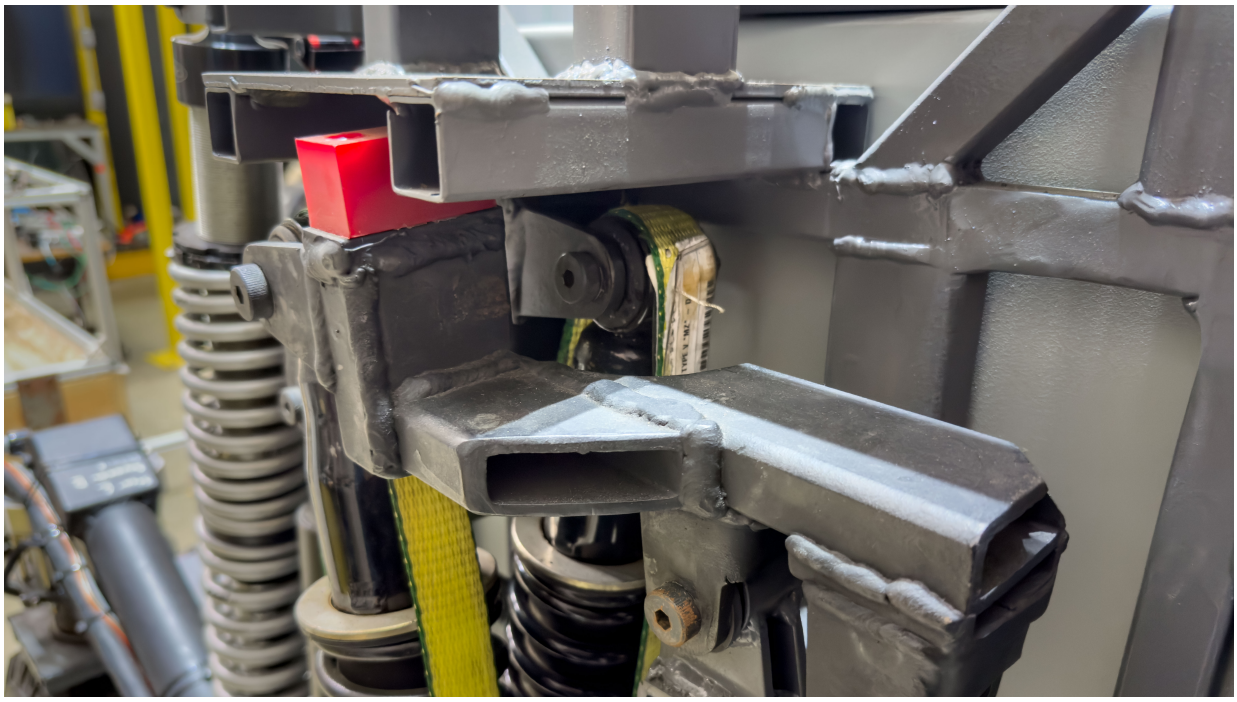

Figure 2.22: Close perspective of the arrangement of the series-elastic elements on the VERTEX suspension system. For system compactness, these elements were placed offset of the main suspension plane and require careful consideration to ensure the nominal ranges of motion are not compromised.

The pivot center of the SEA was fixed to reduce required chassis modifications, and thus adjustments were restricted to the upper mounting points of the linear actuator and series elastic element. These positional adjustments effectively modified the ratio of lever arms about the SEA pivot. Constraints were strictly enforced to prevent interference with the existing chassis, ensuring compatibility without requiring unrealistic modifications.

Upon validating geometry, spring-based components underwent additional parameter tuning. A systematic parameter sweep was conducted across a finely gridded range for spring preload (0.0–6.0 inches), crossover displacement (0.0–10.0 inches), and spring rates (100–500 lb/in, in increments of 50 lb/in). This detailed exploration aimed to maximize the suspension's stability, defined by ensuring a positive net moment across all swingarm positions. Additionally, the optimal solution was identified by selecting the combination that minimized the peak positive moment value, minimizing any over-stiffening effect.

The results revealed clear performance distinctions between the two replacement strategies. For the single-rate adjustable spring, stable configurations adhering to the linear actuator force constraint were achievable only within a limited rover weight range (approximately 2900 lbf and below). In contrast, the dual-rate spring configuration was able to accommodate the full range of vehicle weights. Figure 2.23 illustrates the optimized peak moment sum results, highlighting the consistently lower peak moments achieved by the dual-rate spring configurations compared to the single-rate scenario. This indicates that the dual-rate springs offer enhanced tunability and suggest a more compliant suspension can be generated across a broader range of payload conditions.

It is important to note that due to budget constraints this study limited the optimization to modifying only one suspension component at a time. However, the established optimization

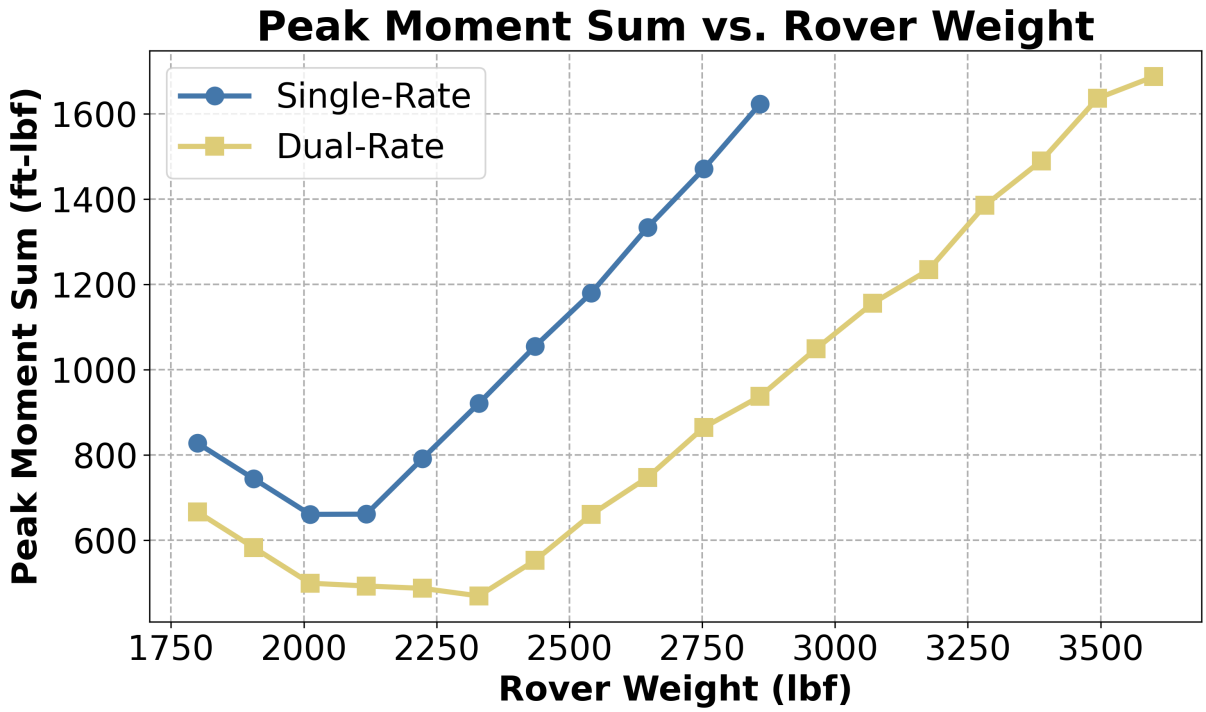

Figure 2.23: Comparison between the best single-rate spring replacement and the best dual-rate spring replacement results.

model is fully capable of simultaneously evaluating adjustments to multiple components, thereby enabling analyses of more complex and comprehensive suspension configurations. This additionally does not limit the use of this modeling approach and assumptions within it (notably the full-contribution assumption) from performing a multi-objective optimization scheme to optimize other suspension systems.

2.3.6 As-Built System Upgrades

The optimization results identified that replacing the original gas struts with dual-rate spring-damper assemblies offered superior performance and adaptability across the broadest range of payload conditions. Although no single configuration of springs, preload and crossover could fully accommodate every scenario tested, the dual-rate damper was uniquely capable of

Figure 2.24: Dual rate spring modification exhibiting lack of rebound and controllability at steady state conditions due to higher than expected sprung mass during electronics integration phase. Top rate 150 lb/in, bottom rate 200 lb/in. Increasing the dual-rate damper's preload returned the system to positive static stability.

maintaining positive net moments through the appropriate adjustment of these settings. Figure 2.24 illustrates the as-integrated dual-rate shock absorber under an early configuration of the

second suspension iteration (top rate 150 lb/in, bottom rate 200 lb/in). Figure 2.24 demonstrates the vehicle post-upgrade experiencing a lack of rebound due to tuning the preload on an empty chassis weight. The yellow circumferential strap responsible for eliminating tension forces within the element is slack in the image, indicating the element has been compressed. Once additional components such as batteries, seat, crew interfaces, the umbilical-tending arm, and a test subject were added, the nominal payload capacity was exceeded for the initial suspension settings. By increasing preload and adjusting the crossover point, the suspension regained positive control as predicted by the model.

As emphasized during the design phase, a primary objective was to maintain flexibility in hardware so that discrepancies or new payload configurations could be managed with minimal additional fabrication. In practice, the vehicle's final weight after full electronics integration ($2,600 \pm, 2lbf \approx$ 1180 kg-Earth) exceeded the dual-rate damper settings used in response to Figure 2.24. Consequently, the final dual-rate damper configuration, guided by the model in Section 2.3, used a 200 lb/in upper spring rate and a 400 lb/in lower spring rate, with approximately 1.5 in of preload and a crossover transition occurring at 27.3° of swingarm travel. This revised setup delivered reliable quasi-static stability under both empty and partially loaded conditions, as predicted by the model.

Figure 2.25 shows the extent of chassis modifications that were required to implement these spring-damper assemblies, while Figure 2.26 highlights the finished chassis structure. The magenta region in Figure 2.26 corresponds to the original gas spring mounts cut out during the upgrade process.

Overall, this dual-rate conversion combined with appropriate parameter adjustment resulted in a robust and versatile suspension architecture. Despite initial challenges stemming from unex-

Figure 2.25: Heavy chassis modifications required for upgraded suspension including removal of old structure and welding of new supports to support dual-rate spring dampers.

pected increases in sprung mass, the final system proved capable of stabilizing the vehicle under a range of loading scenarios, validating both the theoretical model and the flexible, component-

Figure 2.26: Chassis after modification to remove old mounts and create new structure

driven approach to hardware redesign. The final field-tested configuration was used for all non-sensitivity plots in Section 2.3 and serves as the basis for validation and improvement efforts detailed in Section 2.4.

2.4 Force Sensing and Validation

To quantify the improvements in controllability and validate the moment-based suspension model, a systematic analysis was conducted on the as-built VERTEX rover. Field observations by the SSL team indicated that the upgraded stiffer suspension noticeably enhanced operator confidence with test subjects successfully adjusting chassis height and angle. However, it was noted that future optimization could be performed to improve ride comfort and refine controllability. Such refinements rely on accurate characterization of the as-built system to confirm modeling assumptions and guide future development.

Figure 2.27: Compression/tension load cell sensor replacing the series-elastic element in the VERTEX suspension system

2.4.1 Load Cell Integration and Calibration

An Omega Engineering LC103B-3K compression/tension load cell was purchased and integrated to directly measure forces within the system. As shown in Figure 2.27, the load cell replaced the series-elastic element in the front-right (FR) suspension. Mounting it at any other location or in series with the existing spring would have significantly altered suspension kinematics or required extensive system modifications. Although replacing the series-elastic element with a load cell effectively rigidizes the FR corner, testing was performed under quasi-static conditions to represent the loads that the elastic element would typically experience without compressing.

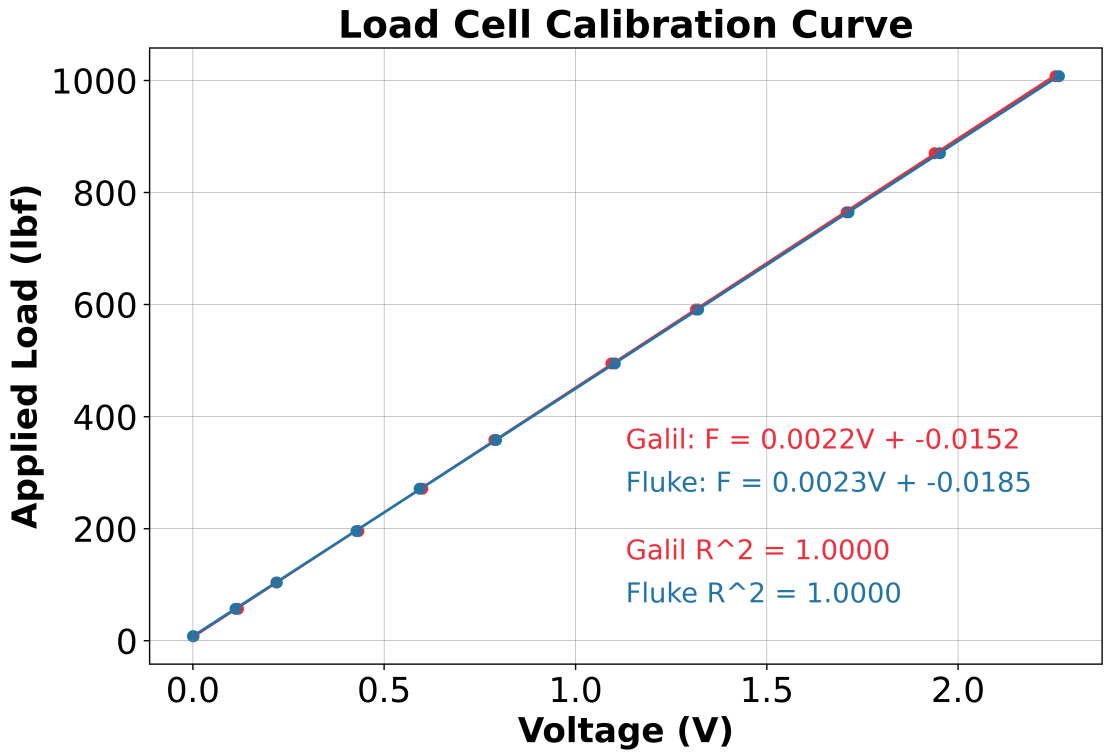

Figure 2.28: Calibration curve for transforming recorded voltages from the load cell and amplifier to forces exerted on the cell. The red Galil curve recorded voltages from the onboard Galil motion control system, and the blue Fluke curve used manually measured and recorded values from a Fluke 117 multimeter.

Figure 2.28 presents two calibration curves correlating measured voltages to applied force using a crane scale (precision ± 2 lbf) and the known weight of the VERTEX vehicle. One calibration data set used onboard Galil controller voltages, while the other employed a Fluke 117 multimeter. Both curves exhibit excellent linearity, each with $R^2 = 1.0000$. For all subsequent analyses, forces were derived from voltages recorded by the Galil system.

2.4.2 Data Collection and Analysis

A series of quasi-static tests were conducted to capture the suspension's characteristics. The onboard datalogger recorded:

- System uptime and controller states
- Suspension and steering modes
- IMU data (quaternions, roll, pitch, yaw, linear/angular accelerations)
- Load cell voltages
- Actuator metrics (commanded positions, actual positions, velocities, accelerations, efforts)

The data was sampled at a rate of 100 Hz via the onboard ROS (Robot Operating System) controllers. Future upgrades to the motor drivers will allow traction motor data to be recorded in similar fashion for dynamic trials.

The trial shown in Figure 2.29 involved cycling the chassis between maximum and minimum heights while maintaining near-zero pitch and roll. All four swingarms were commanded to cycle between their upper and lower positions at identical rates. Nearly five complete cycles

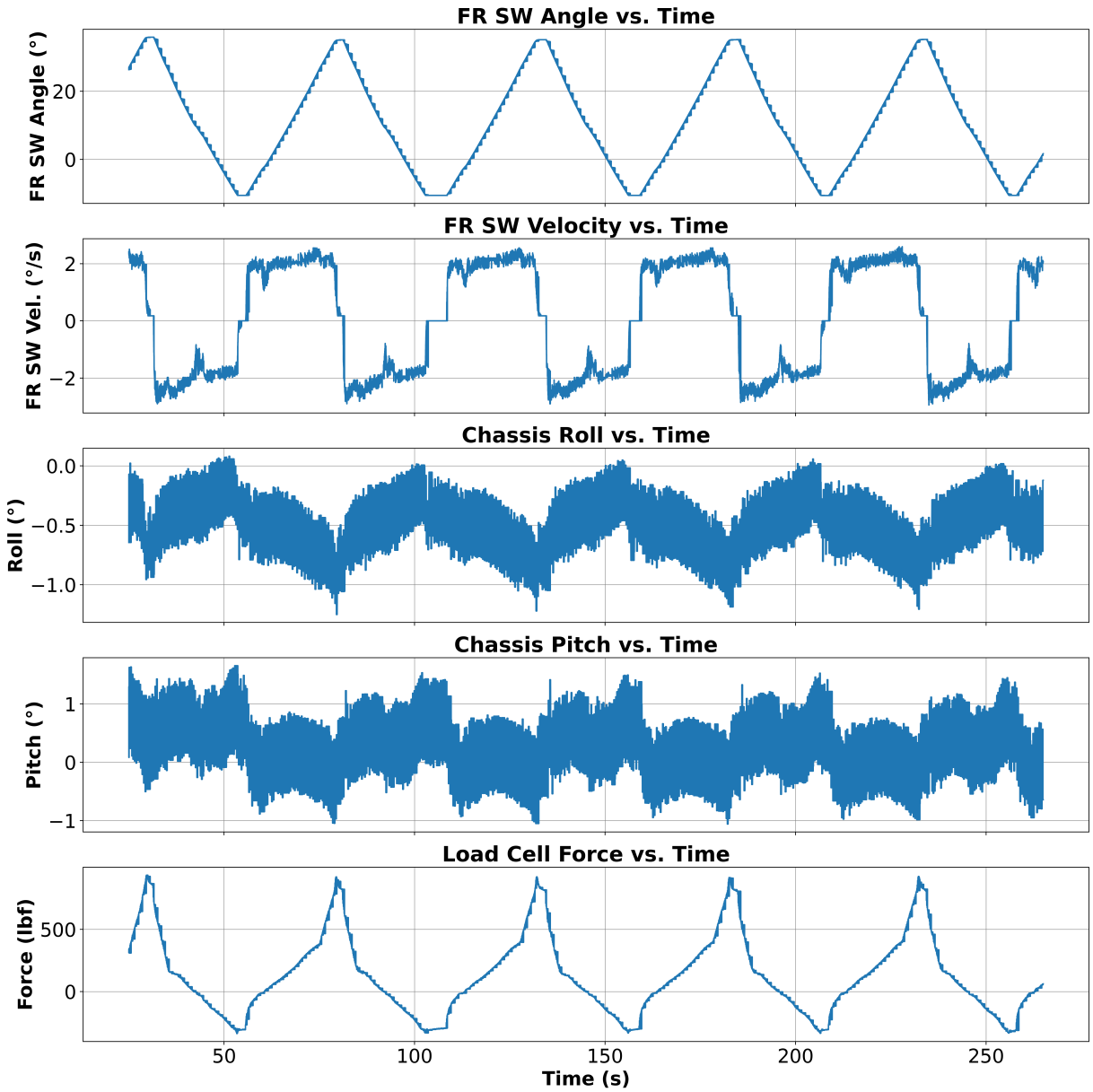

Figure 2.29: Subset of data collected on an experiment run, cycling the chassis between maximum and minimum height while maintaining as low pitch and roll values as possible. Note that startup and shutdown transients have been removed from the beginning and ending of the approximately 300 second run. In the labeling, ”FR” designates the ”Front Right” suspension corner, and ”SW” abbreviated for ”Swingarm”.

of motion were logged, and Figure 2.29 presents a subset of the complete data for the front-right suspension, chassis roll and pitch, and load cell force.

The control algorithm computed desired encoder positions for each swingarm based on

Table 2.2: Roll and pitch statistics from dataset in Figure 2.29

Quantity	Mean	Min	Max	1σ Std. Dev.
Roll	-0.48°	-1.25°	0.45°	0.32°
Pitch	0.34°	-1.06°	2.26°	0.76°
Force (lbf)	132.36	-337.81	935.78	287.90

a target translation distance and rate. Due to IMU noise, the system did not actively adjust swingarm velocities to maintain a level chassis during movement since the rover operations were already occurring within the chassis leveling control loop's bandwidth. Future upgrades to the IMU to reduce effective noise are slated for near-term upgrades, dependent on funding. However the at a total of 1.8° of roll variation, and 3.32° of pitch variation, the chassis angles seen in this dataset are not be dissimilar to real-world chassis angles seen in normal operations. In short, pitch and roll remain small, indicating that the four swingarms moved at sufficiently similar rates to keep the chassis near level despite IMU noise and minor velocity differences among corners. Table 2.2 summarizes the roll, pitch, and load cell force statistics over this interval.

To precisely show the minor variances, Figure 2.30 overlays motion data from all four swingarms, with 0° representing a level position perpendicular to the gravity vector. Table 2.3 quantifies the range of motion and maximum angular rates for each corner, revealing modest discrepancies likely due to minor manufacturing tolerances, uneven payload distribution (e.g., the umbilical-tending manipulator), and most likely, the rigidization introduced by the load cell in the FR corner.

Table 2.3: Variability between each swingarm range of motion. FR = Front Right, FL = Front Left, RR = Rear Right, and RL = Rear Left

	Min Angle	Max Angle	Max - Rate	Max + Rate
FR	-10.63°	35.90°	-2.94°/s	2.59°/s
FL	-7.11°	38.14°	-3.60°/s	2.81°/s
RR	-8.06°	35.90°	-3.16°/s	2.33°/s
RL	-6.41°	38.58°	-3.55°/s	2.72°/s

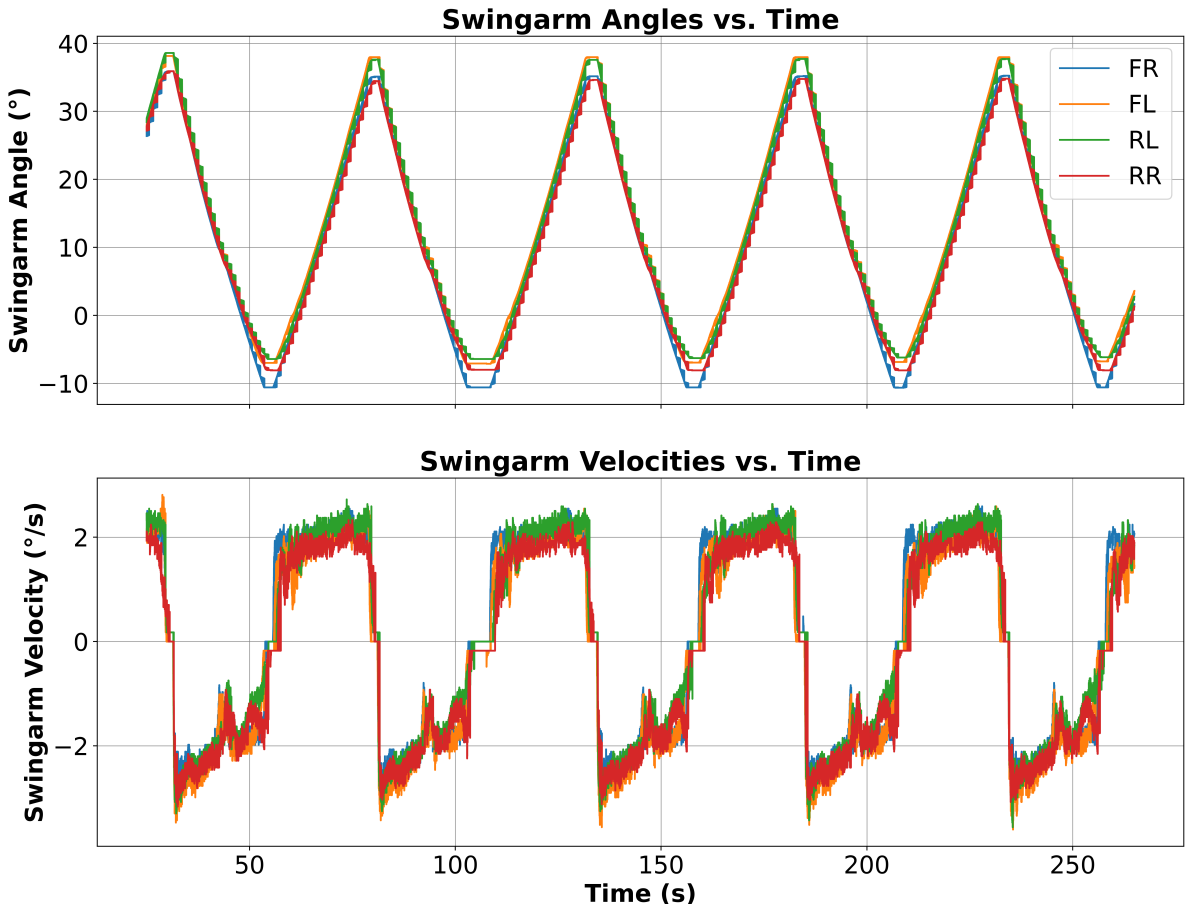

Figure 2.30: Overlaid angles and angular rates for all four swingarms plotted across time from the dataset shown in Figure 2.29. FR = Front Right, FL = Front Left, RR = Rear Right, and RL = Rear Left

Additionally, it should be noted the upper suspension travel is physically constrained by a rubberized hard stop at its upper limit, but in the presented dataset the linear actuators encounter tension forces exceeding 2,000 lbf due to the dual-rate spring crossover setting preventing further retraction. Ongoing efforts aim to optimize for full translation to the hard stop without compromising control.

2.4.3 Operational Characteristics

From the same dataset, focusing on the front-right suspension system, Figure 2.31 illustrates the relationship between the angular position and velocity of the swingarm. The following critical characteristics emerge from this graph, each with implications for rover operations.

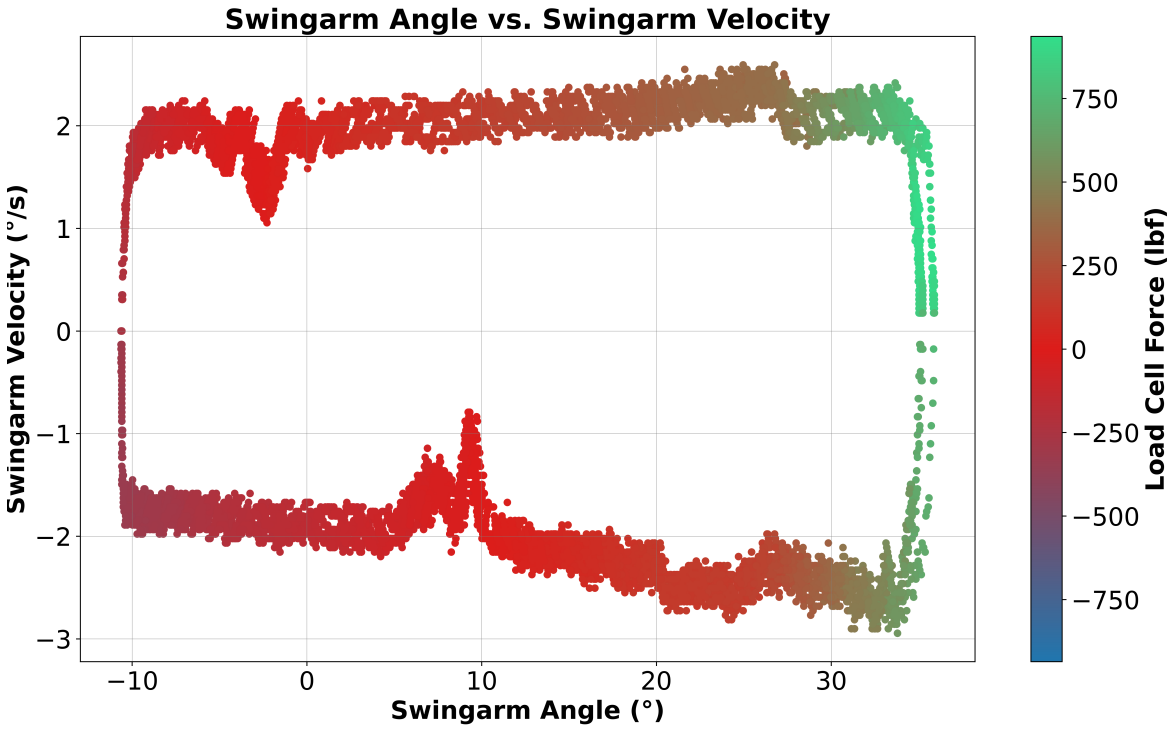

Figure 2.31: 2D plot depicting relationship between swingarm angle and swingarm velocity, colorized by force experienced by load cell. Positive force is tension, and negative force is compression.

2.4.3.1 Nonlinear Kinematics and Force Distribution

The tapering of data from left to right reflects the non-linear geometry of the suspension. The swingarm's full range of motion spans -13.8° to 45°, with prismatic elements undergoing variable deflections throughout this travel, as illustrated by Figure 2.32. The change in color underscores how the front-right corner transitions between compression and tension as it increases

in angular position, indicative of the interplay between the parallel spring-damper system and the vehicle's weight.

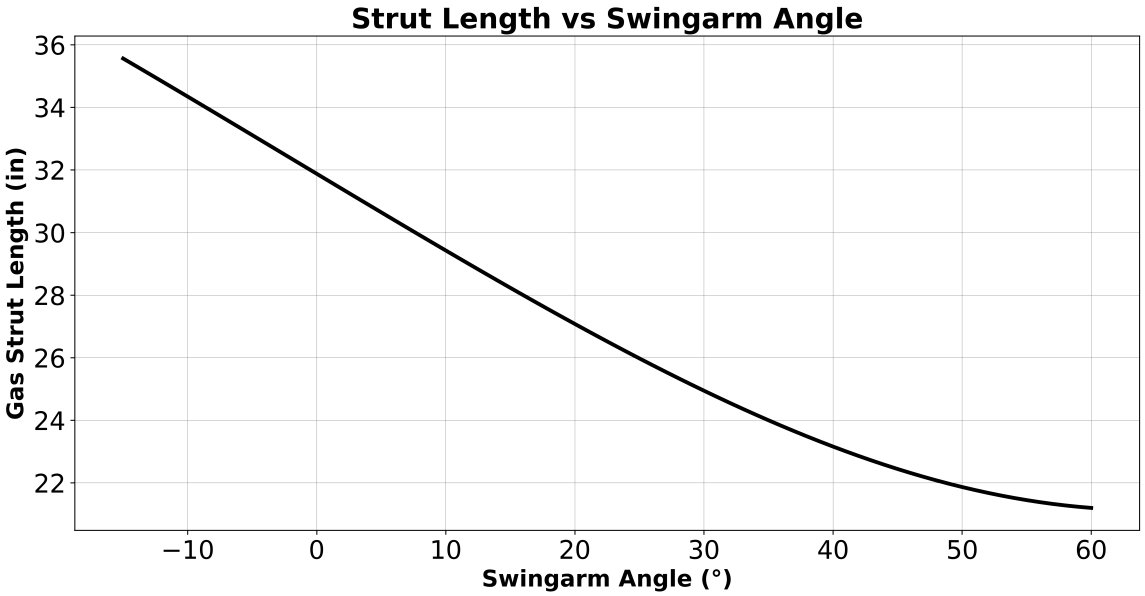

Figure 2.32: Strut length for the original gas struts plotted across swingarm angle showing varied rate in length change as swingarm travels upwards

2.4.3.2 Dynamic Disturbances and Hysteresis

Two significant disturbances are evident in the plot. The first occurs at a swingarm angle of approximately -2.29° in the positive velocity (upper) half, and the second at 9.23° in the negative velocity (lower) half. These points, as evidenced by the colorization, represent transitions between tension and compression within the series elastic actuator system.

The series-elastic system employs welded steel pivots and soft rubber bushings to interface the actuator, spring damper, and vehicle structure. During the transition from tension to compression, dynamic loading and unloading of these bushings and any connection backlash create a region of reduced controllability. The delta in the swingarm angle between these two transition

points between the positive and negative velocity directions is evidence of a significant system hysteresis, likely due to friction in the bushings and the parallel spring damper system. Quantifying this hysteresis may become an important characteristic for future predictive system response efforts.

One optimization approach could focus on minimizing load on the actuator, theoretically maximizing actuation speed and allowing the spring-damper to better absorb driving disturbances. If the series elastic element is experiencing compressive force at a standstill some of the preload intended for rebounding during deflections is naturally taken up. Conversely, if the element is under excessive tension, the vehicle's response to dynamic forces becomes overly harsh as disturbances must first overcome the SEE's tension before being compressing spring damper. Figure 2.31 shows distinct inconsistencies in this transition area, presenting control challenges in the transition between tension and compression. The differential in the angular position of this transition between the positive and negative directions is additionally indicative of a significant hysteresis.

2.4.3.3 Spring Crossover Point

At a swingarm angle of 27.29° (ref. Figure 2.31) the suspension system's dual-rate spring damper transitions from the two-spring series configuration to the single spring acting condition. Below this angle the effective spring rate is 133.33 lb/in, derived from the combination of 200 lb/in and 400 lb/in series springs. Beyond this angle, the effective rate shifts to 400 lb/in. This transition point is consistent between the positive and negative velocity direction as it is a kinematically-constrained parameter whereas the tension/compression line is determined via

variable moment contributions.

The crossover point, which can be customized, was set during field testing at NASA Goddard to balance system stiffness and controllability. This setting allowed for improved operation under the varying payload and terrain conditions encountered during testing.

2.4.4 Validation of Kinematics and Regime Transitions

The model accurately predicted the crossover points between the dual-rate and single-rate springs, as seen in both the experimental data and Figure 2.20. This alignment demonstrates that the kinematic parameters of the suspension were not only mathematically modeled correctly but also fabricated with close precision to the as-designed chassis, reinforcing confidence in the assumptions and methods used (Sections 2.3 and 2.3.5).

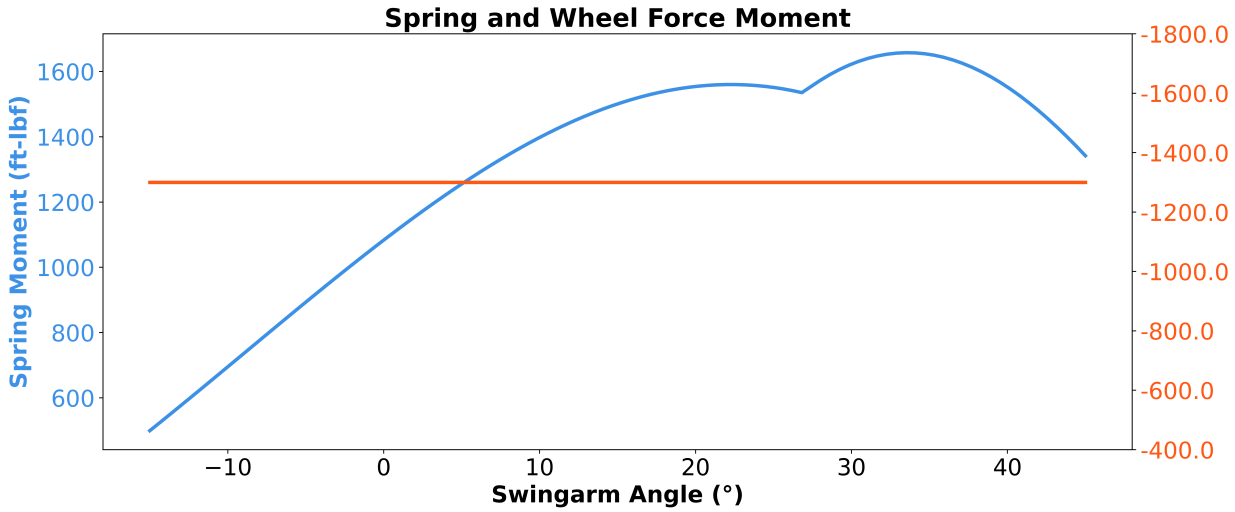

Figure 2.33: Wheel moment and parallel spring-damper moment plotted together. Wheel moment is inverted to more clearly see the point of transition where the series-elastic actuator does not provide counteractive force to the wheel-moment and instead is placed under tension.

The transition from compression to tension in the negative velocity region of Figure 2.31 serves as another key validation point. As highlighted in Figure 2.33, this transition occurs where

the parallel spring-damper moment surpasses the negative moment from vehicle weight, placing the series-elastic actuator in tension. This crossover is critical, as it signifies the point at which the suspension's stiffness begins to dominate system response.

The observed static transition of the built system aligns well with the lower transient region in Figure 2.31. In fact, this was tested by removing the series-elastic elements with the suspension at it;s steady-state no SEE load position as shown in Figure 2.34. The swingarm angle at which this occurs is $\approx 9.23°$ and aligns closely with value predicted as shown in Figure 2.33. This agreement reinforces the model's accuracy in predicting dynamic transitions and operational stiffness.

2.5 Results and Discussion

Although direct moment contributions of each component cannot be directly measured, the characteristics identified in section 2.4.3 show strong alignment between experimental data and model predictions in kinematics, the zero-force/regime crossover point, and in expected system nonlinearities. However, the presence of the force hysteresis within the system was unexpected and it may become beneficial in the future to identify the source or resolution of such a significant difference in force as a function of the swingarm velocity direction.

2.5.1 System Failure Mitigation

Although major structural or component failures are uncommon, the system has been designed to remain operational under certain failure modes. Specifically, if the series-elastic element were to fail (e.g., by exceeding its damper rating or if a retention strap should break), the

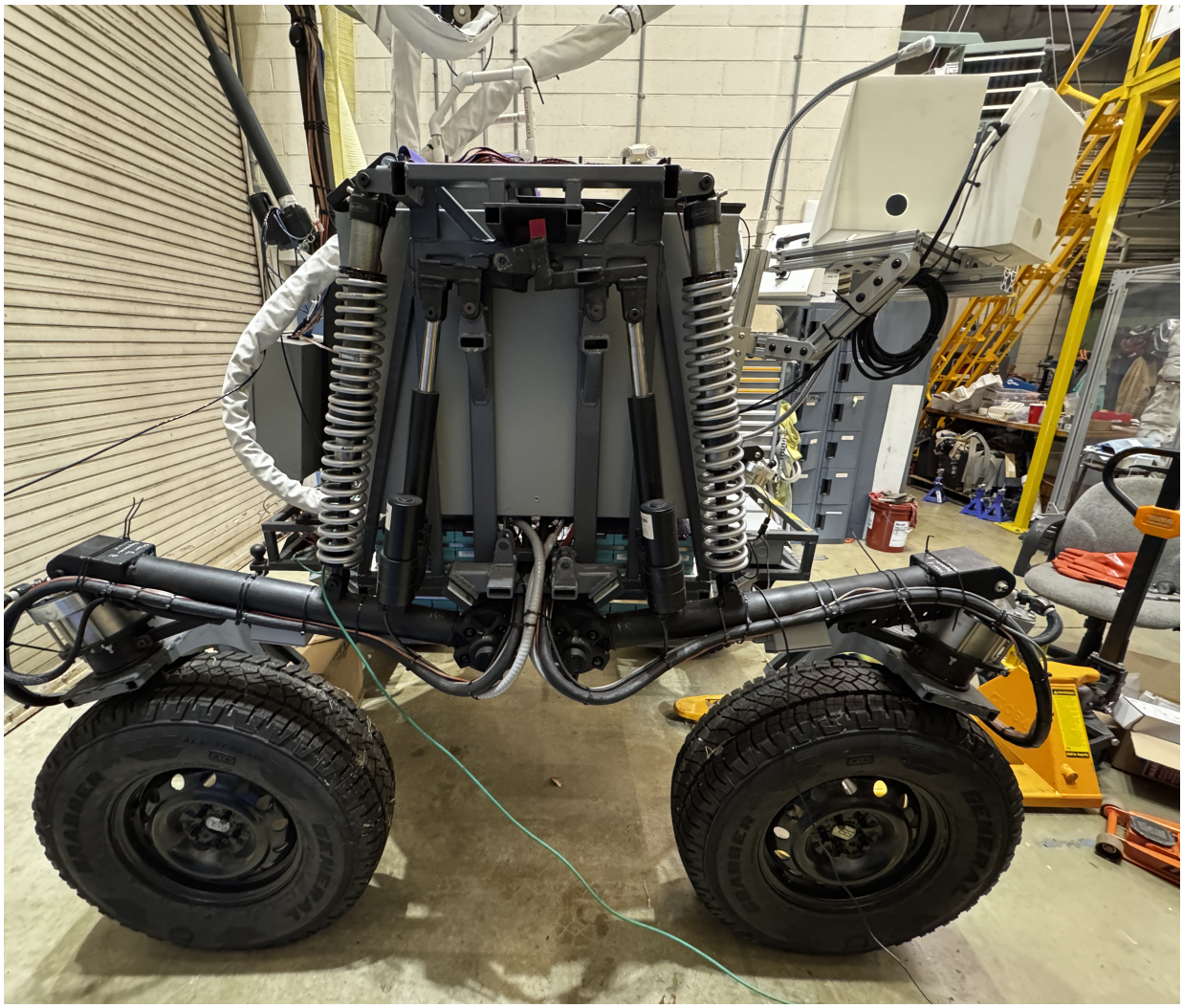

Figure 2.34: VERTEX suspension system at steady state with both series elastic elements removed from the vehicle's right side. This indicates the point of no-load in the series elastic element, and the point of transition between tension/compression.

suspension can still maintain control if the linear actuator is held in tension via the vehicle's structure. This inherently robust design allows mission-critical functions to continue even under non-ideal conditions.

An in-lab failure event (Figures 2.35 and 2.36) illustrates similar robustness. During a crane-assisted lift, the wheel moment transitioned, as one might expect, from negative to positive, causing the linear actuator to bear not only the dual-rate spring force but also the unsprung wheel

Figure 2.35: VERTEX during a crane lift to remove vehicle from trailer.

load. The actuator's structural housing subsequently yielded. Thanks to the system's modular design, the damaged actuator was easily replaced with minimal downtime (Figure 2.36). Even with the actuator removed, the swingarm angle was maintained at it's stable point, settling at 9.23° albeit with reduced stiffness.

Moving forward, lifting procedures now incorporate rated straps to transfer the spring and wheel loads onto the chassis or else occur at lower swingarm angles, thus minimizing the risk of overloading the actuator. More critically, the design ensures that an isolated failure of an actuator or series-elastic element is not mission-ending. If necessary, the suspension can revert to a simpler single-strut configuration for that corner, sustaining operational capability until full

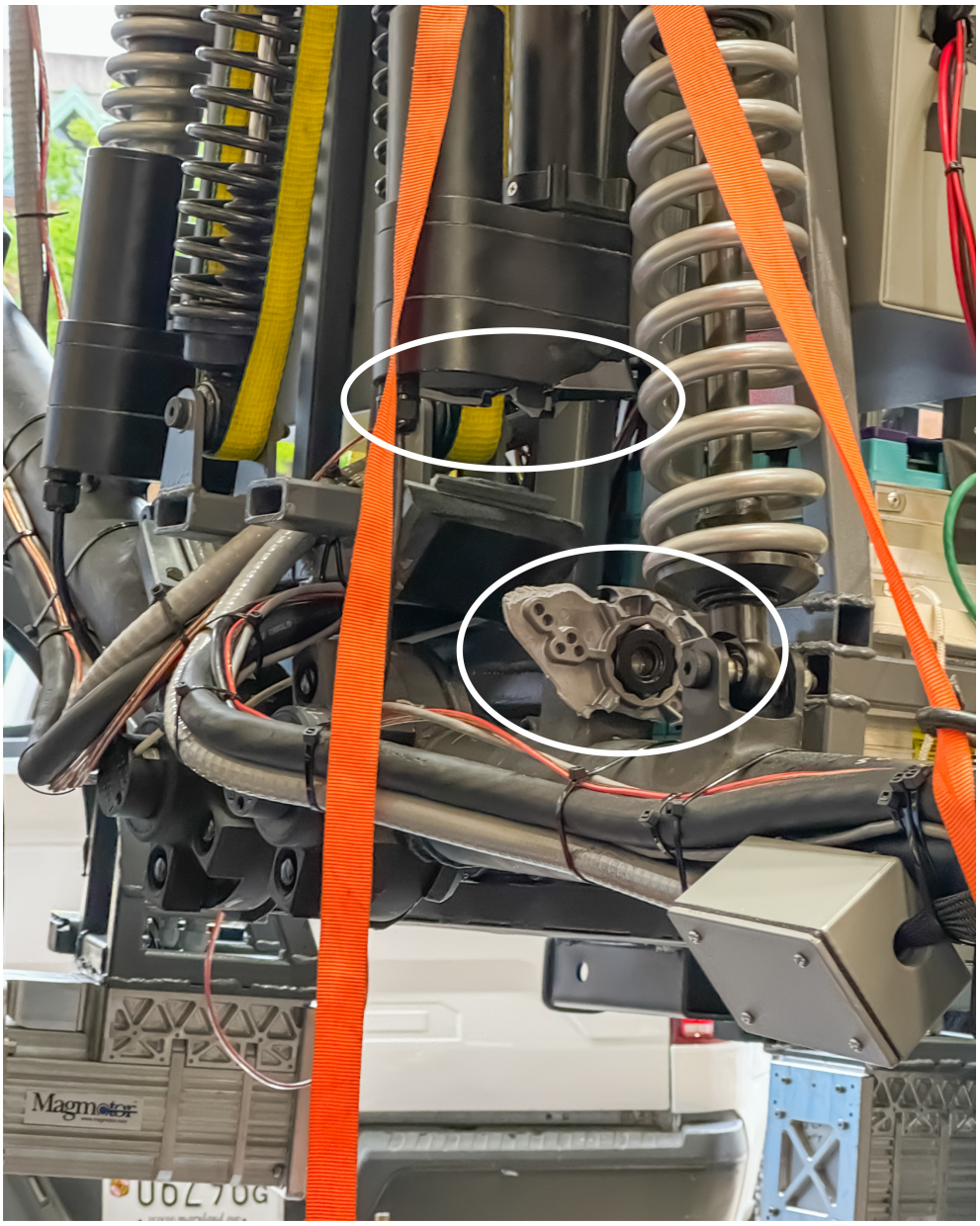

Figure 2.36: Failure of the linear actuator structural housing after crane lift. The two pieces of the linear actuator are highlighted within the ellipses.

repairs are feasible.

2.6 Conclusion

The application of a quasi-static force analysis using a sum-of-moments approach has demonstrated its effectiveness in evaluating and generating valid suspension designs for planetary surface rovers. This methodology enables a detailed prediction of suspension performance under varying loading conditions, providing a robust, computationally-efficient framework for developing systems that enhance rover stability and mobility.

The close alignment between the theoretical model and empirical force data for the series-elastic element validates this modeling approach as a high-level optimization tool. The efficiency of the sum-of-moments approach, grounded in the kinematics of the suspension system, makes it particularly suited for early design iterations. This allows for rapid evaluation and refinement of critical parameters including component placement, spring rates, preload, and crossover points.

Once a stable and kinematically sound configuration is achieved, dynamic analyses should be conducted to fine-tune the system. This step will ensure the suspension provides sufficient isolation of the chassis from harsh surface disturbances, optimizing the rover's operational performance in extreme environments. By combining quasi-static and dynamic modeling, future rover designs can achieve an balance between stability, mobility, and durability in supporting mission success across diverse planetary terrains.

Chapter 3: Lagrangian Formulation

The content in chapters 3 and 4 has been written as a stand-alone paper to be submitted shortly after the culmination of this thesis.

Contributions In This Chapter This chapter focuses on the development of a dynamics modeling approach for articulated suspension systems with passive spring damping. Specifically, the system presented, BioBot, is highly nonlinear and requires consideration of many real-world conditions such as tension restrictions, bushing modeling, and nonlinear friction. The path behind the formulation is presented with the intent to allow the same approach to be taken with other systems, possibly similar or dissimilar to the kinematic configuration of the example rover but still result in a robust set of equations to capture the system behavior.

3.1 Introduction

Articulated suspension systems are a practically advantageous niche that significantly increase stability margins when climbing slopes, manipulating large payloads, and allow advanced locomotion in uncertain terrain [77]. A handful of rovers use articulated suspension systems in varying configurations for both flight missions and Earth-based testing. NASA's VIPER (Volatiles Investigating Polar Exploration Rover) uses independent articulation of each wheel to adjust chassis orientation and track width to increase mobility in rocky conditions without the use of passive dampers [18]. Carnegie Mellon University's Scarab vehicle applies body-averaged suspension linkages that enable chassis height and roll articulation in a stiff configuration, facilitating the precise positioning of a chassis-mounted lunar ice drill while retaining classic locomotive benefits [25]. Similarly, the SherpaTT platform, developed at DFKI (Deutsches Forschungszentrum für Künstliche Intelligenz), utilizes a wheel-on-limb articulation system and an integrated force-torque sensor to deliver multiple control modalities, including roll/pitch correction, force balancing, and simulated spring-damper behavior — all without physical passive elements [26].

NASA's Resource Prospector suspension was actively articulated and included passive spring damping in the articulation mechanism [20]. Each wheel is independently articulated to allow for chassis height, roll, and pitch compensation, and the revolute actuator responsible for this capability is allowed to move and compress a spring system to provide the passive reactionary element. Although integrating a spring-damper element mitigates shock loads and high-frequency disturbances, it also adds complexity to the overall system and poses additional mechanical design challenges. In future platforms such as NASA's upcoming lunar terrain vehicle (LTV), these components become even more critical due to prolonged operation at appreciable speeds on the

lunar surface.

Figure 3.1: BioBot concept during first field trial

Suspension design and analysis techniques for planetary rovers have often been adapted from conventional automotive methodologies [17, 51, 52] or derived from kinematic-heavy paradigms such as the traditional rocker-bogie approach [41–50]. Techniques for advanced suspension design focusing on high ranges of articulation and the inclusion of passive spring damping for impact attenuating and stability at higher speeds are often derived from a vehicle's own special considerations [55–57].

In response to this gap, the present paper introduces a generalized framework for analyzing and refining independently articulated suspension systems equipped with passive spring-dampers, offering broad applicability across diverse rover platforms. The proposed example system further addresses commonly overlooked real-world complexities, such as the inability to tension most

commercial dampers, bushing compliance, as well as the presence of nonlinear geometry and damping characteristics. The analysis of the example roving vehicle shown in this paper uses imperial units as most damper systems, linear actuators, and springs sold commercially within the United States use customary units.

The system evaluated in this paper uses a real-world suspension system developed for the University of Maryland (UMD) Space Systems Laboratory's (SSL) BioBot concept. BioBot is an Earth-analogue LTV prototype focused around alleviating metabolic strain on astronauts during Extravehicular Activities (EVAs) by providing a vehicle capable of climbing and leveling the chassis on 30° slopes, carrying life support systems, and supporting a 5-meter umbilical-tending robotic manipulator. VERTEX (Vehicle for Extraterrestrial Research, Transportation, and EXploration) is the moniker for the roving vehicle, and the umbilical-tending arm on top is named ARMLiSS (Active Rover Mounted Life Support System) which sum to create BioBot. VERTEX was originally designed for a set of lunar surface requirements, and then the form factor was maintained while all actuation systems were redesigned to meet the same requirements, while being affordable, in Earth gravity. The result is a vehicle that weighs four times as much but can climb and level its chassis on slopes in excess of 30° in any direction and carry a full simulated EVA payload for high-fidelity field trials in 1G. Figure 3.1 shows BioBot during the initial field testing with the suspension at nominal drive height.

3.2 Method

This section describes a Lagrangian-based modeling approach that consolidates complex geometric relationships into functions suitable for numerical integration through kinematic def-

initions. As shown in Equation 3.1, the Lagrangian L is the difference between the system's kinetic energy and potential energy:

$$L = T - V \tag{3.1}$$

The Euler-Lagrange equation (Equation 3.2) then provides an avenue to relate partial derivatives of the Lagrangian with generalized forces. These generalized forces must be expressed in terms of a chosen coordinate. In the present work, the generalized coordinate q_i is the swingarm angle θ. Non-conservative forces, such as ground reaction and damping, must therefore be converted into torques about the swingarm pivot.

$$\frac{d}{dt}\left(\frac{\partial L}{\partial \dot{q}_i}\right) - \frac{\partial L}{\partial q_i} = Q_i \tag{3.2}$$

As shown in section 3.3, these quantities need to be kept in terms of the generalized coordinate and any other non-static kinematic values to be numerically iterable. Once these derivatives are computed, individual terms can be rearranged to satisfy Equation 3.3 and then propagated using numerical methods.

$$F = m\ddot{q} \tag{3.3}$$

Figure 3.2 depicts the independently articulated suspension system of the BioBot platform. For clarity, a quarter-car spring-damper diagram is shown in Figure 3.4, identifying the key high-level parameters used in the Lagrangian formulation.

Primary Components:

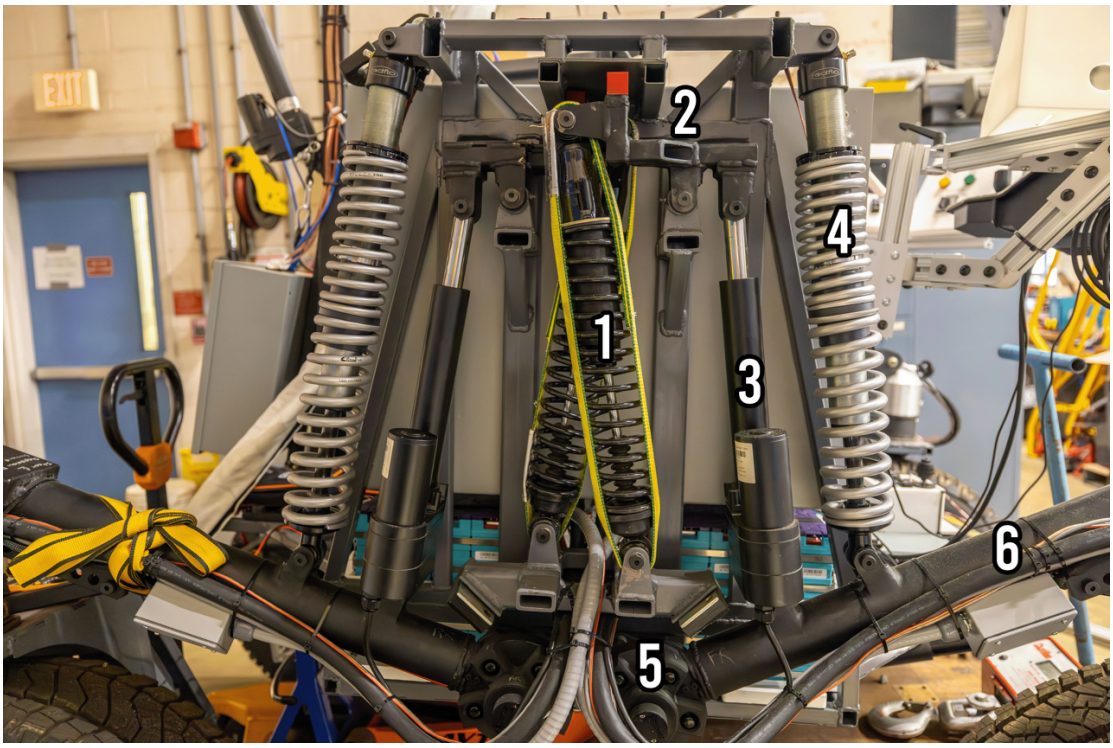

Figure 3.2: VERTEX suspension system high-level diagram

1. Commercial spring-damper unit with retention mechanism (Series Elastic Element — SEE)
2. Pivot between the linear actuator and the elastic element
3. Linear actuator
4. Gravity-offload (GO) spring-damper system
5. Swingarm rotation point with absolute encoder
6. Swingarm

Figure 3.3 offers an alternate perspective on the rover's nominal driving setup. The swingarms (component 6) rotate from 45° above horizontal to 13.8° below horizontal around the pivot (component 5). Components 1, 2, and 3 together form the series-elastic actuator (SEA) that drives

Figure 3.3: BioBot alternate vide

this motion. While a simple series elastic actuator like this may provide enough force to articulate a lunar-grade rover of equivalent size on the moon, the weight on Earth with the heavier systems is too great for actuators within BioBot's budget and additional hardware had to be designed in. For an overview of the multi-iterative suspension engineering path please reference a previously published paper Hanner et al. [78]. In summary, a commercial off-road racing shock absorber is implemented in the latest generation, element 4 in Figure 3.2. This commercial unit offers multiple adjustment capabilities (gas pressure, multistage spring rates, crossover points, and preload), which allows fine-tuning of vehicle response over various payloads, terrains, and mission requirements.

The complete BioBot system weighs approximately 2600 lbs ($\sim$1180 kg) comprised of the VERTEX rover and the ARMLiSS manipulator. For suspension analysis purposes, the to-

tal mass is categorized into three principal segments: unsprung, swingarm, and sprung mass. The unsprung mass includes the wheel, steering actuators, and associated hardware (250 lbs or ∼114 kg per wheel). Each swingarm weighs around 50 lbs (∼23 kg) based on welded steel tube and machined joints. The sprung mass (the chassis, battery pack, control electronics, and human interfaces) weighs approximately 1400 lbs (∼635 kg). Unsprung masses were measured directly using crane scales, the swingarm mass was estimated from CAD, and the sprung mass was estimated via subtraction from a total measured weight.

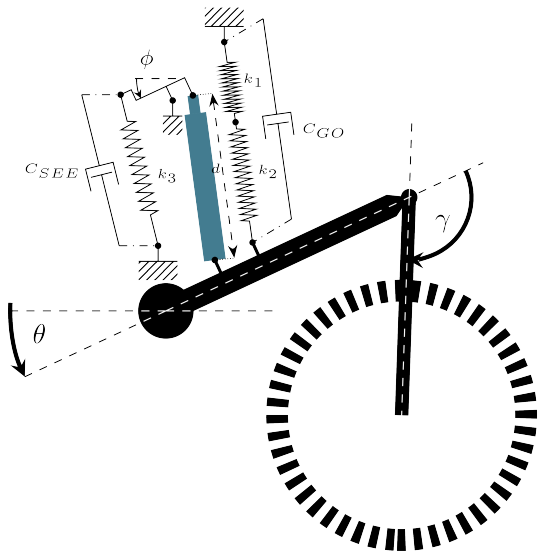

Figure 3.4: Variable-Labeled BioBot Suspension Illustration

Table 3.1: Variables in Figure 3.4 from left to right

Parameter	Unit	Description
θ	rad	Swingarm angle measured from horizontal
C_{SEE}	$\frac{lbf \cdot s}{in}$	Damper coefficient of series elastic element
k_3	$\frac{lbf}{in}$	Spring constant for series elastic element
ϕ	rad	Angle of suspension transfer lever
d	in	Linear actuator length
k_1	$\frac{lbf}{in}$	Upper spring constant for gravity offset springs
k_2	$\frac{lbf}{in}$	Lower spring constant for gravity offset springs
C_{GO}	$\frac{lbf \cdot s}{in}$	Damper coefficient of gravity offset spring system
γ	rad	Angle between swingarm and steering axis

A to-scale spring-damper diagram of the suspension system is shown in Figure 3.4 featuring dimensions and directions relevant to the formulation of energy quantities used in the Lagrangian. Kinematic relations are highlighted later in section 3.3 as they are more relevant to specific applied computation. The assumed distribution of point masses within the vehicle are

shown in Figure 3.5 with the following locations:

- Sprung mass - set (x, y) offset from swingarm hub
- Unsprung mass - assumed concentrated at wheel center
- Swingarm - swingarm midpoint assumption

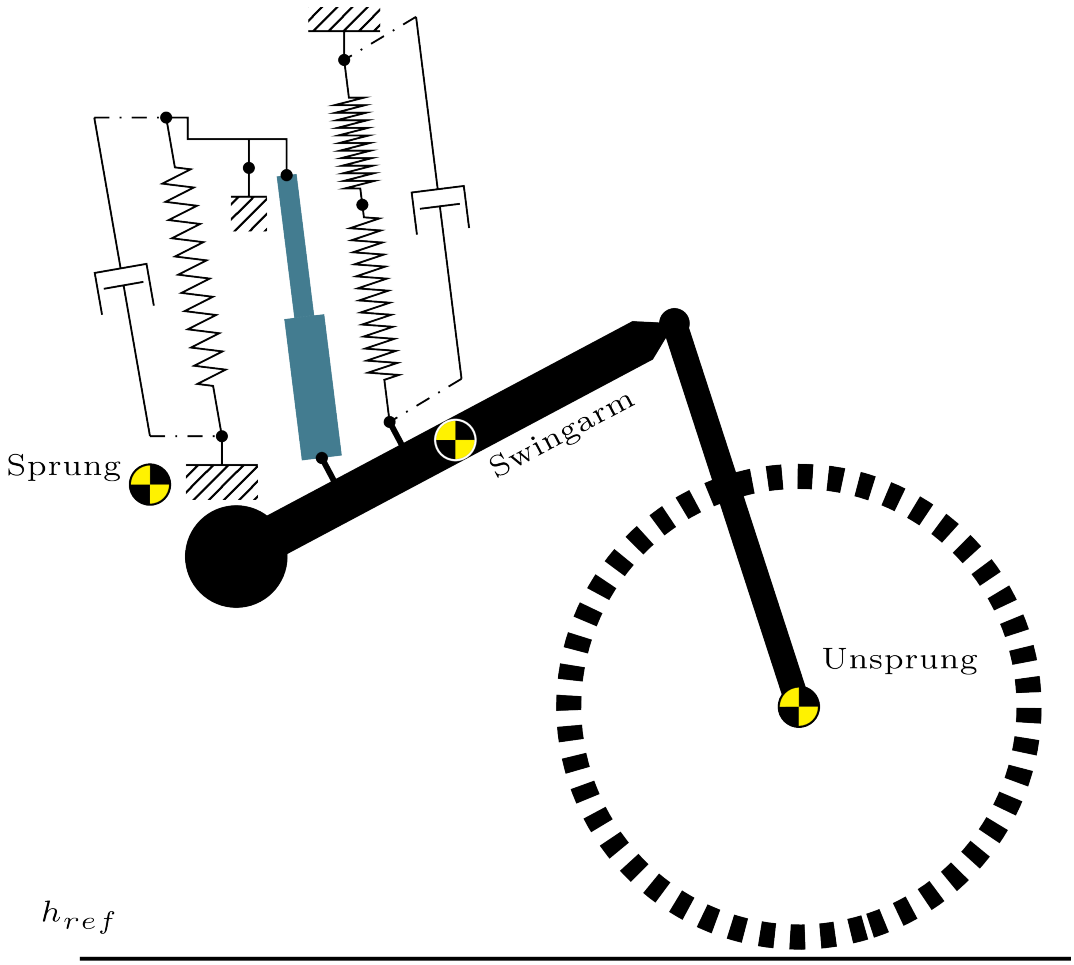

Figure 3.5: CG allocation diagram

A single-corner (i.e., quarter-car) model is appropriate because the VERTEX suspension is fully independent at each wheel. Any half-car or full-car simulation would simply replicate individual corner models, each with unique loading conditions. In this paper, the ground is presumed

flat, and each corner supports one-quarter of the total sprung mass. Asymmetric loading, steep slopes, or large cantilevered payloads (such as ARMLiSS) ultimately adjust the sprung mass of the vehicle. Alternate loading configurations in these conditions can be simulated in this modeling approach by adjusting the portion of the sprung weight that the vehicle corner is responsible for supporting. At a high level, three quantities must be defined: kinetic energy (T), potential energy (V), and non-conservative forces (Q_i).

3.2.1 Kinetic Energy

The total kinetic energy comprises contributions from the sprung mass (denoted s), unsprung mass (denoted us), and swingarm (denoted sw) components as shown in Equation 3.4.

$$T = \frac{1}{2}\frac{m_s}{4}v_s^2 + \frac{1}{2}m_{us}v_{us}^2 + \frac{1}{2}I_{sw}\omega_{sw}^2 \tag{3.4}$$

For the swingarm, the rotational velocity ω_{sw} about the pivot is assumed to be dominant. The arm itself is modeled approximately as a hollow cylinder of length l_{sw}. Thus, the swingarm moment of inertia is:

$$I_{sw} = \frac{m_{sw}}{12}(3(r_{sw_{outer}}^2 + r_{sw_{inner}}^2) + l_{sw}^2) \tag{3.5}$$

3.2.2 Non-Conservative Forces

In the Lagrangian method, non-conservative forces (e.g. damping, ground contact forces) must be expressed as generalized forces with respect to the chosen coordinate θ. In BioBot, three main damping sources are considered:

1. Gravity-offset spring-damper (GO)

2. Series-elastic element (SEE)

3. Pivot friction within the main swingarm axle

.

Linear Damping:

The gravity offload springs are damped with a pressurizable nitrogen cylinder along the centerline of the springs whereas the series elastic element has a set, unknown, damping coefficient from the factory. Initially each source was presumed to be linear. The generalized torque due to linear damping can be summed as:

$$Q_{\text{LinDamping}} = \sum_{i} -c_i v_i l_i S_{i_{\text{Loss}}} \quad i \in \{\text{GO}, \text{SEE}\} \tag{3.6}$$

where c_i is the damping coefficient, v_i is the linear velocity at the respective damper, l_i is the respective lever arm the component acts on respective to the swingarm pivot, and $S_{i_{\text{Loss}}}$ is a generalized term representing the sine and cosine losses that the kinematics of the system dictate. These losses contribute significantly to the design difficulty and are discussed further in section 3.3 Applied Calculation.

The swingarm pivot uses a 3500 lb commercial trailer axle that relies on a pair of tapered roller bearings to constrain the motion. A combination of the high preload required on these bearings with the thick waterproof grease used in the assembly process results in a pivot that has a very noticeable amount of friction. The rotational damping in the swingarm pivot is added as:

$$Q_{\text{RotDamping}} = -c_{PVT}\dot{\theta} \tag{3.7}$$

Where the rotational damping coefficient about the swingarm pivot, c_{PVT} ($\frac{ft-lb\cdot s}{rad}$), is linearly related to the swingarm angular velocity.

Ground-Reaction Force:

The total ground force at the wheel is resolved into two major components: one along the swingarm length and one along the "over-wheel structure" (OWS). Each component exerts a different moment about the swingarm pivot, as indicated in Figure 3.6:

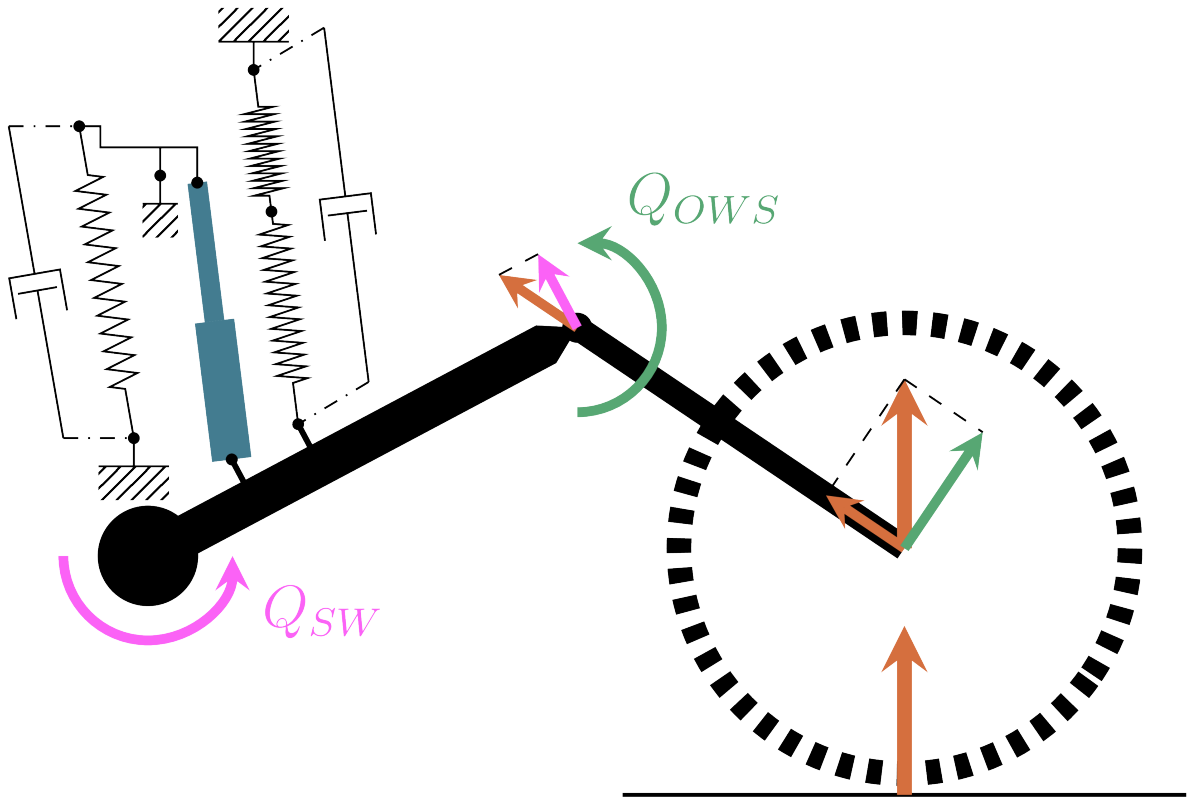

Figure 3.6: Ground force vector decomposition to moments about the generalized coordinate

$$Q_{GroundForce} = Q_{SW} + Q_{OWS} \tag{3.8}$$

Equation 3.8 sums both moments as the moment applied at the swingarm tip can be considered to be applied around the center of rotation for the point.

$$Q_{tot} = Q_{GroundForce} + Q_{RotDamping} + Q_{LinDamping} \tag{3.9}$$

3.2.2.1 Nonlinear Damping

Early system identification revealed significant discrepancies if purely linear damping was assumed. Consequently, nonlinear formulations were introduced to replace the original linear terms for the same three damping sources mentioned above.

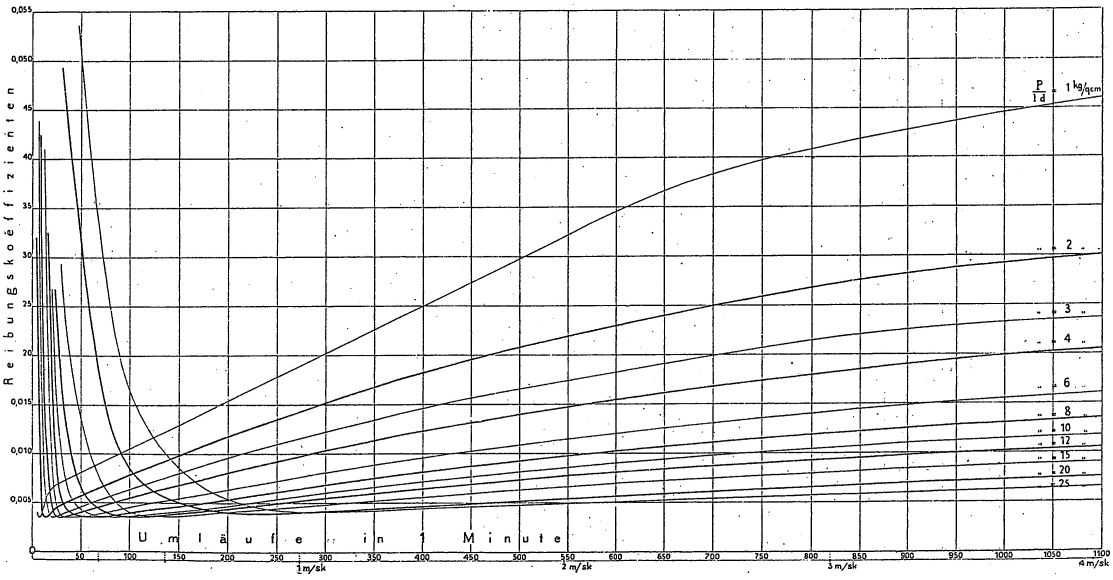

Figure 3.7: Stribeck's curve "Coefficient of friction (Reibungskoeffizienten) versus revolutions per minute (Umlaufe in 1 min) at different loads (T = 25° C, dia shaft = 70 mm, P_{Geom} = 0.1–2.0 MPa, oil for gas powered engines $\eta \approx 180$ mPa s)." [79]

(1) Swingarm Pivot - Stribeck Friction Model Highly viscous or greased bearings often obey Stribeck-like friction. This model features a higher friction coefficient at low speed (boundary lubrication) that decreases with velocity, followed by a subsequent increase in the hydrodynamic

regime as seen in Figure 3.7 [**martonControlMechanicalSystems2009**, **woydtHistoryStribeckCurve2010a**].

For a rotating joint with velocity $\dot{\theta}$:

$$Q_{\text{Stribeck}}(\dot{\theta}) = \sigma\,\dot{\theta} \;+\; \text{sgn}\big(\dot{\theta}\big)\Big[F_c \;+\; \big(F_s - F_c\big)\,e^{-\left(\frac{|\dot{\theta}|}{v_s}\right)^{\delta}}\Big] \tag{3.10}$$

where σ is the viscous coefficient, F_s is static friction, F_c is Coulomb friction, v_s is a reference velocity, and δ controls how quickly friction transitions near $\dot{\theta} = 0$.

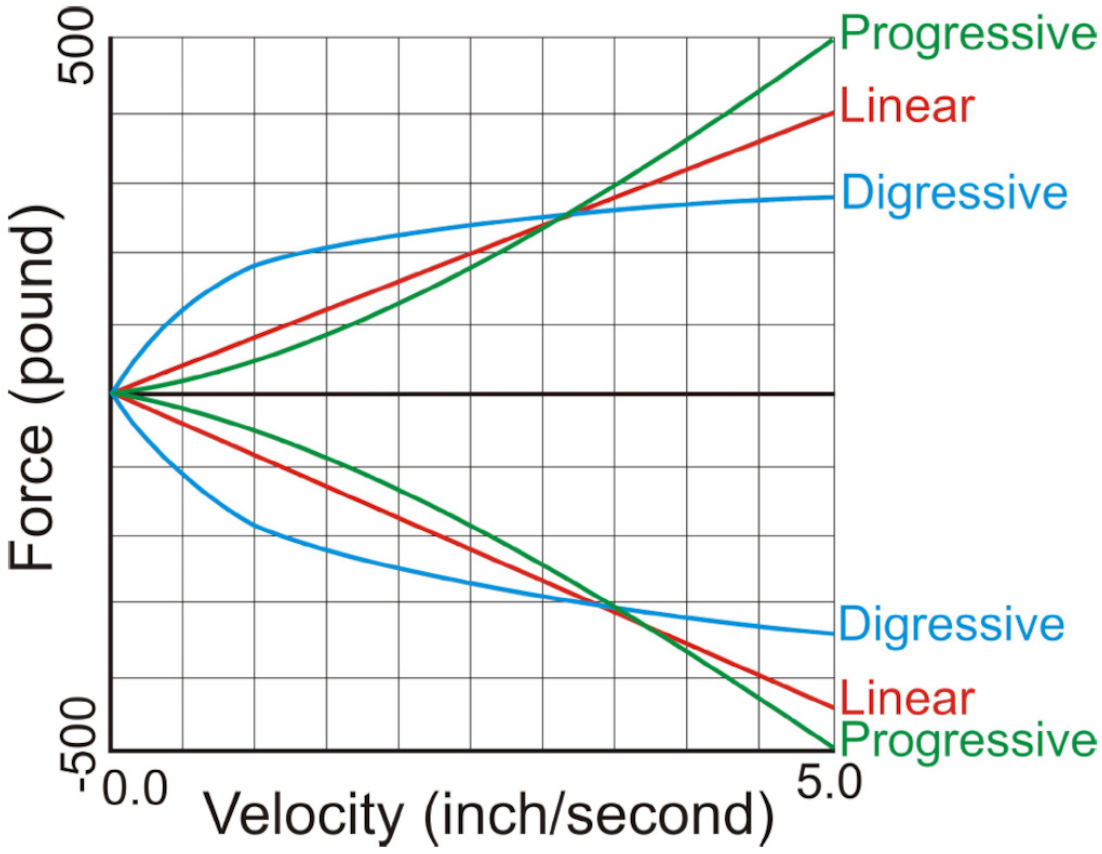

Figure 3.8: Illustration showing a set of example example linear, progressive, and digressive profiles [80]

(2) Gravity-Offset Damper Commercial shock absorbers typically fall into one of three categories: linear, progressive, or digressive [80] (see Figure 3.8). Their force-velocity curve can be approximated with an exponential relationship:

$$F_{\text{expGO}}(\dot{\theta}) = -c_{GO} \left|\Delta \dot{d}_{GO}\right|^{n+1} \operatorname{sgn}\left(\dot{\theta}\right),$$

where c_{GO} is a damping coefficient, $n \in (-1, 1]$ adjusts non-linearity, and $\Delta \dot{d}_{GO}$ is the damper's linear velocity (as a function of θ and $\dot{\theta}$). The corresponding torque on the swingarm includes geometric factors such as lever arms and any sine/cosine losses:

$$Q_{expGO} = F_{\text{expGO}}\ sin(\angle(\overrightarrow{SW}, \overrightarrow{GO}))\ l_{swGO}$$

(3) Series-Elastic Element The elastic element also provides an element of damping when compressing or rebounding. As the specific damping characteristics of the integrated damper are not known, nor are the damping effects of the pivot rotating in the rubber bushing used, an *effective* damping coefficient can be defined for this rotational motion. The damping model can be defined around the pivot angle velocity $\dot{\phi}$, including a nonlinear exponent:

$$Q_{SEE\,exp} = l_{sw\,a}\ c_{SEE}\ \dot{\phi}^{n_{SEE\,damp}+1}$$

The exponent of $\dot{\phi}$ is included to account for the possibility, or rather likelihood, the damping about the pivot is nonlinear both in the damping and rotational bushing motion components.

Note, it is required that ϕ and $\dot{\phi}$ be formed as a function of θ in the final application of this equation to the system kinematics. In doing so, the sine losses on both ends of the linear actuator are considered in this formulation and is one of the principal reasons behind choosing this "effective characteristic" method alongside the unknown characteristics of the two potential sources of damping here.

Nonlinear Damping Total The total sum of the nonlinear damping terms is as follows:

$$Q_{tot} = Q_{GroundForce} + Q_{Stribeck} + Q_{expGO} + Q_{SEE\,exp} \tag{3.11}$$

It should also be noted here that in response to the discovery of a significant *velocity-direction*hysteresis, discussed in more detail later in section 4.1.1, each of these damping terms are separated into sets of separate positive and negative velocity coefficients. For example, c_{GO}, the damping coefficient for the exponential damping of the gravity-offset system is split into c_{GO+} and c_{GO-} dependent on the velocity direction.

3.2.3 Potential Energy

The potential energy for the system is the sum of the gravitationally-dependent and spring-force energy values. The gravity terms are simple and use a reference origin point on the planetary surface for the height terms.

$$V_{\text{gravitational}} = \sum_i m_i g h_i \quad i \in \{S, US, SW\} \tag{3.12}$$

Equation 3.12 shows this summation across the set of sprung (S), unsprung (US), and swingarm (SW) masses as shown in 3.5.

3.2.3.1 Gravity Offset Springs

While the gravitational energies are simple factors, the spring-based factors bring significant additional complication due to their physical characteristics and limitations. Beginning with

the gravity-offset spring system will provide context to the calculations required for the series elastic element. Figure 3.9 labels the features of the dual-rate spring damper hardware that the energy calculations must consider.

Figure 3.9: Labeled photo of the gravity offset damper from Radflo Suspension Technology, Inc.

1. Lower structural connector
2. Lower spring retention ring
3. Spring-spring interface slider
4. Crossover rings
5. Preload rings
6. Upper structural connector

The damper has a length of 35.43 inches measured from the mounting points at full extension and has 14 inches of travel available in the damper. The damper is designed to support a pair of 14-inch springs with the lower spring mounted between the lower connector (2) and the interface slider (3), and the upper between the same interface slider and the preload rings (5). VERTEX has had two configurations of springs over the course of its testing. First was a 150 lb/in upper and 200 lb/in lower set but after the round of field testing determined the suspension was not stiff enough this model was created and an upgraded rate of 200 lb/in upper and 400 lb/in lower was implemented. Although spring rates are adjustable by swapping physical springs in and out of the system, two other adjustable factors are present that greatly change the suspension characteristics: preload and crossover.

Preload, adjusted by physically threading a pair of rings up and down the damper body, increases or decreases the amount of force the system resists before compressing by any Δx amount. As the springs in the system are aligned in series, the equivalent spring rate for two springs in this configuration must be used (Equation 3.13).

$$k_{eq} = \frac{1}{\frac{1}{k_1} + \frac{1}{k_2}} \tag{3.13}$$

$$F_{GO_{preload}} = k_{eq} \Delta x_{preload} \tag{3.14}$$

$$V_{GO_{preload}} = \frac{1}{2} k_{eq} (\Delta x_{preload})^2 \tag{3.15}$$

Equations 3.14 and 3.15 detail the force and potential energy from the distance the rings were threaded down the damper and compressing the springs, $\Delta x_{preload}$. The energy value can be directly included in the system energy model for the Lagrangian, and the force output of this system is required when calculating the energy values associated with the series elastic element later in this section.

Until the gravity offset system is compressed by a critical deflection amount, Δx_{cross}, the springs will continue to act at the combined spring rate and can be treated as a single spring. Δx_{cross} is then defined as the total amount of deflection in the gravity-offset spring system that causes the transition between the combined rate and using just the lower rate. This occurs when the spring interface slider (3) contacts the crossover rings (4) and prevents the upper spring from deflecting further. Figure 3.10 shows the gravity offset system about to hit the crossover point.

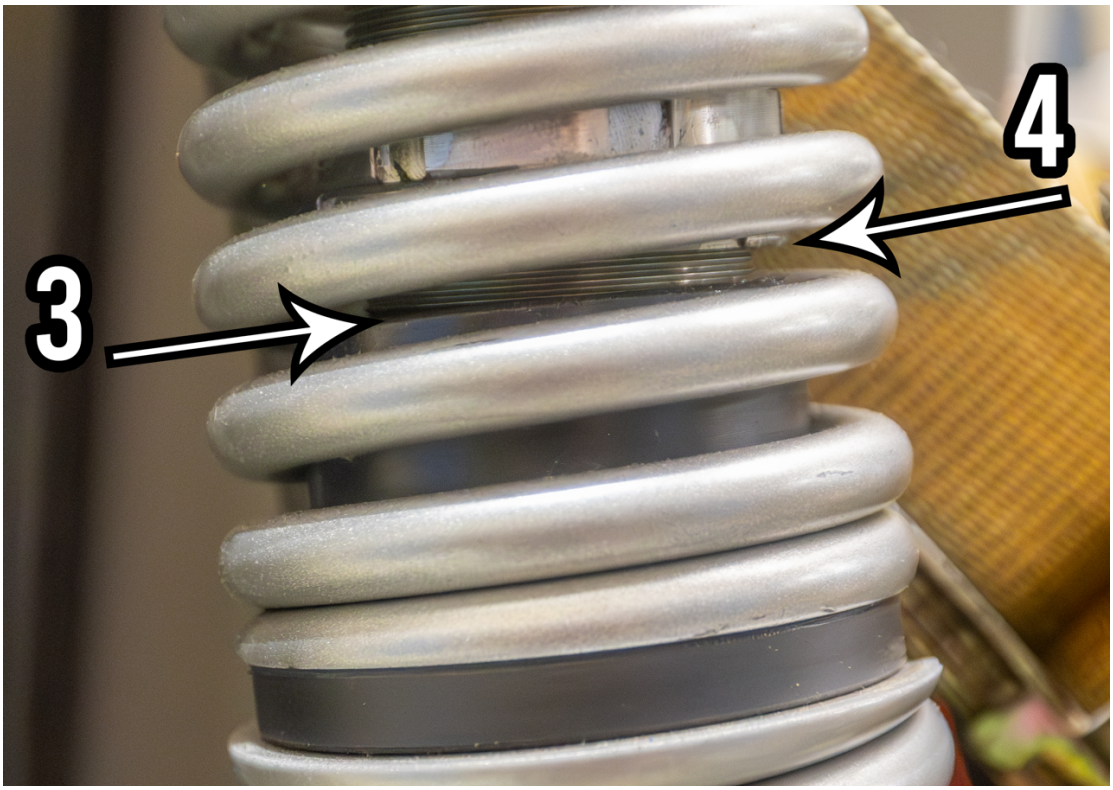

Figure 3.10: Gravity offset system near crossover point

The general Δx represents the linear deflection of the spring system and can be defined kinematically as a function of θ. If $\Delta x \leq \Delta x_{cross}$ then the potential energy and force functions can be calculated as seen in equations 3.16 and 3.17.

$$F_{GO} = k_{eq}\Delta x + F_{preload} \tag{3.16}$$

$$V_{GO} = \frac{1}{2}k_{eq}(\Delta x)^2 + V_{GO_{preload}} \tag{3.17}$$

Alternatively, if $\Delta x > \Delta x_{cross}$ then equations 3.18 and 3.19 must be used.

$$F_{GO} = k_2(\Delta x - \Delta x_{cross}) + k_{eq}\Delta x_{cross} + F_{GO_{preload}} \tag{3.18}$$

$$V_{GO} = \frac{1}{2}k_2(\Delta x - \Delta x_{cross})^2 + \frac{1}{2}k_{eq}(\Delta x_{cross})^2 + V_{GO_{preload}} \tag{3.19}$$

The value Δx_{cross} must be calculated from a given damper configuration, including spring rates, preload, and crossover ring locations. Equation 3.20 shows the distance condition that can be created by combining spring deflections with linear distance measurements and variables which can be manipulated to create a function of d_{CRs} and $\Delta x_{preload}$ for Δx_{cross} as shown in Equation 3.21.

$$\underbrace{2.5625}_{\substack{\text{0 preload} \\ \text{line}}} + \underbrace{14}_{\substack{\text{Upper} \\ \text{spring} \\ \text{length}}} - \underbrace{1.5625}_{\substack{\text{Connector} \\ \text{in spring}}} + \underbrace{\frac{\Delta x_{preload}k_{eq}}{k_2}}_{\substack{\text{Preload defl. of} \\ \text{lower spring}}} - \underbrace{\frac{\Delta x_{cross}k_{eq}}{k_1}}_{\substack{\text{Upper spring} \\ \text{defl. from } \Delta x}} - \underbrace{d_{CRs}}_{\substack{\text{Crossover ring} \\ \text{measurement}}} = 0 \tag{3.20}$$

$$\Delta x_{cross} = \underbrace{d_{CRs} - (15 + \frac{\Delta x_{preload}k_{eq}}{k_2})}_{\Delta x \text{ required in top spring}} \frac{k_1}{k_{eq}} \tag{3.21}$$

The VERTEX setup conditions for the dynamic validation shown later in section 4.1 are 200 lb/in upper spring rate, 400 lb/in lower spring rate, 1 inch of preload, and the crossover ring distance (d_{CRs}) is set 9.125 inches down the damper measured from the base of the upper structural connector (6). The base of this connector is where the threaded section of the damper ends and as a result is defined as the upper limit of adjustability for the preload and crossover rings. This is then an excellent reference point for this calculation. From this point the preload rings have 2.5625 in of length they can thread down the damper before contacting the springs and beginning the application of preload. Additionally, the sliding interface connector between the

series springs has stickout inside the spring inner diameter that extends 1.5625 in.

3.2.3.2 Series Elastic Actuator

Now that the force of the gravity offset springs can be calculated given a current θ of the system the contribution of the series elastic system can be found. A set of conditions need to be evaluated to determine the current state of this subsystem, the first of which asks if the series-elastic element has been compressed. If the pivot angle (calculated from system kinematics as shown later in Equation **??**) $\phi > 0$ then the element is compressed.

Most commercially available spring dampers, particularly those with long ranges of motion similar to those present in VERTEX, are not rated to withstand tension forces. Tension typically strains the valving within dampers and in scenarios where a vehicle's system must resist tension straps must be added in line with the damper to take these forces before the system is fully extended. VERTEX features two mechanisms, as shown in Figure 3.11, to ensure the series elastic elements are not damaged when tension forces are present in the dampers.

The yellow circumferential strap is the primary retention mechanism and the red bumpers act as a backup. The yellow strap is small enough that the spring damper needs to be compressed by approximately $\frac{1}{4}$ of an inch to fit. The gravity offset springs do not require limiting straps as the kinematics suspension system, even at full extension of the linear actuator, dictate the gravity offset spring be slightly compressed.

The presence of the retention mechanism increases the amount of force that must be applied before the series elastic element begins to compress, effectively increasing the preload. However, since the series elastic element is not guaranteed to always be in compression, as the gravity offset

Figure 3.11: Bushing elements shown in a perspective image of the suspension system. The bushings are seen at the top and bottom connectors for the series elastic element and at the central pivot point between the linear actuator and the SEE.

springs are, the contributions to the equations of motion from the SEA must be conditionally evaluated.

If the damper has not yet been compressed, the total sum of the moments and kinematics can be used to find the force within the series elastic actuator quasi-statically. The moment magnitude for which the linear actuator is responsible to quasi-statically balance the sum of forces, Q_{LinAct}, is found in Equation 3.22. The moment contribution of the gravity offset spring must be discounted by the sine loss of the angle between it and the swingarm, $sin(\angle(\overrightarrow{SW}, \overrightarrow{GO}))$, for the state at which the calculation is made.

$$Q_{LinAct} = Q_{SW} + Q_{OWS} - F_{GO} sin(\angle(\overrightarrow{SW}, \overrightarrow{GO}))l_{GO} \tag{3.22}$$

At this point, another condition needs to be evaluated. If Q_{LinAct} indicates that the series-elastic actuator is in tension, it acts as a resistive *force* and is then not captured by the potential energy of the spring element. This requires an addition of this moment to the non-conservative force total to balance the equations quasi-statically.

$$Q_{tot} = Q_{tot} + Q_{LinAct} \tag{3.23}$$

If the actuator is in compression, this force is captured more standardly via the potential energy equation. The moment must be translated from the linear actuator attachment point and into the force experienced by the series elastic element, involving three main steps as listed below and labeled in Figure 3.11:

1. Account for the sine loss between the linear actuator and the swingarm to find the actual

force in the linear actuator

2. Account for the sine loss between the linear actuator and the pivot in the direction of rotation

3. Translate the force through the pivot and into the series elastic element

Once the force transmitted into the series elastic element is known, the amount of preload that is reacting such force can be calculated. First, the equivalent amount of preload deflection must be calculated as seen in Eqn. 3.24, and then the amount of potential energy this correlates to is calculated as in Eqn. 3.25.

$$\Delta x_{SEE_{preload}} = F_{SEE}/k_{SEE} \tag{3.24}$$

$$V_{SEE_{preload}} = \frac{1}{2} k_{SEE} (\Delta x_{SEE_{preload}})^2 \tag{3.25}$$

If the pivot point has rotated, the preload has been fully overcome and additional Δx was needed to balance the system. Equation 3.26 details the full potential energy in this case.

$$V_{SEE} = V_{SEE_{preload}} + \frac{1}{2} k_{SEE} \Delta x \tag{3.26}$$

One benefit of the Lagrangian that should not be overlooked is that within each iteration pure kinematics can be used to determine which state the series elastic element is in. At all points in time the propagator knows the length of the linear actuator (d) and the swingarm's current state [θ, $\dot{\theta}$]. If the distances between the mounting points for the linear actuator and the pivot

point at 0° of rotation is not within a set tolerance, then the angle of the pivot (ϕ) can be found that satisfies the current state condition and thus the potential energy contribution can be found. This is possible thanks to the Lagrangian's ability to abstract these complex relationships through meticulous maintenance of all kinematic relations as functions of θ.

3.2.4 Compliance Mechanism Considerations

While the system is modeled broadly as a set of rigid bodies, consideration to component flexibility must be taken into account to complete the modeling picture. Primarily the presence of bushings in the SEA pivot structure and at both ends of the SEA damper allow movement beyond the quasi-static limits under dynamic loading.

The series-elastic actuator system is designed to allow travel in the compressive direction of the SEE but limit travel in the other direction. Tensioning the elastic element and most commercially available dampers is likely to damage internal valving and should be avoided. This nominally limits the angle of the pivot ϕ to not travel below 0° and as a result, in theory, the swingarm should not travel below its quasi-static resting position. Looking at Figure 3.11, if the pivot travels counter clockwise, the swingarm will increase in θ. Conversely, if the pivot were to travel clockwise, which great care has been taken to ensure that any movement in this direction is minimized, the swingarm angle would be traveling in a decreasing θ direction. In dynamic testing (as seen and discussed in greater detail in Figure 4.11) it is seen that the swingarm angle does travel briefly below its starting position, indicating some element of compliance exists that must be modeled.

The angle of the pivot is limited by the yellow circumferential retention strap and as a

backup the rigid red stopper blocks as shown in Figure 3.11. Even when the yellow strap stretches, either naturally over time or during shock loading, the damper internals themselves should never be exposed to tension forces. These mechanisms kinematically stop the pivot from rotating clockwise (from the perspective in Figure 3.11) in quasi-static situations, but not designed to be less stiff compared to something like a metal on metal mechanism would be to reduce component stress under dynamic loading. This is also why the interface between the elastic element, the pivot, and the chassis components are designed with stiff rubber bushings. As a result, the suspension under dynamic loading cases avoids excessive shock loading the components in extending and compressing these elements, and allows the pivot rotation point to temporarily rotate by small amounts in the clockwise direction. Other factors such as bending of the swingarm tube, steel structure of the pivot, and the chassis itself are surely present as the suspension articulates and is subjected to varying forces, but for this analysis these elements are grouped with the bushing and retention mechanism effects.

The selected approach to characterize and model the total effects from the compliance mechanisms is to segment their impact into two categories: restorative force and damping. The restorative force condition is handled in Equation 3.23, and a separate set of damping conditions needs to be created. The three conditions where the presence of rubber bushings, limit straps, or rubberized hardstops have an impact on the system's motion:

1. Bushing lower bound - ϕ rotates clockwise, attempting to overextend SEE ($\phi < 0$)

2. Bushing upper bound - ϕ rotates counter-clockwise into the rotational limit ($\phi > \phi_{max} = 45°$)

3. Swingarm hard stop - θ exceeds upper $\theta_{max} = 45°$ kinematic limit (contacts rubberized

hard stop)

For all three approaches, the same approach is taken with three sets of coefficients. The bushings are modeled wholistically as a linear spring-damper, with the forces applied at the linear actuator mounting point on the swingarm.

For the lower bound and upper bound of the bushing, since they affect the same component, the same set of equations is used, just activated differently depending on the conditions met.

1. **SEA Bushing (Lower Side, when $\phi < 0$):**

$$V_{\text{SEA, lower}} = \frac{1}{2} k_{\text{SEA}} \left(\min(0, \phi)\, l_m\right)^2$$

where k_{SEA} is the SEA bushing stiffness and l_m is the effective actuator mounting length.

2. **SEA Bushing (Upper Side, when $\phi > \phi_{\max}$):**

$$V_{\text{SEA, upper}} = \frac{1}{2} k_{\text{SEA}} \left(\max\{0,\, \phi - \phi_{\max}\}\, l_m\right)^2$$

3. **Hard stop bushing (when $\theta > \theta_{\max}$):**

$$V_{\text{HardStop}} = \frac{1}{2} k_{\text{upper}} \left(\frac{l_m}{2}\, \max\{0,\, \theta - \theta_{\max}\}\right)^2$$

with k_{upper} being the hard stop bushing stiffness.

The total bushing potential energy is then:

$$V_{\text{bushing}} = V_{\text{SEA, lower}} + V_{\text{SEA, upper}} + V_{\text{super}}$$

To handle the differential damping rates between the positive and negative velocity conditions, the following effective rate equation can be used:

$$c_{\text{eff}}(v) = \frac{1}{2}\big(c_{\text{pos}} + c_{\text{neg}}\big) + \frac{1}{2}\big(c_{\text{pos}} - c_{\text{neg}}\big)\ \operatorname{sgn}(v)$$

Let $H(x)$ denote the Heaviside step function:

$$H(x) = \begin{cases} 1, & x > 0, \\ \\ 0, & x \leq 0 \end{cases}$$

Then the damping torques contributed by the bushings are:

1. **Lower SEA Bushing Damping (active when $\phi < 0$):**

$$Q_{\text{damp, lower}} = -\, c_{\text{SEA,eff}}\, \dot{\phi}\, H(-\phi)\, l_m$$

2. **Upper SEA Bushing Damping (active when $\phi > \phi_{\max}$):**

$$Q_{\text{damp, upper}} = -\, c_{\text{SEA,eff}}\, \dot{\phi}\, H\big(\phi - \phi_{\max}\big)\, l_m$$

3. **Hard Stop Damping (active when $\theta > \theta_{\max}$):**

$$Q_{\text{damp, hard stop}} = -\, c_{\text{upper,eff}}\, \dot{\theta}\, H\big(\theta - \theta_{\max}\big)$$

The total non-conservative bushing damping force is given by:

$$Q_{\text{nc,bushing}} = Q_{\text{damp, lower}} + Q_{\text{damp, upper}} + Q_{\text{damp, hard stop}}$$

These totals are then added to the potential energy and non-conservative force totals.

$$V_{tot} += V_{bushing}$$

$$Q_{tot} += Q_{nc,bushing}$$

3.2.5 Lagrangian Approach Summary

The Lagrangian allows for approachable consideration of real-world limitations in the VERTEX actuation system including as-discussed multiple spring rates in series, variable crossover points, and the inability of the spring damper systems to resist tension loading. These considerations are not common in most approaches and ultimately require the creation of a piecewise set of differential equations describing the system across its different regimes of the swingarm range of motion. The flowchart as seen in Figure 3.12 is used to select which Lagrangian equation, from table 3.2 to use for any given suspension state.

A separate Lagrangian summation is found for each of these conditions, using the kinematics of the suspension system to leave only θ, $\dot{\theta}$, and d as variables to evaluate across a specified iteration timeframe. After computing the derivatives of each of the six Lagrangians as specified in Equation 3.2 individual terms can be arranged to satisfy the form of Equation 3.27. This form

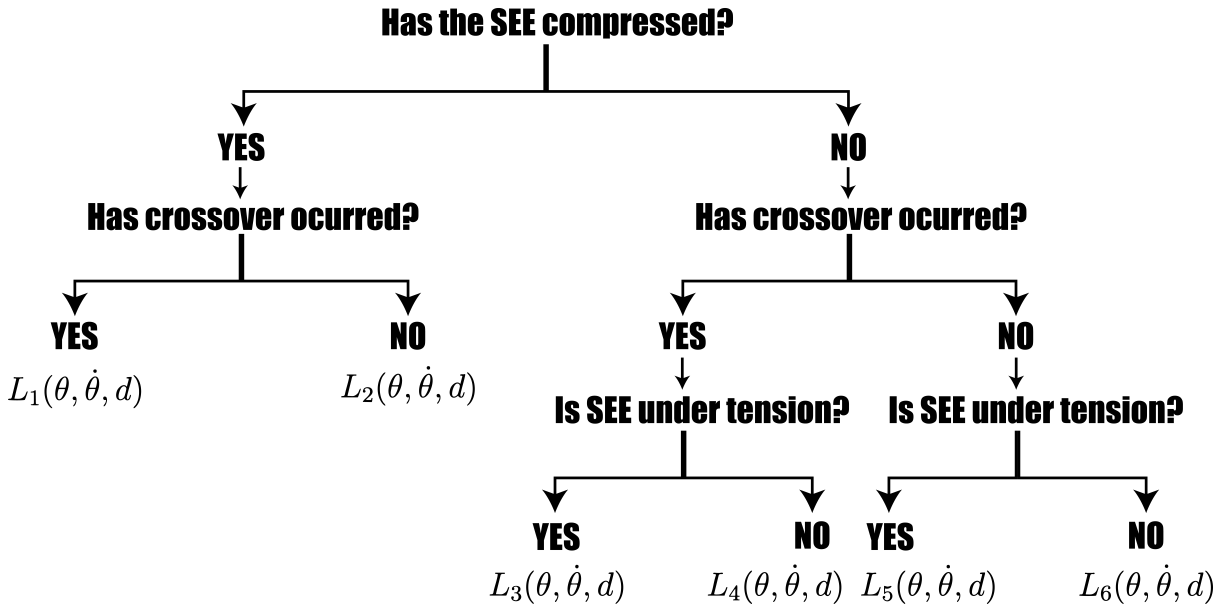

Figure 3.12: Flowchart for selecting which Lagrangian equation to use

Table 3.2: Regimes for the Lagrangian formulation based on pivot motion, crossover, and tension conditions.

Case	Pivot	Crossover	Tension	Lagrangian
1	Yes	Yes	No	$L_1(\theta, \dot{\theta}, d)$
2	Yes	No	No	$L_2(\theta, \dot{\theta}, d)$
3	No	Yes	Yes	$L_3(\theta, \dot{\theta}, d)$
4	No	Yes	No	$L_4(\theta, \dot{\theta}, d)$
5	No	No	Yes	$L_5(\theta, \dot{\theta}, d)$
6	No	No	No	$L_6(\theta, \dot{\theta}, d)$

can then be trivially solved using the inverse for the derivative of the state vector ($[\dot{\theta}; \ddot{\theta}]$) and subsequent numerical propagation.

$$\begin{bmatrix} 1 & 0 \\ 0 & M_{i_{(2,2)}} \end{bmatrix} \begin{bmatrix} \dot{q} \\ \ddot{q} \end{bmatrix} = \begin{bmatrix} 0 \\ F_i \end{bmatrix} \tag{3.27}$$

The numerical propagation process uses a wrapper for the six different sets of equations of motion that evaluates the suspension state at each propagation step to understand which condi-

tions are appropriate between the pivot motion, GO crossover, and linear actuator tension. Once an EOM is selected it can be numerically evaluated using an ODE solver for another step.

3.3 Applied Kinematics

The set of T, V, and Q_i equations created in Section 3.2 form the theoretical basis for creating the equation of motion from the Euler-Lagrange equation, the Lagrangian needs to be expressed in terms of system kinematics and as a function of our generalized coordinate θ. The examples shown below highlight this process of kinematic translation using subterms of reasonable length to show in this publication.

It should be noted all θ and $\dot{\theta}$ values are of course functions of time, but the notation has been simplified by removing (t) to better appear in this format.

3.3.1 Potential Energy - Gravity Offset Springs

Equation 3.28 details the potential energy in the gravity-offset springs under the condition that they have reached crossover. The equation is simplified if the crossover condition has not been met as all deflection in that case is accounted for with the combined spring rate.

$$PE_{GO} = \frac{1}{2}K_{GO\,\text{lower}}\Bigg(-x_{\text{cross}} + \Bigg|l_{\text{uncomp. GO}} - \sqrt{\begin{matrix}(-h_{sw_m}\sin(\theta) + l_{sw_m}\cos(\theta) - x_{ch_m})^2 + \\ +\,(h_{sw_m}\cos(\theta) + l_{sw_m}\sin(\theta) - y_{ch_m})^2\end{matrix}}\Bigg|\Bigg)^2 + \\ + \frac{\frac{1}{2}x^2_{\text{preload GO}}}{\frac{1}{K_{GO\,\text{upper}}} + \frac{1}{K_{GO\,\text{lower}}}} + \frac{\frac{1}{2}x^2_{\text{cross}}}{\frac{1}{K_{GO\,\text{upper}}} + \frac{1}{K_{GO\,\text{lower}}}} \tag{3.28}$$

This equation is comprised of a set of calculated distances and length differences surrounding the crossover point but written as a function of θ. Two frames, one static and one rotating, are needed for the calculation, the first handles the motion of the mount for the GO springs on the swingarm (l_{sw_m} for mounting length longitudinally down the swingarm, and h_{sw_m} for mounting height above the swingarm centerline), and the second is the fixed upper mounting point on the chassis (x_{ch_m}, y_{ch_m}). The uncompressed length of the gravity offset springs ($l_{\text{uncomp. GO}}$), displacement required to contact the combined rate/lower rate changeover point (x_{cross}), and the spring rates ($K_{GO\,\text{upper}}$ and $K_{GO\,\text{lower}}$) are all required quantities, and were defined as shown in Figure 3.13.

3.3.2 Sprung, Unsprung, and Swingarm - K.E. & P.E.

3.3.2.1 P.E. Unsprung Mass

The ground plane is used as the reference height for the gravitational potential energy. In the unsprung case, the masses are assumed to be centered at the wheel center and maintain a constant distance from the ground. Equation 3.14 is the applied form following the general form of Equation 3.12.

$$PE_{US} = m_{US} * g * r_{wheel} \tag{3.29}$$

3.3.2.2 P.E. Sprung Mass

Using the ground as the logical reference frame for the sprung mass requires transformations to be made between the swingarm origin and the ground contact point. The frame assign-

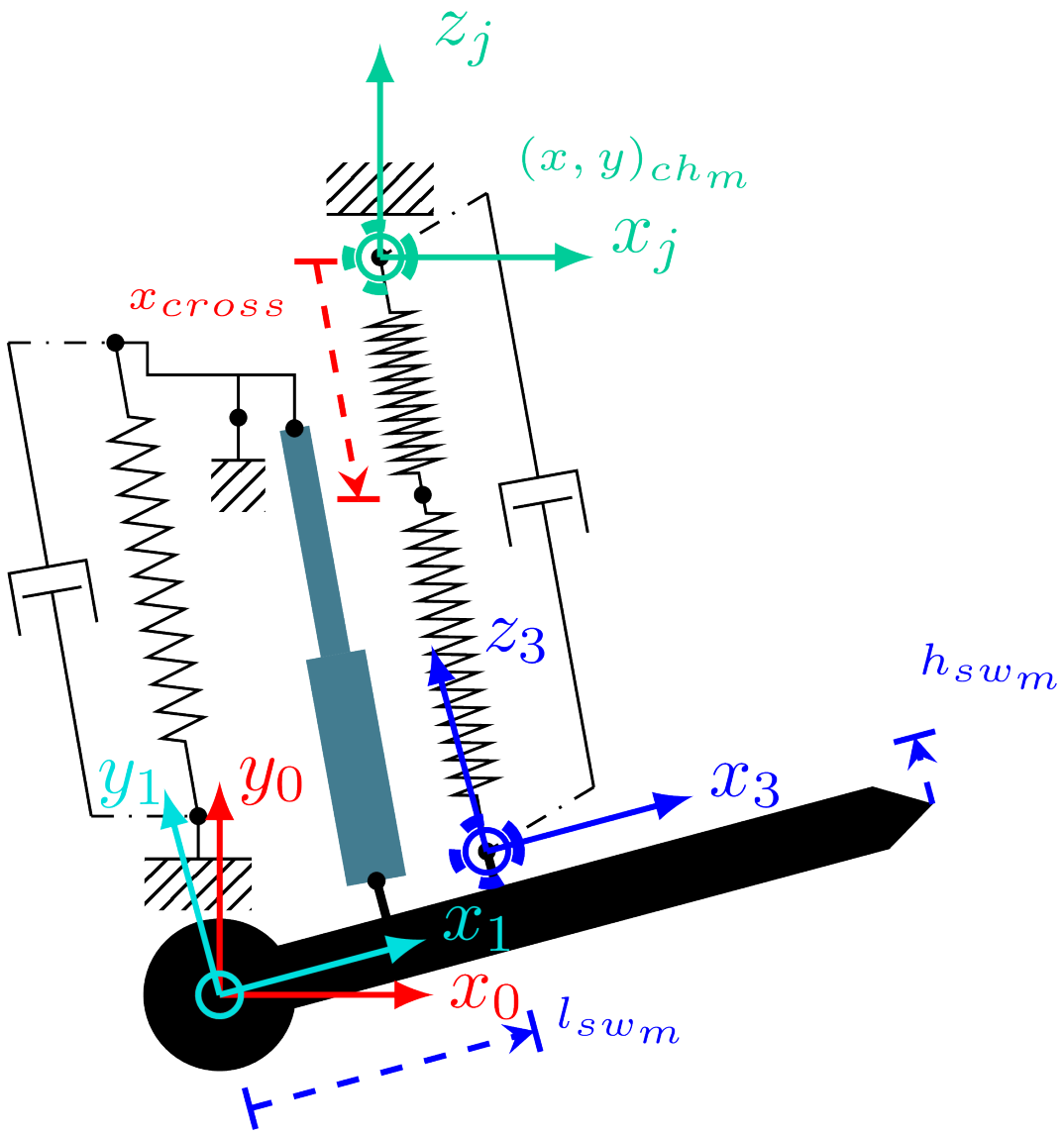

Figure 3.13: Diagram of pertinent frames for the gravity offset spring system.

ment diagram can be found in Figure 3.14

Simplifying repeated terms with the following definitions:

$$A = \sin(\gamma)\cos(\theta) + \sin(\theta)\cos(\gamma)$$

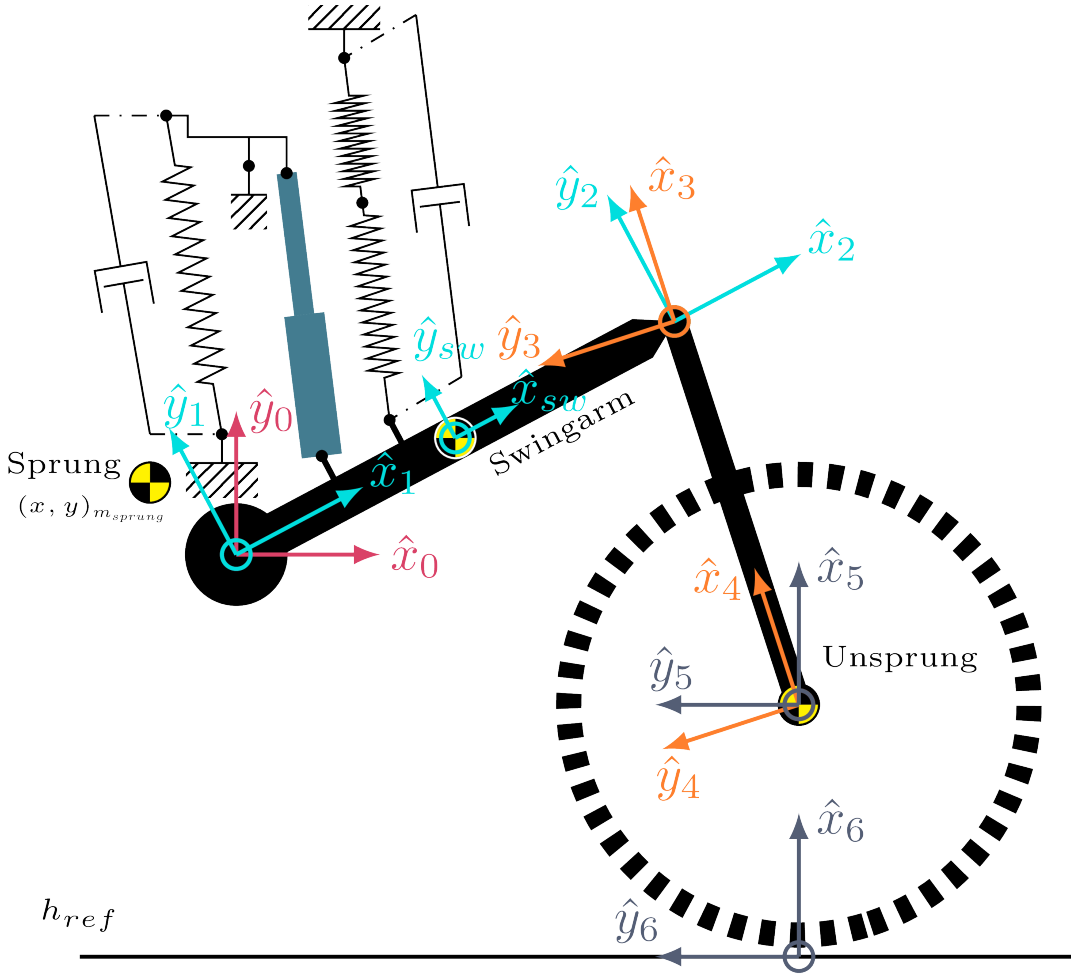

Figure 3.14: Frame assignments for the sprung and unsprung mass

$$B = -\sin(\gamma)\sin(\theta) + \cos(\gamma)\cos(\theta)$$

$$C = \sqrt{l_{\text{ows}}^2 B^2 + l_{\text{ows}}^2 A^2}$$

The final equation for the potential energy of the sprung mass, using the frame assignments shown above, can be expressed as shown in Equation 3.30.

$$PE_{\text{Sprung}} = m_{\text{sprung}} * g * \Bigg(- l_{\text{ows}} A + l_{\text{sw}} \sin(\theta) \\ -r_{\text{wheel}} \left(\frac{l_{\text{ows}} B A}{C} - B \sqrt{-\frac{l_{\text{ows}}^2 B^2}{C^2} + 1} \right) + y_{\text{sprung}} \Bigg) \tag{3.30}$$

3.3.2.3 K.E. Sprung Mass

The kinetic energy of the sprung and unsprung masses can be defined using the same frame assignments.

$$D = l_{\text{ows}}\ l_{\text{sw}} \Big[B\ \cos(\theta) + A\ \sin(\theta) \Big]$$

$$E = \Big(l_{\text{ows}}\, B - l_{\text{sw}}\ \cos(\theta) \Big)^2 + \Big(l_{\text{ows}}\, A - l_{\text{sw}}\ \sin(\theta) \Big)^2$$

$$T_{\text{Sprung}} = \frac{0.125\ m_{\text{sprung}}\ D^2\ E\ \left(\dot{\theta} \right)^2}{C^2\, l_{\text{sw}}^2} \tag{3.31}$$

3.3.2.4 K.E. Unsprung Mass

$$G = B\ \cos(\theta) + A\ \sin(\theta)$$

$$\Lambda = \frac{G^2}{A^2 + B^2}$$

$$T_{Unsprung} = 0.5\, m_{\text{unsprung}} \Big(1 - \Lambda\Big)\, E\, \dot{\theta}^2 \tag{3.32}$$

3.3.2.5 P.E. - Swingarm

$$\alpha = \frac{B^2}{A^2 + B^2}$$

$$W = r_{\text{wheel}} \Big(\frac{l_{\text{ows}}\, B\, A}{C} \; - \; B\, \sqrt{1 - \alpha} \Big)$$

$$V_{\text{sw}} = m_{\text{sw}} \; \Big(- l_{\text{ows}}\; A + l_{\text{sw}} \; \sin(\theta) + \frac{l_{\text{sw}} \; \cos(\theta)}{2} - W \Big) \tag{3.33}$$

3.3.2.6 K.E. - Swingarm

Equation 3.34 shows the final form for the energy related to the inertia of the swingarm, and evolved from earlier equations 3.4 and 3.5. The direct tie between the swingarm and the generalized coordinate makes this a particularly simple calculation without the need for transformation matrices.

$$T_{SW} = \frac{1}{(2)12} m_{sw} \left(\frac{3ID_{sw}^2}{4} + \frac{3OD_{sw}^2}{4} + l_{sw}^2 \right) \dot{\theta}^2 \tag{3.34}$$

3.3.3 Potential Energy - Series Elastic Element

The series elastic element has two distinct conditions, compressed and uncompressed. Equations need to be defined for both sets, the former of which simply relies on the current state of the suspension member deflections, and the latter relying on force balancing conditions to segment the series elastic element force into what is experienced by the suspension system and what is being maintained in the circumferential retention strap.

Figure 3.15 shows the frame assignments for the series elastic actuator system. To fully define the state of the suspension system, more information is required than just the angle of the swingarm θ due to the inclusion of the series elastic element. Any additional information on the state of the series elastic actuator, be it the length of the SEE, the pivot angle ϕ, or the linear actuator length d, will then fully define the system.

The kinematics for the SEA are defined around the pivot location between the SEE and the linear actuator. The assignment logic for these frames is described in Table 3.3 as the purposes may not be as obvious as in Figure 3.14.

Table 3.3: Frame assignment logic for the reference frames as shown in Figure 3.15

Frame	Description
0	Fixed frame at swingarm hub
1	Fixed frame translated from frame 0 to pivot mount by (x_p, y_p)
2	Pivot rotating frame from frame 1 by angle ϕ
3_a	Translated frame by (x_{p2s}, y_{p2s}) (pivot to spring = $p2s$) for SEE top mount
3_b	Translated frame by (x_{p2a}, y_{p2a}) (pivot to actuator = $p2a$) for actuator top mount
s	Translated frame from frame 0 by (x_{lower}, y_{lower}) for SEE bottom mount
rot	Frame rotated by angle θ from frame 0
a	Lower actuator mounting frame from Frame rot by l_{swA} and h_{swa} as shown in Figure 3.15 (swingarm mount actuator = swA)

The VERTEX rover is not presently equipped with measurement devices for any of the three alternate measurements. Integration of a rotational encoder at the pivot point may be physically challenging, but the inclusion of a tape-reel style encoder on the series elastic element or the linear actuator are feasible upgrades for future work.

However, these parameters can be estimated without these upgrades under a quasi-static assumption. The VERTEX suspension is considered to be "adaptive" as opposed to "active" due to its low bandwidth at nearly 60 seconds to complete a full cycle across its range of motion. The suspension is designed to accommodate for slopes and intentionally point the chassis at a desired orientation, but on the scale of large terrain deformation and not to accommodate for rocks on a high speed traverse where the passive spring damping becomes the primary compensation mechanism. If the vehicle is then not traveling at a speed or across a terrain that causes the series-elastic element to deflect then the series elastic system can be assumed to have a pivot angle ϕ of 0 quasi-statically. This becomes helpful in the dynamic test comparison as shown in Section 4.1.3 as the vehicle's chassis orientation is set in a static position and then driven over an obstacle without adjusting the linear actuator length, allowing the starting state of the suspension to be estimated via only the swingarm angle θ. Given the starting length of the linear actuator, d, the following equations allow for the calculation of ϕ. Frame notation follows assignments from Figure 3.15 and uses the pre-superscript as the frame the vector point is transformed from.

$$R_a = -h_{swA}\,\sin(\theta) + l_{swA}\,\cos(\theta) - x_p - x_{p2a}$$

$$R_b = h_{swA}\,\cos(\theta) + l_{swA}\,\sin(\theta) - y_p - y_{p2a}$$

$$R = \Delta l_{SEE} = \sqrt{R_a^2 + R_b^2}$$

$$\delta_d = d \; - \; R(\theta), \quad \text{and} \quad r_{p2a} = \sqrt{x_{p2a}^2 \; + \; y_{p2a}^2}$$

$$\phi = \operatorname{sgn}\big[-\delta_d(\theta)\big] \; \arccos\left(1 \; - \; \frac{\big(\delta_d(\theta)\big)^2}{2\left(r_{p2a}\right)^2}\right) \tag{3.35}$$

$$\dot{\phi} = \frac{d\phi}{d\theta} \; \dot{\theta} \tag{3.36}$$

Performing the aforementioned sensing upgrades to the series elastic system will allow for more complete models to be created and used for onboard compensation and state estimation without the use of the quasi-static assumption. This may be helpful for meeting added ride quality requirements in future research.

If the calculation of ϕ indicates the series elastic element has been compressed, Equation 3.37 captures the energy contribution of the element.

$$L_{\text{eff}} = \sqrt{V_x^2 + V_y^2}$$

$$V_x = x_{\text{lower}} - x_p$$

$$\alpha_2 = \frac{\big|\, d - d_A \big|^2}{2\, x_{\text{p2a}}^2 + 2\, y_{\text{p2a}}^2}$$

$$V_y = x_{\text{p2s}}\big(1-\alpha_2\big) - y_{\text{lower}} + y_p - y_{\text{p2s}}\sqrt{1-\big(1-\alpha_2\big)^2}$$

$$d_A = \sqrt{A_x^2 + A_y^2}$$

$$A_x = h_{\text{swA}}\,\sin(\theta) - l_{\text{swA}}\,\cos(\theta) + x_p + x_{\text{p2a}}$$

$$A_y = h_{\text{swA}}\,\cos(\theta) + l_{\text{swA}}\,\sin(\theta) - y_p - y_{\text{p2a}}$$

$$PE_{SEE} = 0.5\,K\,x_{\text{preload}}^2 + 0.5\,K\,\Big|\,l_{\text{uncomp}} - L_{\text{eff}}\Big|^2 \tag{3.37}$$

If the calculation of ϕ indicates the series elastic element is not compressed, the state of the system either in tension or compression must be determined using Equation 3.22. The equation capturing energy contributed to the system by the damper in the uncompressed state is too long to effectively present in this paper, requiring too many substitutions in the force balancing process.

3.3.4 Non-Conservative Forces - Reaction Moments

The non-conservative forces are the moments about the generalized coordinate θ and use the same set of reference frames as shown in Figures 3.14 and 3.15. These forces are comprised of damping forces from the dual-rate spring damper (Q_{GO}) and a linear damping coefficient (Q_{linear}) corresponding to the swingarm angular rate, as well as the the ground reaction forces as

shown in Figure 3.6 (Q_{SW}, Q_{OWS}).

$$Q_{\text{SW}} = \frac{g\, l_{\text{ows}}\, l_{\text{swingarm}} \left(\frac{m_{\text{sprung}}}{4} + m_{\text{swingarm}} \right) B}{C} \tag{3.38}$$

$$Q_{\text{OWS}} = g\, l_{\text{ows}} \left(\frac{m_{\text{sprung}}}{4} + m_{\text{swingarm}} \right) \sqrt{1 - \alpha} \tag{3.39}$$

$$Q_{\text{react}} = Q_{\text{SW}} + Q_{\text{OWS}} \tag{3.40}$$

3.3.5 Non-Conservative Forces - Damping

Equations for the nonlinear damping forces as shown in the following sections. They have been split into separate forms for the direction dependence using the Heaviside function H(x) to activate as appropriate.

3.3.5.1 Chassis Pivot Damping

As the damping model for the chassis pivot is linear with the swingarm angular velocity, the final integrated equations are very similar to the theoretical equation form from section 3.2.2.1. The final integration includes the differential damping dependent on the velocity direction.

$$D_{\text{p}} = -\, F_{c\text{p}} - \sigma_{\text{p}}\, \dot{\theta} - \left[-\, F_{c\text{p}} + F_{s\text{p}} \right] e^{-\left(\frac{\dot{\theta}}{v_{s\text{p}}} \right)^{\delta_{\text{p}}}}$$

$$D_{\text{n}} = F_{c\text{n}} - \sigma_{\text{n}}\, \dot{\theta} + \left[-\, F_{c\text{n}} + F_{s\text{n}} \right] e^{-\left(\frac{|\dot{\theta}|}{v_{s\text{n}}} \right)^{\delta_{\text{n}}}}$$

$$Q_{\text{ChassisDamping}} = D_{\text{neg}}\, H(-\dot{\theta}) \;+\; D_{\text{pos}}\, H(\dot{\theta}) \tag{3.41}$$

3.3.5.2 Gravity Offset Damping

The damping in the gravity offset damper is comprised of the follow equations with $h_{\text{sw m}}$ representing the mounting height above the swingarm of the GO damper, $l_{\text{sw m}}$ is the length down the swingarm that the damper is mounted, and $(x_{\text{ch m}}, y_{\text{ch m}})$ are the (x,y) coordinates from the swingarm pivot to the fixed upper mounting point of the damper.

$$\Xi = h_{\text{sw m}}\ \sin(\theta) - l_{\text{sw m}}\ \cos(\theta) + x_{\text{ch m}}$$

$$\Upsilon = -\,h_{\text{sw m}}\ \cos(\theta) - l_{\text{sw m}}\ \sin(\theta) + y_{\text{ch m}}$$

$$\Delta_m = \sqrt{h_{\text{sw m}}^2 + l_{\text{sw m}}^2}$$

$$F_{\text{neg}} = c_{\text{GO neg}}\ \left|\Delta_m\, \dot{\theta}\right|^{n_{\text{GO neg}}+1}\ \left[H(-\dot{\theta})\right]$$

$$F_{\text{pos}} = c_{\text{GO pos}}\ \left|\Delta_m\, \dot{\theta}\right|^{n_{\text{GO pos}}+1}\ \left[H(\dot{\theta})\right]$$

$$\zeta = -\,\Xi\ \sin(\theta) -\ \Upsilon\ \cos(\theta)$$

$$Q_{\text{GO Damping}} = \frac{l_{\text{sw m}}\ \zeta\ \left[F_{\text{neg}} - F_{\text{pos}}\right]}{\sqrt{\Xi^2 + \Upsilon^2}} \tag{3.42}$$

3.3.5.3 SEE Damping

The set of applied equations for the damping within the series elastic element follow a very similar procedure as demonstrated for the GO damping but are dependent on the time derivative of the pivot angle ϕ. Evaluating $\frac{d\phi}{d\theta}\ \dot{\theta}$ forms too long of an equation to present concisely in this publication.

$$v_{pivot+} = H\left(\dot{\phi}\right)\ \left|\dot{\phi}\right|^{\,1+n_{\text{pos}}},$$

$$v_{pivot-} = H\left(-\dot{\phi}\right)\ \left|\dot{\phi}\right|^{\,1+n_{\text{pos}}},$$

$$Q_{damp\,SEE} = l_{\text{mount}}(-c_{pos}\ v_{pivot+} + c_{neg}\ v_{pivot-})$$

3.3.6 Bushing Contributions

As the contributions from the suspension bushings are assumed to be linear respective to the pivot, and are dependent on the amount of deflection beyond the quasi-static limit, the applied version of for each equation is relatively close to the original theoretical formulation given ϕ.

3.3.6.1 Potential Energy

For the lower limit of the pivot, $\phi < 0$, rotating clockwise:

$$V_{\text{SEA Lower}} = \frac{1}{2}\, k_{\text{SEA bushing}}\, (l_{swA})^2\, \left[\phi\, H\big(-\phi\big)\right]^2$$

For the upper limit of the pivot, $\phi > 45°$, rotating counter-clockwise:

$$V_{\text{SEA Upper}} = \frac{1}{2}\, k_{\text{SEA bushing}}\, (l_{swA})^2\, \left[\left(\phi - \frac{\pi}{4}\right) H\left(\phi - \frac{\pi}{4}\right)\right]^2$$

For the swingarm contacting the upper rubber bushing hardstop at the top of the range of motion θ >45°:

$$V_{\text{Hardstop}} = \frac{1}{2}\, k_{\text{bushing upper}}\, (\frac{1}{2}\, l_{swA})^2\, \left[\left(\theta - \frac{\pi}{4}\right) H\left(\theta - \frac{\pi}{4}\right)\right]^2$$

3.3.6.2 Damping

As the set of rubber bushings is assumed to have differential damping between its directions, the effective damping rate can be found as follows:

$$c_{\text{bush,eff}} = -\, 0.5 \left(c_{\text{bush,neg}} + c_{\text{bush,pos}}\right) - \left[-0.5\, c_{\text{bush,neg}} + 0.5\, c_{\text{bush,pos}}\right] \text{sign}\big(\dot{\phi}\big)$$

The generalized force then from the bushings can be expressed as follows:

$$Q_{\text{LowerBushing}} = l_{swA} \left[c_{\text{bush,eff}}\, \dot{\phi}\right]\, H\big(-\phi\big)$$

$$Q_{\text{UpperBushing}} = l_{swA}\,\left[c_{\text{bush,eff}}\;\dot{\phi}\right]\;H\left(\phi - \tfrac{\pi}{4}\right)$$

$$c_{\text{eff hardstop}} = \;-\;0.5\left(c_{\text{upper neg}} + c_{\text{upper pos}}\right) - \left[-0.5\,c_{\text{upper neg}} + 0.5\,c_{\text{upper pos}}\right]\text{sign}\left(\dot{\theta}\right)$$

$$Q_{\text{HardStop}} = c_{\text{eff hardstop}}\;\dot{\theta}(\frac{1}{2}\,l_{swA})\;H\left(\theta - \tfrac{\pi}{4}\right)$$

With the piecewise set of Lagrangians created, the validation and system characterization can begin.

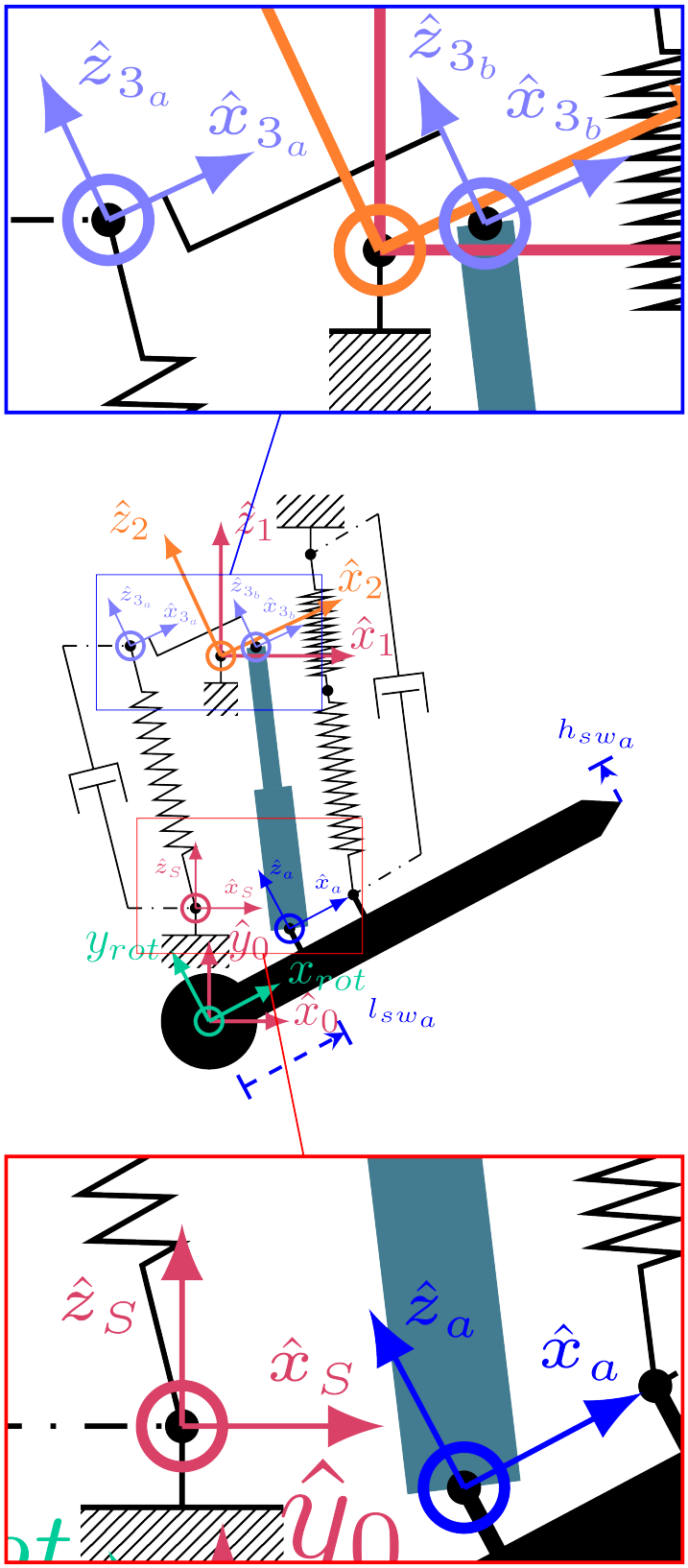

Figure 3.15: Frame assignments for the series elastic actuator system

Chapter 4: Validation and System Improvement

The content in chapters 3 and 4 has been written as a stand-alone paper to be submitted shortly after the culmination of this thesis.

Contributions In This Chapter This chapter presents a new machine learning framework focused on system identification for the as-built suspension design. The approach presented is originally used to identify differences between the as-modeled forces and the as-measured forces on the vehicle to identify a shortfall in the original set of assumptions, but is later used to optimize the force profile within the series elastic element. Additionally, this section works to validate the Lagrangian model as developed in Chapter 3 by comparing it against a set of collected impulse-response data.

4.1 Model Validation

Two main steps were used to validate the modeling approach presented in Section 3.2. The first is a quasi-static validation to ensure the predicted forces within the suspension aligned with the model, and second is a dynamic comparison between the two with data collected with a moving rover. The two-step validation process was designed to help in the debugging of the model and provide a checkpoint showing the generalized approach used for the subsequent numerical propagation closely matches the real-world system.

4.1.1 Quasi-Static Experiment

One advantage in using the generalized coordinate of θ is in allowing for a relatively simple translation from a system state into the forces felt in any given member. As discussed surrounding equation 3.22, the process to arrive at the load felt within the series-elastic element using the generalized forces is fairly straight forward and when combined with the quasi-static assumption provides an avenue for the intermediate static validation step.

By adjusting the length of the linear actuator in the model, a range of combinations of (d, F_{SEE}) can be predicted. A load-cell was calibrated and integrated to the suspension where the series-elastic element was, thus removing any passive spring damping capability from that suspension member but allowing for onboard recording of force within that member.

The series elastic element was replaced with a load cell on the vehicle's right side as shown in Figure 4.1. The rover then was commanded to raise and lower across nearly 5 full cycles, with all linear actuators commanded to move at the same rate. Figure 4.2 shows the result between the predicted curve and the actual curve after the first trial.

Figure 4.1: Load cell integration into the front-right suspension system on VERTEX, replacing the series elastic element.

The results shown in Figure 4.2 show three unexpected characteristics. First is the presence of a significant hysteresis in the measured swingarm force data with a range between 150 to 220 lbf (outside the transition areas between positive and negative velocity). It is not immediately clear if the blue line, red line, or some average between the two should be used as the comparison point, and neither is the root cause of the hysteresis. To evaluate the line the model should be compared with the zero-crossing point of the force was used. This point being the location of

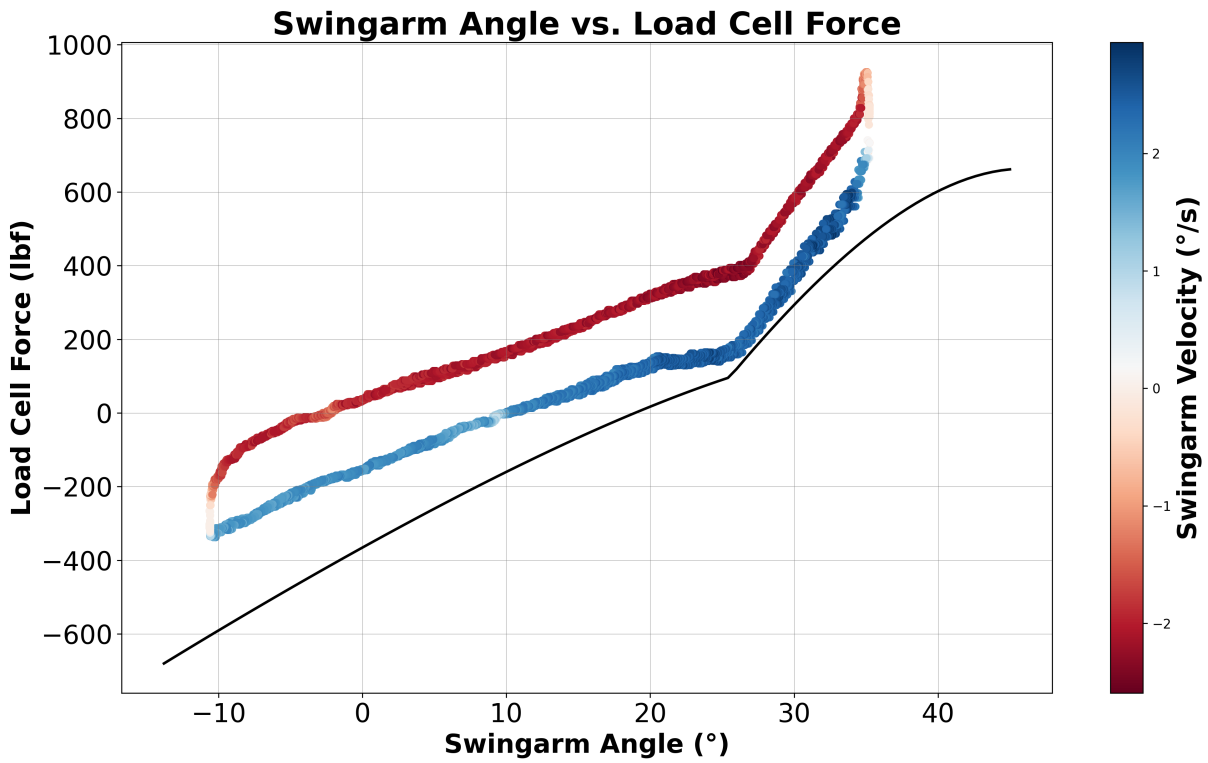

Figure 4.2: Initial diagram comparing load cell sensed force (colored points) with predicted force in the series elastic element (black curve). Colorization of the points shows a force hysteresis is present and is dependent on swingarm velocity direction.

zero force on the series elastic element, also means the linear actuator becomes a zero-force member and the swingarms rely purely on the dual-rate spring dampers to maintain position. The suspension was adjusted until the series elastic elements and the load cell could be removed, and the suspension could fully rest on the series springs as shown in Figure 4.3, and the swingarm angle was measured to be very close to the approximately 9.23° load cell crossing point. The blue line is then used for the comparison point with the predicted force curve in the upcoming analyses. It is still undetermined what causes the significant force difference, but it is believed that frictional forces play a major role.

The next two characteristics required a deeper analysis. The second characteristic is the y-axis offset between the predicted curve and the actual curve. As the vehicle weight was measured

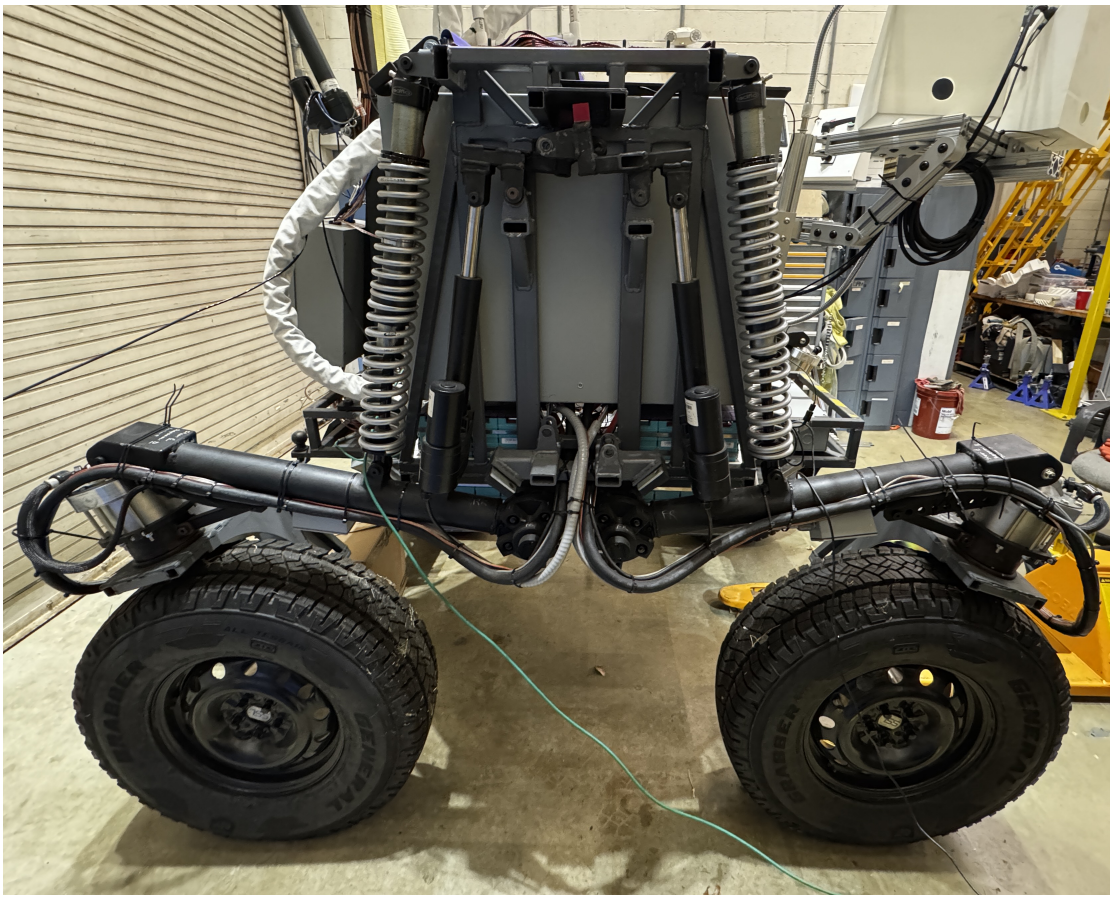

Figure 4.3: VERTEX's right side with no series elastic elements installed on the front and rear suspension while investigating the no-load condition.

to be 2,600 lbf with a crane scale (± 2 lbf), this offset was unexpected. The vehicle parameter that has the greatest effect on the position of the y axis is the sprung weight, and the predicted sprung mass was 1,400 lbf by subtracting out the 250 lbf per wheel of unsprung mass and 50 lbf per swingarm. It was suspected that these estimations may not have been perfect and was causing the offset, but further characterization would be needed.

The last characteristic is the difference in slopes above and below the sharp crossover point. The sharp point is the transition between the dual-rate damper acting with the series spring rate and just the lower spring rate. Above this point deflections of the damper result in compression of the 400 lb/in spring, and below this the effective spring rate is $\approx$ 133 lb/in. The curve appeared

to transition at the correct point, indicating that the crossover calculation process as shown in equations 3.20 and 3.21 is correct, however determining the root cause of the slope was not straightforward. A sensitivity analysis to potentially obvious parameters such as spring rates, sprung mass, preload, and crossover distances was performed, and no single parameter was able to adjust the slopes as desired.

As a note, the fact that the swingarm did not achieve its full upward range of possible motion before hitting its hard rubber bump stop was an expected characteristic. During a field trial the suspension crossover point was adjusted to provide a stiffer platform, and as a result the linear actuator experiences its operating limitation of $\approx$ 2,000 lbf at $35.90°$. This characteristic was expected, and future optimization of the suspension settings should be performed to allow a greater range of motion while remaining statically stable.

4.1.2 ML-Based Parameter Identification

Due to these emerged discrepancies between the theoretical and measured series elastic element force curves, an investigation was undertaken to identify possible causes. In an effort to systematically work through possible causes, Python's `scipy.optimize` library was applied in hopes of identifying which suspension parameters exerted the strongest influence on aligning the model with observed data. This initial effort was motivated by the idea that such alignment (or misalignment) might reveal model inadequacies, questionable assumptions, or inaccuracies in the as-built suspension itself.

As listed in Appendix A.1, the VERTEX system is defined by a large set of numerical parameters. In the context of quasi-static calculations, many of these (e.g., chassis dimensions,

damping coefficients for dynamic analysis, spring lengths, etc.) can be temporarily disregarded, reducing the problem size to 29 parameters. Although 29 variables is certainly more manageable than the full set, it remains a sizable optimization task. Moreover, the computational cost of performing this search with our existing model and packages proved substantial, prompting the exploration of alternative methods.

To overcome these limitations, optimizers originally developed for ML and AI applications were employed. Such optimizers are well-suited to large parameter spaces and complex functions, and their sophistication and flexibility offer a promising route to identify latent parameter inconsistencies or unmodeled physical effects in the system.

4.1.2.1 Model Structure

Various network structures, optimizers, and loss functions were explored to inform the design of the final model using Python's `PyTorch` library. PyTorch is an open-source framework for building machine learning codes and applications. The initial concept relied on a three-layer model as shown in Figure 4.4, which maintained activations within the range [0, 1] to promote numerical stability and efficient training. The network ingests an `n`-dimensional vector representing the nominal suspension parameters and outputs `n` corresponding multipliers. These multipliers are constrained to vary the nominal parameters by at most a predefined percentage, ensuring that adjustments remain physically plausible and within acceptable deviation bounds.

This model was ultimately hard to train to produce informative results even across a wide variety of loss function configurations. Multiple network depths were evaluated, but in testing produced minimal improvement beyond a three-layer design. In practice, a simpler direct param-

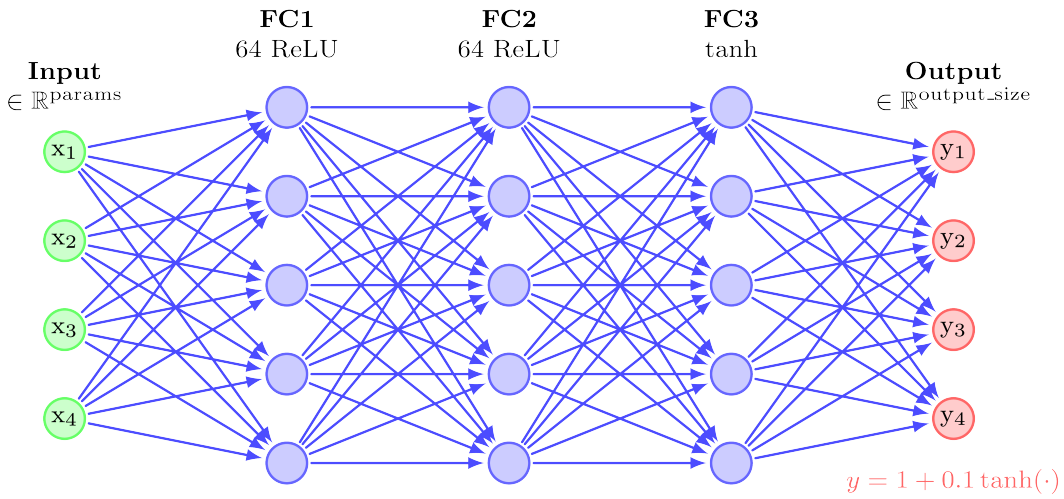

Figure 4.4: Initial NN model attempt relying on forming multipliers for each numerical suspension parameter and bounding within a set multiplier boundary, shown as 0.1 in this example.

eter method was found to be significantly more robust.

The same suspension definition classes as shown in Appendix A.1's Tables 1, 2, and 3 were converted to tensor compatible submodules. All three submodules extend PyTorch's nn.Module, storing their respective parameters (e.g., masses, lengths, damping coefficients) as learnable nn.Parameters. The overarching model inherits the parameters from nn.Module, combining these submodules into a single trainable system. Consequently, the model returns all parameters from the rover, prismatic spring-damper, and gravity-offset springs as one handy function.

4.1.2.2 Custom Loss Function

To improve training stability and focus on the unique physical characteristics of the suspension system, a specialized loss function was developed. The function combines traditional mean-squared-error (MSE) terms with domain-specific penalties that encourage physically plausible solutions.

The angle $\theta \in \mathbb{R}^N$ is a vector of N discrete swingarm angles and $\mathbf{F}_{\text{pred}}, \mathbf{F}_{\text{true}} \in \mathbb{R}^N$ are the predicted and ground-truth forces, respectively.

1) Mean-Squared Error (MSE):

$$\mathcal{L}_{\text{MSE}} = \frac{1}{N} \sum_{i=1}^{N} \left(F_{\text{pred},i} - F_{\text{true},i}\right)^2$$

MSE is included as a wide-reaching penalty term looking to help focus the training on a macro- scale in comparison to the focused later terms.

2) Knee Detection & Penalties: To identify the "knee" (i.e., the transition between the dual-rate and lower-rate spring regimes) in the predicted force profile, a function computes the curvature $\kappa(\theta)$ by estimating the first- and second-order derivatives with respect to θ. In continuous form, the curvature of $F(\theta)$ can be written as

$$\kappa(\theta) = \frac{\left|\frac{d^2F}{d\theta^2}\right|}{\left(1 + \left(\frac{dF}{d\theta}\right)^2\right)^{3/2}}$$

We locate $\theta_{\text{knee}}^{\text{pred}}$ as the angle at which $\kappa(\theta)$ peaks. The predicted force curve is very smooth and this easily finds the point, but the crossover point is manually set from the measured data due to noise. A sigmoid-based validity score is ultimately clamped to produce either 0 or 1, penalizing invalid/numerous knees, or unrealistically sharp transitions:

$$\mathcal{L}_{\text{knee}} = (1 - \mathcal{V}) \sqrt{(\Delta\theta\ \lambda_\theta)^2 + (\Delta F\ \lambda_F)^2}$$

$$\text{where} \begin{cases} \Delta\theta = \theta_{\text{knee}}^{\text{true}} - \theta_{\text{knee}}^{\text{pred}}, \\ \\ \Delta F = F_{\text{true}}\big(\theta_{\text{knee}}^{\text{true}}\big) \; - \; F_{\text{pred}}\big(\theta_{\text{knee}}^{\text{pred}}\big). \end{cases}$$

As the scale between the x and y axes is significantly different, individual gains are set to scale the $Delta\theta$ and $DeltaF$ values in the form of λ_θ and λ_F. As of this publication, the approach with the greatest success has been with scaling the $\Delta\theta$ value up to ΔF scale, as opposed to the opposite. If the knee is deemed "valid" ($\mathcal{V} = 0$), then $\mathcal{L}_{\text{knee}}$ is computed. Otherwise, the penalty is effectively set to a very large gain $\mathcal{L}_{\text{invalid}}$:

$$\mathcal{L}_{\text{invalid}} = \mathcal{V} \cdot \lambda_{\text{invalid\_knee}}$$

3) Slope Regularization via Polynomial Fits: A polynomial of degree d, usually 2, is fit to each segment of the force curve separately below and above the predicted knee on both the measured and predicted data:

$$p_d(\theta) = \sum_{k=0}^{d} a_k \, \theta^{d-k}$$

A set of functions perform least-squares fitting and evaluation. We compare the polynomial coefficients of the true and predicted curves on both sides of the knee as both curves utlize the same degree of polynomial fit:

$$\mathcal{L}_{\text{slope}} = \sum_i \lambda_{\text{slope}} \left\| \mathbf{a}_{\text{i}}^{\text{pred}} - \mathbf{a}_{\text{i}}^{\text{true}} \right\| \; i \in \{above, below\}$$

4) Threshold Penalty: Physical actuators or structural limits may cap allowable force. F_{th} is set

as a predefined threshold (e.g., 1000 lbf) that the elastic element should never be subjected to. Excess predicted forces (in either tension or compression) $|F_{\text{pred}}| > F_{\text{th}}$ incur a penalty:

$$\mathcal{L}_{\text{threshold}} = \lambda_{\text{flat}} \sum_{i=1}^{N} \max\Big(0,\ |F_{\text{pred},i}| - F_{\text{th}}\Big)$$

5) Total Loss: The overall objective combines these terms into:

$$\mathcal{L}_{\text{total}} = \mathcal{L}_{\text{MSE}} + \mathcal{L}_{\text{knee}} + \mathcal{L}_{\text{invalid}} + \mathcal{L}_{\text{slope}} + \mathcal{L}_{\text{threshold}}$$

This structure preserves the usual MSE minimization while explicitly guiding the knee location, the slope continuity, and disallowing physically unrealistic forces.

Algorithm 1 High-Level Custom Loss Computation

Require: $\theta,\ \mathbf{F}_{\text{pred}},\ \mathbf{F}_{\text{true}},\ \theta^{\text{true}}_{\text{knee}},$
$\lambda_\theta,\ \lambda_F,\ \lambda_{\text{invalid\_knee}},\ \lambda_{slope},\ \lambda_{threshold}$

MSE $\leftarrow \frac{1}{N}\sum_i (F_{\text{pred},i} - F_{\text{true},i})^2$
knee_idx, $\mathcal{V} \leftarrow$ `find_predicted_knee`$(\theta, \mathbf{F}_{\text{pred}})$
$\theta^{\text{pred}}_{\text{knee}} \leftarrow \theta$[knee_idx]
$\Delta\theta \leftarrow \left|\theta^{\text{true}}_{\text{knee}} - \theta^{\text{pred}}_{\text{knee}}\right|$
$\Delta F \leftarrow \left|\, F_{\text{true}}(\theta^{\text{true}}_{\text{knee}}) - F_{\text{pred}}(\theta^{\text{pred}}_{\text{knee}})\right|$
`knee_penalty` $\leftarrow (1-\mathcal{V})\sqrt{(\Delta\theta\ \lambda_\theta)^2 + (\Delta F\ \lambda_F)^2}$
invalid_knee_penalty $\leftarrow \mathcal{V} \times \lambda_{\text{invalid\_knee}}$
`slope_loss` $\leftarrow$ `Poly_fit_loss`$(\theta, \mathbf{F}_{\text{pred}}, \mathbf{F}_{\text{true}}, \theta^{\text{true}}_{\text{knee}})$
threshold_penalty $\leftarrow \lambda_{\text{flat}} \sum |\ \max\{\,|F_{\text{pred}}| - \text{th}, 0\}\,|$
$\mathcal{L}_{\text{total}} \leftarrow$ MSE + knee_penalty + invalid_knee_penalty + slope_loss + threshold_penalty
return $\mathcal{L}_{\text{total}}$

After computing $\mathcal{L}_{\text{total}}$, PyTorch's automatic differentiation updates the suspension parameters in *SuspensionModel* during backpropagation. This ensures that physically meaningful properties (e.g., mass, spring constants) shift to reduce the prediction error while maintaining focus on the valued curve comparisons. Clamping limits are set after the back propagation and optimizer

advancement steps to ensure respectable value limits are maintained. Often these limits are set to a blanket percentage, but some specific values like the gravity fraction are clamped to not allow change.

Finally, the epoch loop uses the Adam optimizer with an initial learning rate of 0.1. A ReduceLROnPlateau scheduler monitors the loss and, if the loss does not decrease for 5 consecutive epochs, reduces the learning rate by a factor of 0.5 to fine-tune convergence.

4.1.2.3 Performance and Results

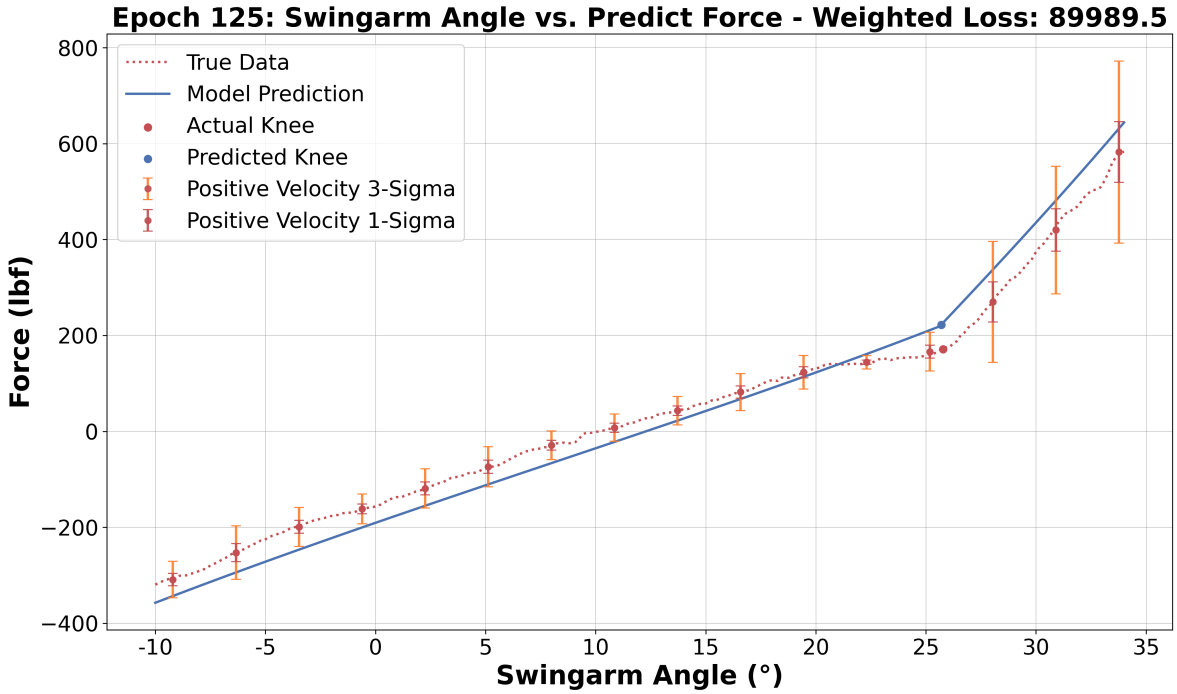

Figure 4.5: Final curve-matching result from using the ML approach to identify vehicle parameters

Although finding sets of gains and optimizer settings was no simple task, informative results were ultimately found. The final result as shown in Figure 4.5 fits the predicted curve almost entirely within 3σ, and in some places to 1σ. The area with the largest deviation is a segment just

before crossover where the curve below the knee has a sharp bend at approximately 22°, as shown in the focused plot in Figure 4.6. The source of the bend has not yet been identified as of the time of publication, but may have a connection to the peaking behavior of sine losses. Interestingly, this area has a force profile similar to that of backlash being taken up in the system. While this would make sense near the swingarm's 0-force point of $\approx 9.23°$, the bend point is much higher in the range of motion and the series-elastic actuator is under significant tension in this regime.

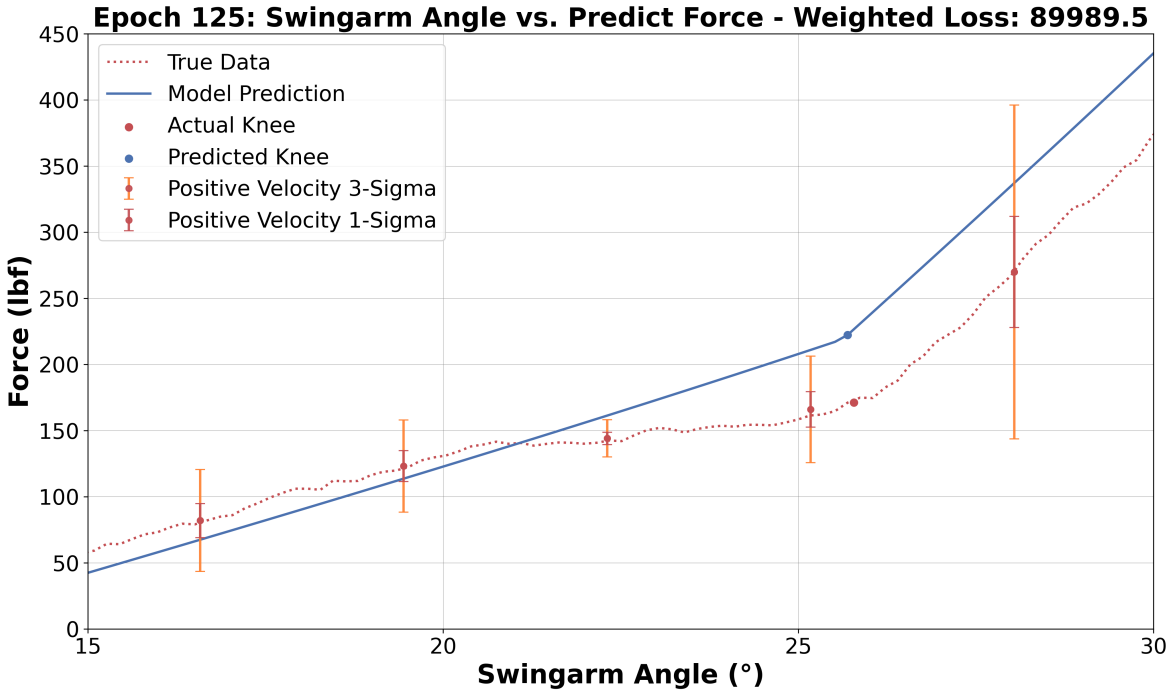

Figure 4.6: Magnified section of Figure 4.5 focusing on the transition region as the system nears crossover

As for practical implications in evaluating whether the predicted curve has adequately fit the true data, two notable points should be considered. First, the bend seems to cause the curve fit of the predicted line below the knee to compromise in slope between the segments before and after this bend.

Secondly, the weighted loss functions used in the final selection closely align the location

of the bend and the departure point of the predicted curve, and prioritized aligning the crossover point at the same swingarm angle. This causes the force at crossover to be higher in the predicted values than the measured points, and subsequently causes a linear offset in the positive direction for the points above the knee. This is why one reason comparing the curve fits of the lines was included in the loss function, as without the odd lessened force bend these curves would likely match very closely. Lastly, the curve fits at nearly all points within 1σ standard deviation.

Comparison of post-optimization values shows that many vehicle parameters were very close to the initial conditions. It should be noted before reviewing that no penalty was applied to the network for deviating from the original values, intended to allow essentially free choice. Examples of values remaining close to their original values include the sprung mass (1400 $\rightarrow$ 1397.79 lbf), swingarm mass (50 $\rightarrow$ 47.78 lbf), and GO spring rates ([200, 400] $\rightarrow$ [201.76, 401.89] lb/in) indicating parameters regarding these values are likely modeled well. However, not all values remained this close. Specifically the two values that changed the most include the swingarm length (34.5 $\rightarrow$ 32.09 in) and the over-wheel steering length (28 $\rightarrow$ 25.98 in), indicating an issue in the model in these areas.

Figure 4.7 shows the difference between the old swingarm tip position, and approximately where the new pivot position is as indicated by the network. The swingarm length offset is the measure between the swingarm pivot and the tip point where the top of the steering actuator bolts into the assembly. The over-wheel steering length measures from the wheel center to the same bolt fixturing point. The structure that was overlooked in the modeling process was the caster adjustment system and is the supplemental strengthening bar with adjustable hole points and can be seen in Figure 4.7. This structure stiffens the assembly and locks the angle of the steering actuator relative to the swingarm to any of the set of drilled points. The model neglected

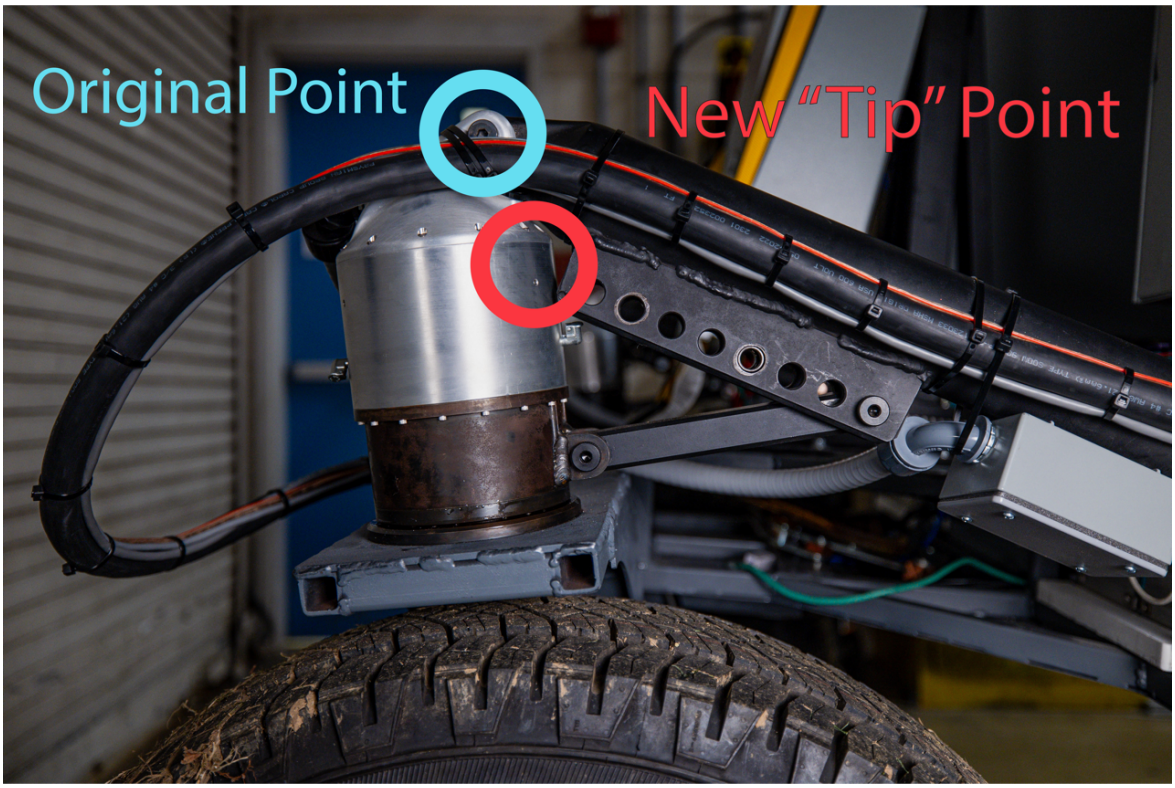

Figure 4.7: Position of new equivalent swingarm tip position as indicted by the minimum loss result, overlaid to approximate scale onto as-built swingarm photo

to include that this structure is responsible for restricting the Q_{OWS} moment, and effectively translates the point of moment application more inward.

4.1.3 Dynamic Validation

After the suspension characteristics were more closely nailed down the load-cell was removed from the suspension system so dynamic trials looking at the suspensions response to obstacles could progress. VERTEX was driven transversely across a relatively sharp obstacle in the road in an attempt to create an impulse response that the code could be trained and validated against (see 4.8).

A series of runs were performed at varying vehicle chassis heights in an attempt to collect a

variety of data to test the model across multiple regimes. The vehicle was also driven at a variety of speeds across the obstacle with the goal of testing a range of impulse magnitudes to subject the vehicle to. Unfortunately, no closed-loop control exists in the traction control system on the vehicle as of publication, so speed was not recorded for each impact.

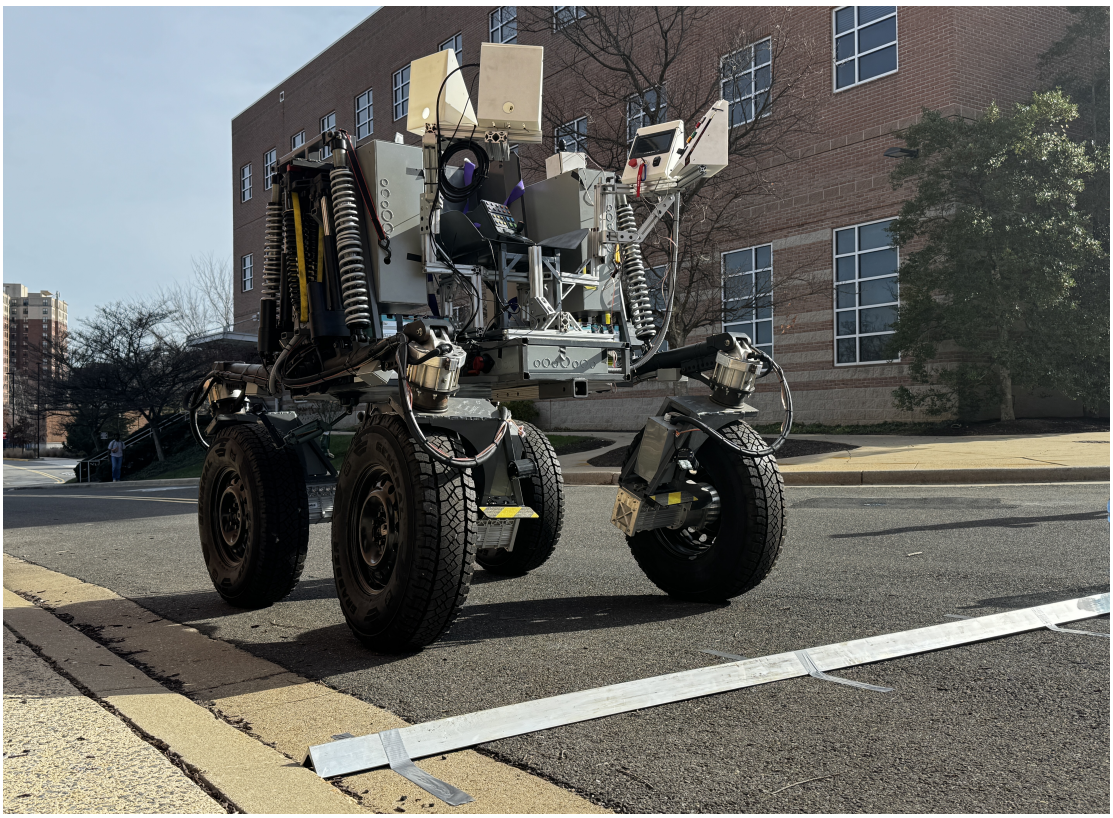

Figure 4.8: Experimental setup for generating an approximate impulse-response scenario under driving conditions. VERTEX as pictured is in an abnormally high driving position.

4.1.3.1 Collected Dynamic Data

The vehicle's on-board control system was used to log system data at a rate of 100 Hz. The relevant data for the comparison with the dynamic model pulled from the data logger is focused around the absolute encoder mounted to the swingarm pivot as shown in Figure 4.9 recording with 13-bits of precision.

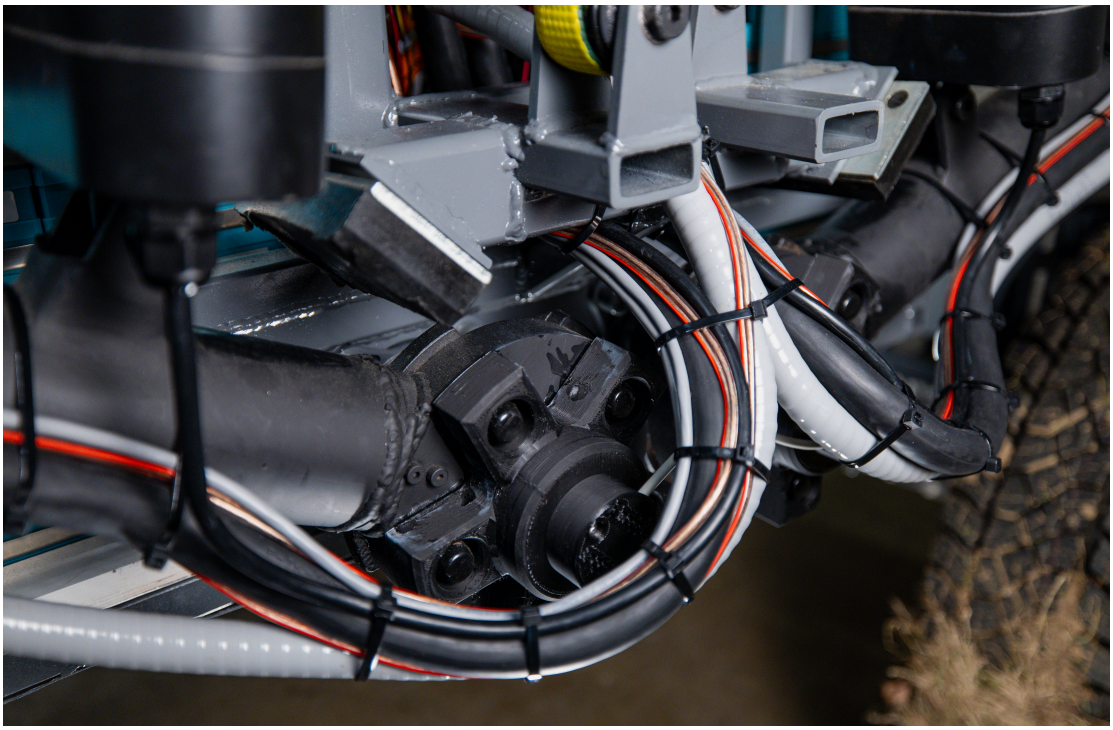

Figure 4.9: Encoder mounting on swingarm pivot

Subsections of the data pertaining to each run were partitioned, with all raw data appearing similarly to as shown in Figure 4.10. Unexpected at first, after working through a set of filtering techniques it was found that either ROS or the onboard carputer were adding erroneous points at a near constant rate of approximately 0.11 seconds. This effect plagued all of the swingarm position and velocity data, consistently placing outlier points at locations near the nominal data points and trending in the same direction as the core data.

The sorting method checked each point's neighbors (except for beginning and end point), and removed an outlier point if it was more than a factor of 3 away from the median. 3 was found experimentally and cleaned the data up nicely without removing the expected datapoints, and resulted in the filtered data as shown in Figure 4.11.

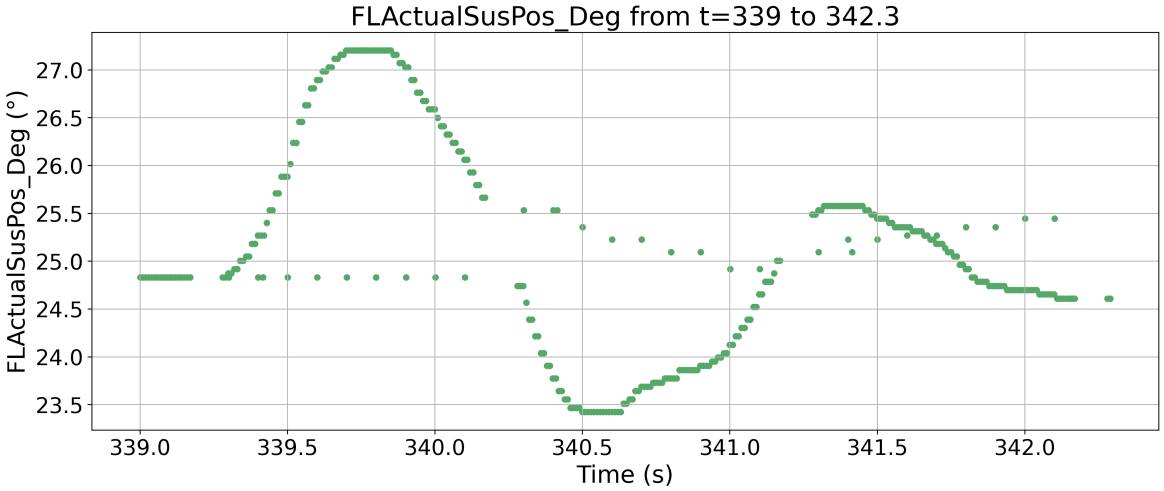

Figure 4.10: FR swingarm angle data pre-filtering, used for tuning model damping values.

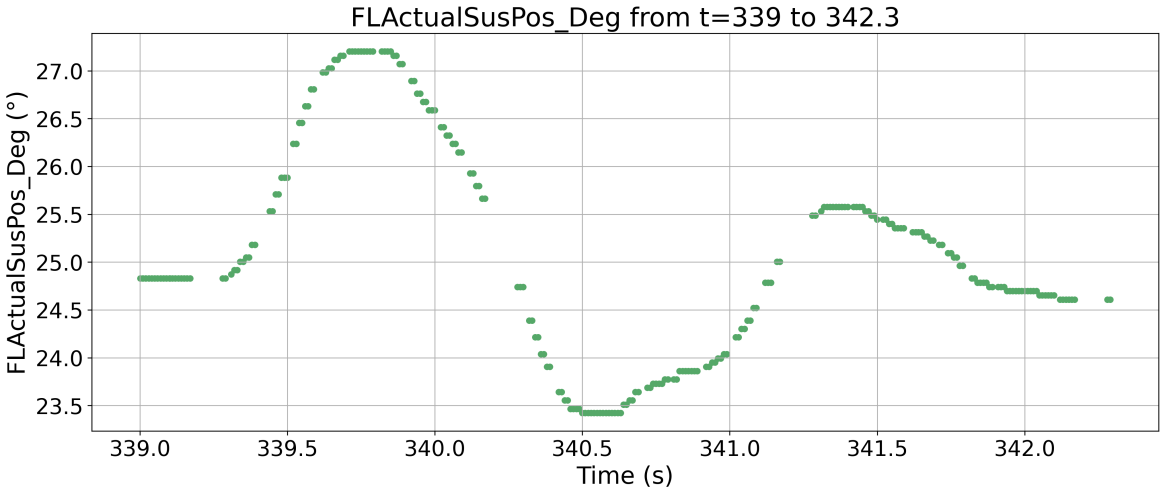

Figure 4.11: Dataset from Figure 4.10 after outlier filtering

4.1.3.2 Comparison with the Lagrangian Model

In the original creation of the Lagrangian, as shown in section 3.2, it was assumed that the damping properties for each component would be similar in the respective positive and negative directions per-component. The force hysteresis as shown in Figure 4.2 shows a significant force difference dependent on swingarm velocity, and after this discovery the model was updated to have a differential set of damping values for each source, dependent on the velocity direction.

With these two updates, 22 damping coefficients and 2 bushing rates (upper hard stop / SEA) are unknowns and need to be identified from recorded datasets. The dataset shown in Figure 4.11 was used to identify the parameters using a variety of optimization techniques. The comprehensive set of parameters can be found in tables 1 - 3.

The search space for the optimization was very wide and appropriate parameter bounds were difficult to set. The strategy employed to try and identify damping parameters within the as-built model was to leverage parallel process computing and step-wise expand a narrowed search space as results required greater headroom. Python's Ray package served as the overarching optimization manager, employing either the Non-dominated Sorting Genetic Algorithm (NGSA-II) or Covariance matrix adaptation evolution strategy (CMA-ES) dependent on search space size. Wider spaces were more quickly sorted by the genetic algorithm, and once parameter sets were settled within a smaller set of bounds and the improvements of the genetic algorithm settled, the CMA-ES solver was employed to find a better solution in a more optimally-guaranteed way.

In the set of optimization attempts performed, the search spaces were initially set in bounds between [0, 1000] for damping coefficients and bushing rates, and the nonlinear coefficients between (1, 1]. Ultimately, after a series of runs with both optimizers, the search space was expanded for all coefficients to [0, 5000] and the nonlinear coefficients were brought in to lower bounds between $\pm$ 0.9. Figure 4.12 shows the best-fit achieved.

The final fit of the plot is reflective of the final configuration of the loss function used during the optimization process. The evaluation criteria evolved from originally a set of curve fits and metrics regarding matching the peaks and slopes to a more controls-focused approach. Characteristics including the rise time, displacement at the rise time criteria, the dominant frequency, bandwidth, settling time, and velocity were all weighted and used to evaluate how closely

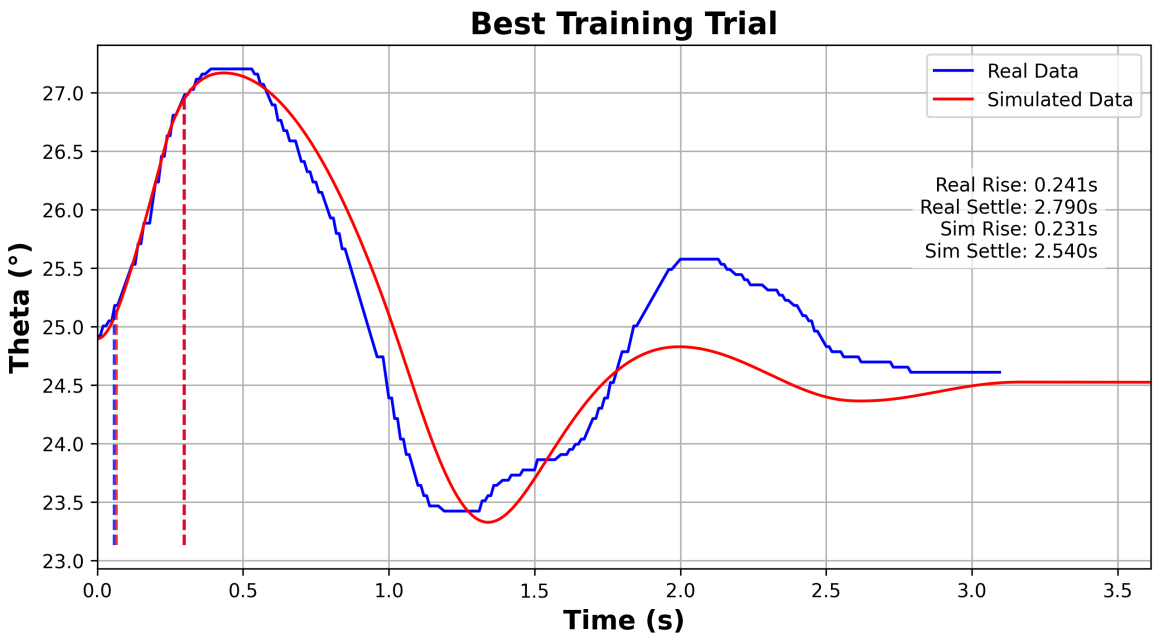

Figure 4.12: Best fit for the training set of data found using the Ray-based optimization scheme in Python. The blue line shows filtered encoder data recorded onboard the BioBot rover, whereas the red line showcases the optimizer's best attempt at fitting the nonlinear dynamics to the real data by varying damping characteristics and the initially-applied step input.

matched each propagated run was to the training data.

In the course of training, when starting from a large dataset it often took between 15,000 and 20,000 iterations before convergence on a best fit value. Thanks to the high-performance computing (HPC) clusters available at the University of Maryland completing these optimization runs takes on the order of days, not weeks to complete. The research presented in this paper would have taken orders of magnitude longer in compute time without the University of Maryland supercomputing resources (`http://hpcc.umd.edu`) made available for conducting the research.

To generate the same effect as the pseudo-impulse response experienced in the experimental data, two approaches were taken. The first approach looked to impart an instantaneous velocity on the swingarm, adding a $\dot{\theta}_{init}$ value to the initial condition. This resulted in graphs whose rise

characteristics were similar to that shown in Figure 4.13.

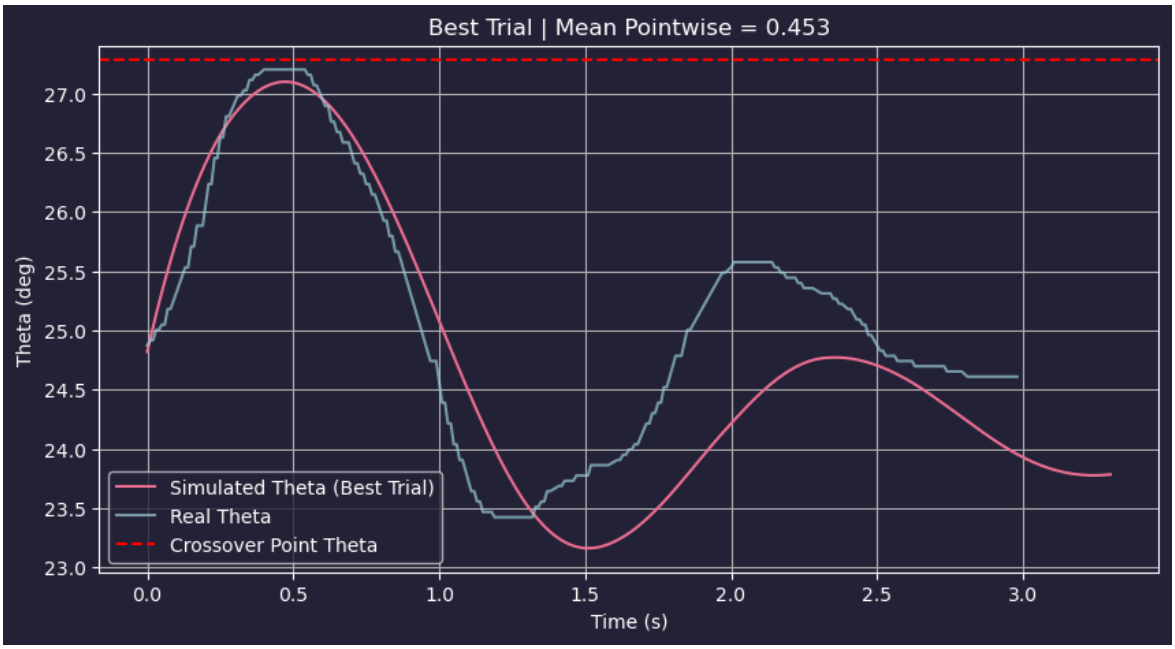

Figure 4.13: An early, not well fit optimization run with the old $\dot{\theta}$ impulse strategy - note the highly linear displacement trend in the first ∼0.15 seconds compared to the accelerative rise shown in the true data. In this case, the light blue data showcases the same training dataset as shown in Figure 4.12 and the magenta color shows the early simulated response.

The second and more realistic representation used an applied torque for a step response, applied for a short duration. This torque, named *torque_magnitude* within the optimizer, was added to the non-conservative forces within the Lagrangian as long as the current propagated time was less than the quantity *torque_stop_time*. These values were originally set to range between 1,000 and 100,000 in-lbs and between 0.05 and 0.5 seconds to get initial perspective of realistic range. Early in the optimization process the torque bounds were shifted upwards, with the final values for Figure 4.12 resting at $\sim$ 165,000 in-lbs for $\sim$ 0.22 seconds.

A set of notable characteristics can be seen from this figure. First, one can notice that the initial point at time = 0 is slightly higher than the steady-state finishing point in the dataset. This is a commonality seen across each run in the dataset varying in magnitude as can be seen in the later

variations of the test data. This is very likely due to stiction in the VERTEX suspension system. That is, the swingarm holding at a set angle after being positioned with the linear actuator and then under dynamic loading settling in a slightly different position due to friction force irregularities. In the propagated curve, the displacement curve over time shows a similar characteristic as a result of the way bushings are handled. When the model is initialized the initial preload in the bushings is 0 and in effect the system ”settles in” to the steady state point after a period of time. The effective stiffness of the bushings and the yellow circumferential strap was identified from the optimization found in Figure 4.12 to be $\sim$ 3,800 lb/in.

Additionally, the recorded curves are not as smooth as they might be in an ideal case. This is likely due to a combination of noise in the encoder measurement and inconsistencies in system damping characteristics. While the dataset for Figure 4.14 is relatively smooth, 4.15 highlights this inconsistent quality. This is part of the decision to focus on matching characteristics of the curve like rise time and bandwidth as the evaluative approach rather than focusing on hyper-alignment with the datapoints.

The second peak in this training set has been difficult to match over time. This was the primary source behind the integration of the nonlinear damping sources and is the primary reason this dataset was selected as the training data. As shown later in the test data in Figure 4.14, the equations can match very closely to more traditional single-period data points, but the 1.5 cycle graph in the test data presents an additional challenge in low-speed damping variation. In the duration between the trough and the second peak in the training data the damping of the system appears to have a significant reduction and re-activation. It was this portion of the graph that inspired the use of the nonlinear damping equations within the Lagrangian as described earlier in section 3.3.5, and it was the hysteresis in the force profile as shown in Figure 4.2 that led to the

velocity-direction dependent split within the damping equations. Although these characteristics were not able to fully represent the friction characteristics within the rover, as evidenced by the digression between the true and simulated data towards the tail-end of the graph, they still provided a significantly improved fit when compared to earlier parameter fits like shown in Figure 4.13. Friction modeling in robotics is notoriously difficult, and this difficulty is compounded in BioBot with its combination of damping sources and inconsistent damping coefficient behaviors as a function of the swingarm angle. It is suspected that the variances in the system's stiction properties are closely tied with these coefficient variations. To improve the prediction a significant testing campaign would be needed to characterize the damping coefficient behaviors, as discussed later in Chapter 5.

The alignment shown between the simulated and real data in Figure 4.12 was accepted as of-quality to progress to the test data scenarios. A significant majority of the curve matches the training data well in the beginning of the data, and begins to diverge in the tail section due to the suspected damping irregularities.

The best set of identified parameters can then be applied to a different set of impulse responses to test the closeness of the model to the real system. To accomplish this, an optimization code was set up, again using the Ray package in Python, to carry over all damping and bushing parameters from the lowest-loss configuration and optimize over a space of *torque_magnitude* and *torque_stop_time* to most closely match each test scenario. This significantly reduced search space translated to a significant reduction in the required iterations to reach a "best fit" convergence on the order of ~ 250 using a Bayesian optimization scheme.

Figure 4.14 shows the test criteria for a different impulse response recorded at a different steady-state swingarm angle. In this scenario, the swingarm begins at a lower angle, indicating the

chassis was positioned higher in this test than in the training data. This test data shows a system response at 1 cycle, as opposed to the 1.5 cycles from the training data, and by visual inspection appears to have more consistent damping than the training data. The propagated displacement closely matches the recorded data, especially early in the cycle. The difference in steady-state position at the tail of the curve is most likely due to varied stiction within the suspension.

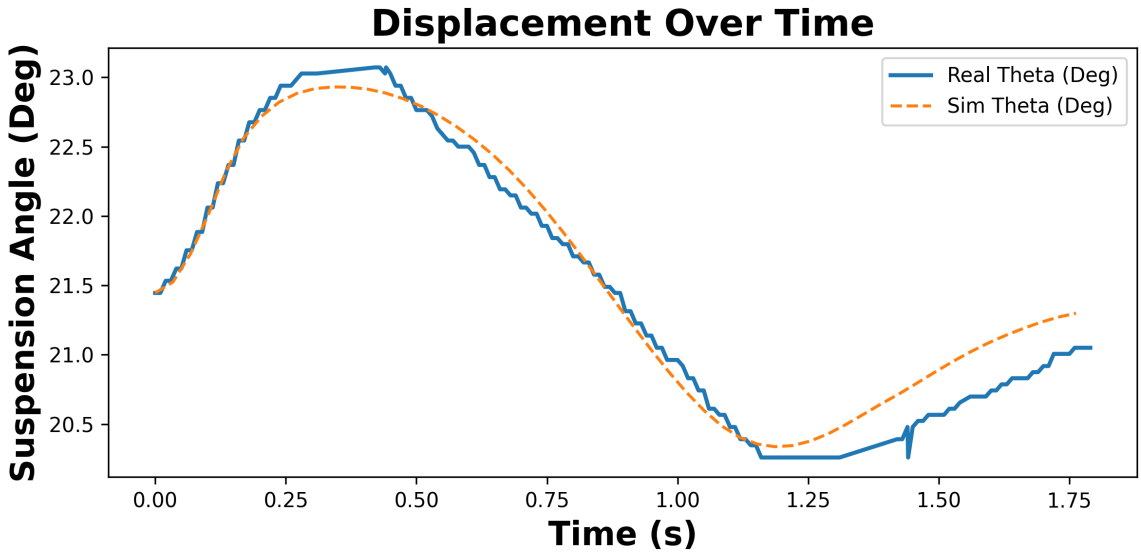

Figure 4.14: Test data run using same settings as identified in Figure 4.12, with parameter-based optimization for the step impulse magnitude and duration.

Figure 4.15 identifies a recorded run only with partial data stored in the datalogger. As the vehicle is on its way to fully autonomous capabilities, it may become important for the overarching controllers to have the ability to accurately predict the response of the suspension and reacting prior to undesired motion. While the actuation systems presently on the vehicle are low-bandwidth and likely have little potential to influence dynamic motion, upgraded linear actuators are a relatively simple upgrade to perform. This test aimed to use the model to predict what the suspension response looked like in a different dataset than those shown prior, using only the partial data available. This partial data is likely due to an issue in the ROS-based datalog-

ging software or in the encoder hardware, although data drops like this were an exceedingly rare phenomenon.

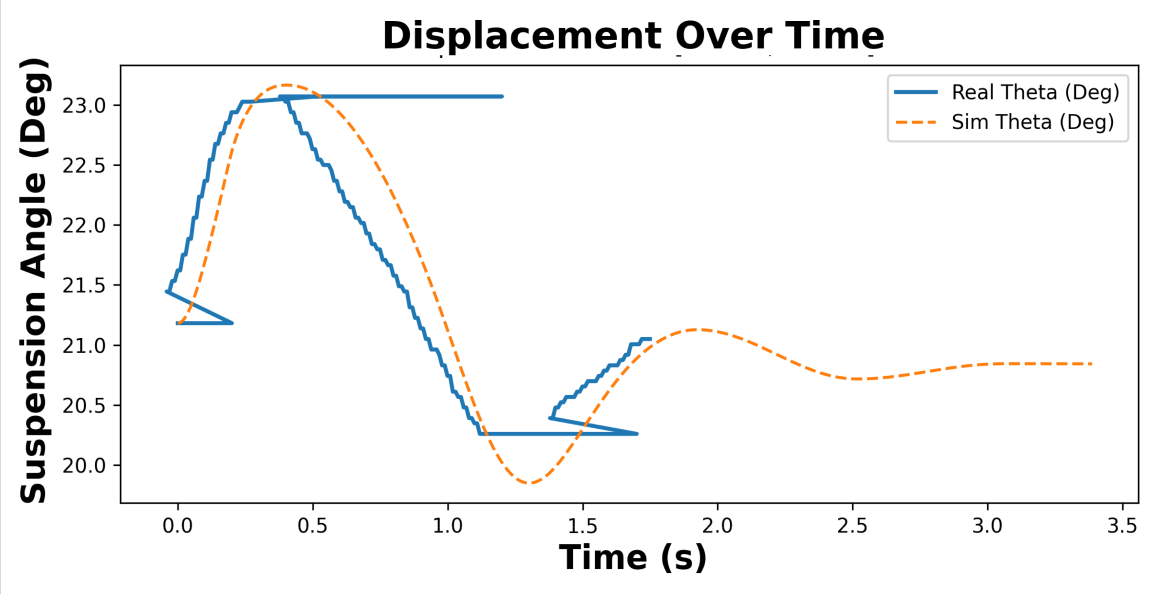

Figure 4.15: Curve match to a set of partial dataset recovered from a run

The set of Lagrangians that preserve the full set of system nonlinearities take exceedingly long to propagate (on the order of 600-800 seconds per iteration in Python) when compared to real-time requirements. However, as discussed later in Chapter 5, linearization of the system about small displacements and starting angles will allow for significantly accelerated calculations especially when using a compiled language.

In the two previous test examples (Figures 4.14 and 4.15), the simulated dataset was able to closely match to the test data especially in the early segments of the data. Figure 4.16 presents a test data set in which the model did not match closely between the prediction and reality. The damping ratio of the real system appears to be decreased between each of the peak and troughs shown in this dataset compared to the earlier plots as the first peak is well-matched in the simulated data, but decays too quickly as time approaches the first trough. The period of the

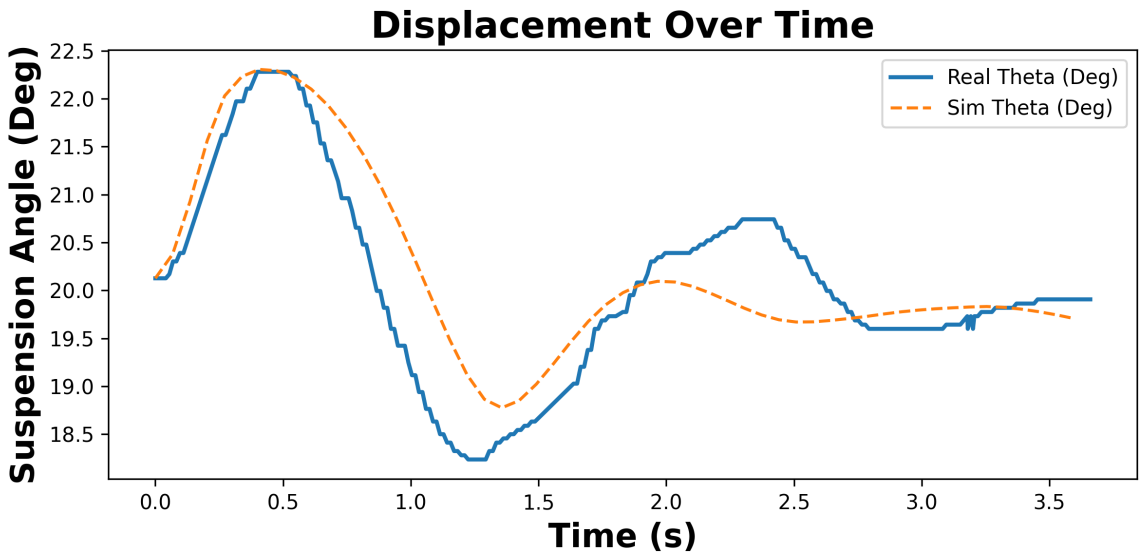

Figure 4.16: A third test dataset showing limitations of the model's ability to match to recorded curves, indicating further investigation into the nonlinear damping characteristics is needed.

curves appears to be very close for approximately the first cycle but becomes offset as the time progresses.

This indicates that further research into the variances of the damping characteristics of the vehicle is needed to better match the predicted curves with all recorded training data sets. Many factors likely affect the damping characteristics, and the true damping coefficients are likely not a set of constants but rather functions dependent on items such as swingarm angle, dual-rate spring forces, and bushing characteristics. Future studies should focus on characterizing these dynamic variabilities and integrating them into the model, thereby enhancing its predictive capacity and real-time applicability for advanced control strategies.

4.1.4 ML-Based Optimization

The machine learning framework created in section 4.1.2 can also be used to improve the suspension. Given a limited set of parameters to adjust like preload, crossover, and spring rates

(i.e. easily-tuned items, unlike re-welding structural pivots), the parameter set can be adjusted to either match an intentionally designed curve or fit within a set of evaluative criteria. To limit the network in its ability to change parameters, a green list of adjustable values was created, and any value not on the list was set to *param.requires_grad = False*.

If a mission, EVA, or design requires a specific force profile for the suspension that is realistically possible within the suspension (careful to consider realistic combinations of preload and crossover as they are both interlinked to each other and tied closely with the spring rates), then the same loss function as outlined earlier can be used to find the desired set of parameters to match the force curve. Alternately and perhaps more realistically useful, an approach could be used with a new loss criterion focused on the end-goal performance of the system. A set of criteria was created to encourage the model to push the force profile into areas that reduced limitations seen in the original suspension settings used for the previous plots. The first criteria aimed to decrease the force seen at maxima and minima as it was seen that the elastic-element was near compression when at low θ angles, and it was suspected at high θ angles that the linear actuator was experiencing excessive tension. To accomplish this, bounds were set at the existing maxima and minima points to introduce a heavy loss for extending beyond these bounds, alongside an added loss for the mean squared error around the 0-force line. Secondly, the linearity of the system was evaluated using the coefficient of variation (CV)and a ratio of coefficients using a quadratic fit. The CV calculated as the ratio between the standard deviation of the slope and the slope average.

$$\Delta x_i = x_{i+1} - x_i, \quad \Delta y_i = y_{i+1} - y_i, \quad i = 1, 2, \ldots, N-1$$

$$s_i = \frac{\Delta y_i}{\Delta x_i}, \quad i \in \mathcal{V} \quad \text{with} \quad |\Delta x_i| > \epsilon$$

$$\bar{s} = \frac{1}{n} \sum_{i \in \mathcal{V}} s_i, \quad n = |\mathcal{V}|$$

$$\sigma_s = \sqrt{\frac{1}{n} \sum_{i \in \mathcal{V}} (s_i - \bar{s})^2}$$

$$\text{CV}_s = \frac{\sigma_s}{|\bar{s}|}$$

A quadratic equation $y = a_2 x^2 + a_1 x + a_0$ is fit to each dataset and the ratio of the a_2 and a_1 coefficients is calculated $Q = \left| \frac{a_2}{a_1} \right|$. Lastly, to avoid the controllability issues seen around the 0-force transition point (between tension and compression), the curve was given a bias penalty evaluating whether the majority of the curve was sitting above or below the 0 point. Ideally, the 0-force crossing point would be at one end of the force curve to avoid uncontrollability issues in the transition regime.

The beginning set of spring rates in the dual rate damper included a 200 lb/in top rate, 400 lb/in bottom rate. Starting with these values and letting the network work to minimize the evaluation criteria, an interesting result came to light. As Figure 4.17 shows, the final solution when the spring rates were allowed to vary was an inversion in the stiffness order of the springs. The top spring rate was increased and the bottom reduced, effectively reversing the typical spring setup found in most off-road dual-rate dampers. The stiffer rate at the bottom is traditionally used to help prevent the damper from bottoming out at full compression under very high levels

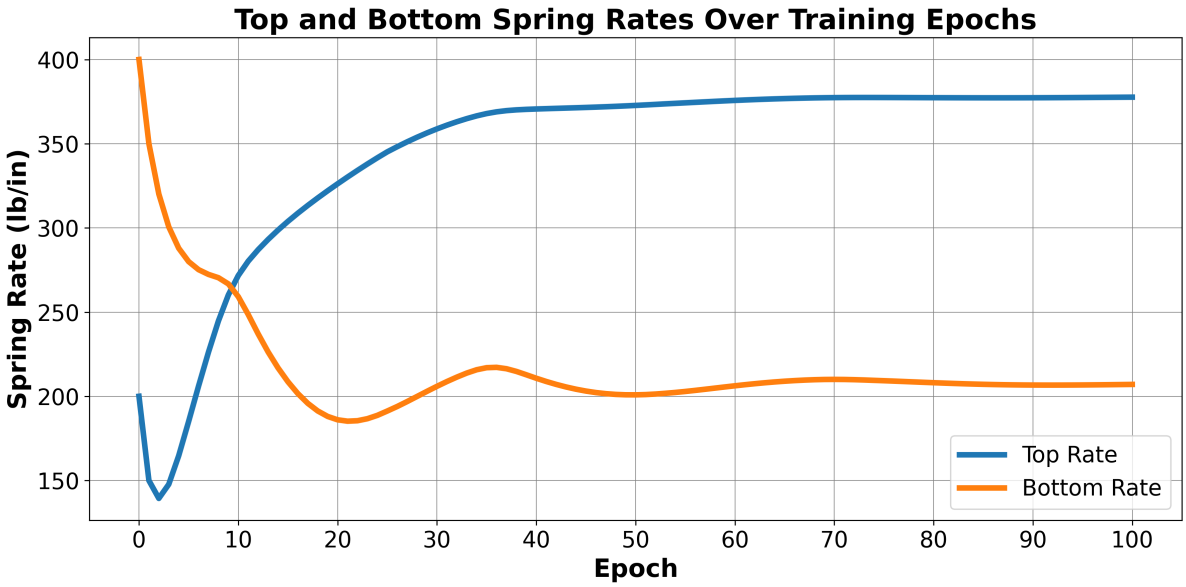

Figure 4.17: Spring rates over epochs during setting optimization run

of dynamic loading.

The final rates suggested by the network were approximately 207 lb/in bottom rate, and 377 lb/in top rate. The SSL has available to it at the present sets of 150, 200, and 400 lb/in springs, and at only a 3.5% decrease in the desired bottom rate, and a 6.1% increase in stiffness for the top rate, the dampers were disassembled, re-lubricated, and re-assembled with the same springs as before but now in the ”inverted” configuration.

The load cell was reintegrated on the front right side of the rover just as before, with the new settings and plotted against the force curve from the old settings, as shown in Figure 4.18. The new settings are capable of providing a reduction of 15. 2% in the maximum tension force, a reduction of 20. 4% in the maximum compressive force, and was able to reduce the average slope of the system by 23.9%. The coefficient of variation was reduced to 42.2% of its original value and the quadratic ratio was reduced by an order of magnitude, signifying a significantly linear response.

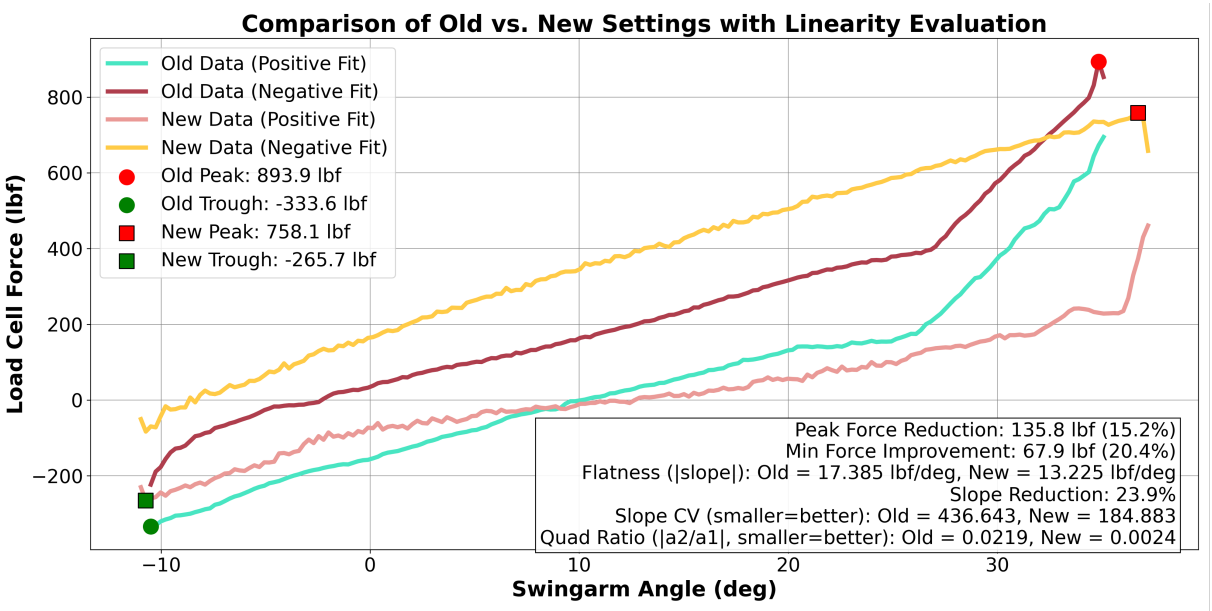

Figure 4.18: Improved force profile from ML-output settings plotted with the maxima and minima of the old settings

This is a significant improvement in the force profile of the suspension system that is expected to provide a much more comfortable, less stiff, ride for test subjects alongside being more adaptable to tuning the upcoming control schemes in the newest version of the rover's software.

Chapter 5: Conclusions and Future Work

5.1 Contributions

In the process of this dissertation, three main contributions were created. The first was the computationally efficient sum-of-moments framework used for high-level suspension design. This approach allowed for the re-design of a non-stable suspension system into one capable of supporting large payloads in any quasi-static chassis orientation. This allows for a relatively easy first step in the design of articulated suspension systems that need to include passive spring damping. Central to this approach is the 'full-contribution assumption', allowing moment-sum graphs to be easily inspected to find unstable configurations alongside providing a relative gauge for the system stiffness.

The second was the development of the Lagrangian in a manner sensitive to real-world considerations like damper limitations, tension/compression boundaries, and effects of bushings and limiting strap stiffness within a highly nonlinear suspension system. The deployed approach used combinations of Heaviside functions and separated piecewise equations of motion to consider different characteristics or system states, and when fit to real data show a strong pathway to alignment and predicting system behavior.

The last approach focused on system identification and improvement using highly efficient optimizers found within the machine learning field. The approach used a quasi-static analysis

as a baseline, and leveraged the ability of ML-approaches to overfit to data, usually seen as a characteristic to avoid, to hone in on deficiencies in the original modeling approach and identify system parameters. The same approach was then reversed to identify more optimal settings from a set of goal criteria, resulting in a force profile with greater linearity and lower force extrema.

5.2 Lessons Learned

The most impactful lesson learned in the process of creating BioBot was the element of adjustability, especially in the suspension design. The original suspension design did not have adjustment to compensate for any deviations from modeled performance or increase in subsystem masses, such as electronic components or wiring weight estimates. Not only did the upgraded dual-rate springs allow for a more stable system, but at extremely heavy payloads where the suspension would be unstable the preload or crossover can be adjusted on the fly to compensate. Further adjustment by replacing the series-elastic element with an adjustable single-rate damper like discussed in Chapter 2 would allow for even greater customizability in the suspension response profile.

The reconfigurability designed into the angle adjustment system (the system that completes the triangle between the swing arm and the steering actuator as shown in Figure 4.7) allowed the team to adjust with a variety of swingarm configurations and ride heights. Ultimately, this was set to its minimum-retraction setting to lower the ride height as much as possible at 0° caster angle, and is one example of the benefits of modularity.

An area that worked well in the design process was the establishment of key parameters early in the design process. Establishing the overall size of the vehicle, the mounting points of the

swingarms, the lengths of the swingarm, and the dimensions of the chassis allowed the initialization of manufacturing efforts to begin in the early design. The team faced significant challenges in efficiently delivering a working prototype within a university-level budget and the 3-year time frame. Establishing these ”hard points” in the design early helped allow the design and fabrication phases to progress largely in parallel, with manufacturing occurring slightly behind design as is common in the automotive industry. Placing a larger, more intentional focus on establishing these points earlier in the design process may have allowed for an even faster timeline.

The testing methodology the team used throughout the vehicle build process played a crucial role in discovering true system performance and any deficiencies early in the design process. The team followed standard engineering practices within each subsystem to verify each actuation system could perform its required task and validate it resulted in the desired vehicle control. An example of this was in the first suspension system, where early in the build it was verified to actuate through the desired range of motion and validated to successfully articulate to its 30° chassis compensation requirement, but with inconsistent payloads. Executing this test required creating specific hardware such as stand-in steering actuator structure as the steering design had not yet been completed. This allowed the vehicle to support its own weight and required additional design and machining effort that did not contribute to the final rover design, but doing so allowed for a significantly earlier detection of the suspension issue. Bowden's law states *”Following a testing failure, it's always possible to refine the analysis to show that you really had negative margins all along.”* [81]. Test early, test often, test more often than that.

5.3 Future Work

These steps serve as a foundation for future improvement. This work would specifically benefit from a test campaign focused on individualized characterization of the friction and damping profiles within each subsystem. This would require advanced machinery such as shock dynamometers and a series of friction tests within the bushings and bearings at different loads. To improve the overhead on the computation side, linearization of the equations may be advantageous for specific regimes. For example, the equations could be linearized at the 0° caster angle of the suspension system. It is likely that in doing this it would be required to still preserve some elements of the piecewise approach to compensate for the tension/compression transition in the elastic element, and if the linearized point lies near the crossover point for the dual-rate dampers.

Articulated suspension systems with passive spring damping properties are an expanding niche in the rover design space. Astrolab's FLEX rover notably features a large articulation range and is one of 3 Lunar Terrain Vehicle providers currently designing the next generation of rovers to explore the surface of the moon. There are other applications for this category of suspension design on Earth. Rock crawling off-road vehicles may very well benefit from the guaranteed stability margins that chassis articulation can provide to access terrain currently considered "impassible", and there may be approaches to other mountain-conquering vehicles in forests or snow.

In recent developments, the automotive industry has employed interesting applications of articulated suspension. Front-axle lift systems commonly use a hydraulic cylinder between the spring and the upper shock mount to effectively change the top point of the shock absorber to move low cars over speed bumps and up curbs safely. Companies like Porsche have adapted

this technology for 4-corner-independent control of the chassis positioning at higher speeds. Although this area does not have a need for non-linear analysis, the integration of fully independent suspension control in the automotive world will be interesting to watch as the integration matures. In addition, off-road motorcycles have seen the use of independently adaptable suspension. Most notably, BMW's Gelände/Straße (GS) newest motorcycle utilizes an oil-based adjustable spring system, allowing for computer controlled adjustments of the suspension's effective spring rate, allowing for changes in vehicle height and high-bandwidth terrain response. This technology has great potential in applications like VERTEX where a high-bandwidth adjustable spring rate could alleviate some of the design and response challenges observed.

Articulated suspension systems are poised to play a transformative role in the upcoming lunar and Martian exploration and habitation campaigns. Active articulation will allow rovers to guarantee stability margins on extreme slopes, precisely manipulate payloads for the extensive logistics anticipated, and dynamically adapt to challenging terrain, all while maintaining the benefits in reducing noise, vibration, and harshness due to the inclusion of passive spring damping. BioBot leverages the articulated suspension system in the form of an EVA support vehicle. Through offloading high-weight life support equipment required for operations in gravity fields such as Mars, BioBot aims to enable less strenuous and extended durations of exploration activities for astronauts. The next step for BioBot is to continue its evaluation campaign, ramping up to high-fidelity simulations like the Desert RATS (Research and Technology Studies) or Haughton-Mars Project (HMP) field tests. True evaluation of the degree of improvement that BioBot can provide to an astronaut and where the minima knee in the PLSS curve lies will be foundational elements in EVA planning in looking towards Mars.

BioBot is greater than the sum of its individual parts —

it's an eclectic research vehicle navigating to the next era of human exploration

(with a very level chassis).

Figure 5.1: BioBot.

A.1 Suspension Parameters

The parameters used to define the VERTEX suspension classes can be found in the tables below.

Table 1: Parameters used for the `Rover` class.

Parameter	Unit	Description
`name`	–	Identifier for the suspension setup
`sprung_mass`	lbs	Total rover sprung weight
`sprung_mass_xy`	in	2D offset of sprung weight from frame 0
`unsprung_mass`	lbs	Unsprung weight, per wheel
`chassis_size`	in	Overall chassis size [width, length]
`swingarm_length`	in	Length of the swingarm from pivot to tip
`swingarm_dia`	in	Outer diameter of the swingarm tube
`swingarm_ID`	in	Inner diameter of the swingarm tube
`swingarm_mass`	lbs	Weight of the swingarm
`swingarm_range`	rad	Swingarm angular travel range [min, max]
`over_wheel_steering_length`	in	Over-wheel steering linkage length
`caster_angle`	rad	Caster angle of the steering axis
`upper_bushing_rate`	$\frac{\text{lbf}}{\text{in}}$	Rate of the upper hard stop
`upper_bushing_damp_pos`	$\frac{\text{lbf}\cdot\text{s}}{\text{in}}$	Damping coeff. of upper hard stop (+ vel)
`upper_bushing_damp_neg`	$\frac{\text{lbf}\cdot\text{s}}{\text{in}}$	Damping coeff. of upper hard stop (- vel)
`planet_g`	–	Gravity fraction
`wheel_radius`	in	Radius of the wheel
`pivot_friction_Fs_pos`	lbf	Static friction force (+ direction)
`pivot_friction_Fc_pos`	lbf	Coulomb friction force (+ direction)
`pivot_friction_vs_pos`	rad/s	Stribeck velocity (+ direction)
`pivot_friction_sigma_pos`	–	Stribeck parameter sigma (+ direction)
`pivot_friction_delta_pos`	–	Stribeck parameter delta (+ direction)
`pivot_friction_Fs_neg`	lbf	Static friction force (- direction)
`pivot_friction_Fc_neg`	lbf	Coulomb friction force (- direction)
`pivot_friction_vs_neg`	rad/s	Stribeck velocity (- direction)
`pivot_friction_sigma_neg`	–	Stribeck parameter sigma (- direction)
`pivot_friction_delta_neg`	–	Stribeck parameter delta (- direction)

Table 2: Parameters used for the `Prismatic_SEA` class.

Parameter	Unit	Description
`name`	–	Identifier for the suspension setup
`min_length`	in	Minimum permissible length of the SEA
`max_length`	in	Maximum permissible length of the SEA
`spring_constant`	$\frac{\text{lbf}}{\text{in}}$	Spring constant of the SEA
`damping_coeff_SEA_exp_pos`	$\frac{\text{lbf}\cdot\text{s}}{\text{in}}$	Exponential damping coefficient (positive velocity)
`damping_coeff_SEA_exp_neg`	$\frac{\text{lbf}\cdot\text{s}}{\text{in}}$	Exponential damping coefficient (negative velocity)
`damping_coefficient_SEA_pos`	$\frac{\text{lbf}\cdot\text{s}}{\text{in}}$	Damping coefficient for positive velocity
`damping_coefficient_SEA_neg`	$\frac{\text{lbf}\cdot\text{s}}{\text{in}}$	Damping coefficient for negative velocity
`SEA_bushing_rate`	$\frac{\text{lbf}}{\text{in}}$	Rate of the bushings in SEA system
`SEA_bushing_damp_pos`	$\frac{\text{lbf}\cdot\text{s}}{\text{in}}$	Damping of the SEA bushings (positive direction)
`SEA_bushing_damp_neg`	$\frac{\text{lbf}\cdot\text{s}}{\text{in}}$	Damping of the SEA bushings (negative direction)
`spring_preload`	in	Preload length of the SEA spring
`uncompressed_length`	in	Uncompressed length of the SEA in the VERTEX suspension
`pivot_springSide`	in	[x, y] from pivot to SEA spring-side mount
`pivot_actSide`	in	[x, y] from pivot to SEA actuator-side mount
`pivot_mount`	in	[x, y] offset of the pivot point
`lower_spring_mount_xy`	in	[x, y] from swingarm pivot to lower SEA spring mount
`actuator_mounting_point`	in	[x, y] along the swingarm for actuator mount

Table 3: Parameters used for the `Gravity_Offset_Spring` class.

Parameter	Unit	Description
`name`	–	Identifier for the suspension setup
`spring_constants`	$\frac{\text{lbf}}{\text{in}}$	Array of stacked spring constants [upper, lower]
`spring_lengths`	in	Lengths of each spring in the dual-rate system
`preload`	in	Preload applied to the GO springs
`rate_changeover`	in	Crossover point for dual-rate transition
`chassis_mounting_point`	in	[x, y] from swingarm hub to chassis mount of damper
`swingarm_mounting_point`	in	[length down arm, height above centerline] for lower spring mount
`uncompressed_length`	in	Free (uncompressed) length of the damper
`GO_damping_coefficient_pos`	$\frac{\text{lbf}\cdot\text{s}}{\text{in}}$	Damping coefficient for positive velocity
`GO_damping_coefficient_neg`	$\frac{\text{lbf}\cdot\text{s}}{\text{in}}$	Damping coefficient for negative velocity
`GO_damping_exponent_pos`	–	Damping exponent (positive velocity)
`GO_damping_exponent_neg`	–	Damping exponent (negative velocity)

Bibliography

[1] Charles Hanner et al. “Field Testing of Artemis Roving System Concept to Reduce On-Suit PLSS Mass \textbar AIAA Aviation Forum and ASCEND co-located Conference Proceedings”. In: *Rovers at Work: Next Generation*. ASCEND. Place: Las Vegas, Nevada. AIAA, July 27, 2024. DOI: 10.2514/6.2024-4887.

[2] Donald Bickler. “ARTICULATED SUSPENSION SYSTEM”. Pat. 4,840,394. June 20, 1989. URL: https://patentimages.storage.googleapis.com/72/87/cf/28263d265cfffd/US4840394.pdf.

[3] Brian D. Harrington and Chris Voorhees. “The Challenges of Designing the Rocker-Bogie Suspension for the Mars Exploration Rover”. In: *37th Aerospace Mechanisms Symposium*. May 1, 2004. URL: https://ntrs.nasa.gov/citations/20040084284.

[4] A.H. Mishkin et al. “Experiences with operations and autonomy of the Mars Pathfinder Microrover”. In: *1998 IEEE Aerospace Conference Proceedings (Cat. No.98TH8339)*. 1998 IEEE Aerospace Conference Proceedings (Cat. No.98TH8339). Vol. 2. Mar. 1998, 337–351 vol.2. DOI: 10.1109/AERO.1998.687920.

[5] R.A. Lindemann and C.J. Voorhees. “Mars Exploration Rover mobility assembly design, test and performance”. In: *2005 IEEE International Conference on Systems, Man and Cybernetics*. 2005 IEEE International Conference on Systems, Man and Cybernetics. Vol. 1. Oct. 2005, 450–455 Vol. 1. DOI: 10.1109/ICSMC.2005.1571187.

[6] Richard Welch et al. “Verification and validation of Mars Science Laboratory surface system”. In: *2013 8th International Conference on System of Systems Engineering*. 2013 8th International Conference on System of Systems Engineering. June 2013, pp. 64–69. DOI: 10.1109/SYSoSE.2013.6575244.

[7] Richard Rieber et al. “Planning for a Martian Road Trip - The Mars2020 Mobility Systems Design”. In: *2022 IEEE Aerospace Conference (AERO)*. 2022 IEEE Aerospace Conference (AERO). Mar. 2022, pp. 01–18. DOI: 10.1109/AERO53065.2022.9843375.

[8] Hong Liu. *An Overview of the Space Robotics Progress in China*. State Key Laboratory of Robotics and System: Harbin Institute of Technology, 2014.

[9] YouQing Ma et al. “A precise visual localisation method for the Chinese Chang’e-4 Yutu-2 rover”. In: *The Photogrammetric Record* 35.169 (2020), pp. 10–39. ISSN: 1477-9730. DOI: 10.1111/phor.12309.

[10] L. Ding et al. “A 2-year locomotive exploration and scientific investigation of the lunar farside by the Yutu-2 rover”. In: *Science Robotics* 7.62 (Jan. 19, 2022), eabj6660. DOI: 10.1126/scirobotics.abj6660.

[11] Armando Nicolella et al. “An Overview on the Kinematic Analysis of the Rocker-Bogie Suspension for Six Wheeled Rovers Approaching an Obstacle”. In: *Advances in Italian Mechanism Science*. Ed. by Vincenzo Niola et al. Place: Cham. Springer International Publishing, 2022, pp. 86–93. ISBN: 978-3-031-10776-4. DOI: 10.1007/978-3-031-10776-4_11.

[12] Zhen Chen et al. “Study on climbing strategy and analysis of Mars rover”. In: *Journal of Field Robotics* 40.5 (2023), pp. 1172–1186. ISSN: 1556-4967. DOI: 10.1002/rob.22177.

[13] A. T. Basilevsky et al. “Geologic characteristics of the Luna 17/Lunokhod 1 and Chang’E-3/Yutu landing sites, Northwest Mare Imbrium of the Moon”. In: *Planetary and Space Science* 117 (Nov. 1, 2015), pp. 385–400. ISSN: 0032-0633. DOI: 10.1016/j.pss.2015.08.006.

[14] Nicholas C. Costes et al. *Mobility Performance of the Lunar Roving Vehicle: Terrestrial Studies, Apollo 15 Results*. NASA, 1972. 92 pp.

[15] Simon Kassel. *Lunokhod-1 Soviet Lunar Surface Vehicle*. R-802-ARPA. Rand SANTA MONICA, CA. 90406: ADVANCED RESEARCH PROJECTS AGENCY, Sept. 1, 1971.

[16] Tom Lund. “Russian Soft Landers, Orbiters, and Rovers”. In: *Early Exploration of the Moon: Ranger to Apollo, Luna to Lunniy Korabl*. Ed. by Tom Lund. Springer Praxis Books. Cham: Springer International Publishing, 2018, pp. 339–362. ISBN: 978-3-030-02071-2. DOI: 10.1007/978-3-030-02071-2_12. URL: https://doi.org/10.1007/978-3-030-02071-2_12.

[17] Kyle Johnson. “High-Speed Dynamic Response for Lunar Rovers”. In: *Earth and Space*. ASCE, Apr. 2021. ISBN: 978-0-7844-8337-4. URL: https://ascelibrary.org/doi/epdf/10.1061/9780784483374.040.

[18] Cyndia Cao et al. “Actuated Suspension Tuning Characterization of the VIPER Lunar Rover”. In: *2023 IEEE Aerospace Conference*. 2023 IEEE Aerospace Conference. Mar. 2023, pp. 1–11. DOI: 10.1109/AERO55745.2023.10115796.

[19] Terry Fong. “VIPER - NASA Ames Lunar Rover Technologies”. NASA Ames, Aug. 26, 2024.

[20] D Andrews et al. *Resource Prospector (RP) - Early Prototyping and Development*. Aug. 28, 2015. DOI: 10.2514/6.2015-4460. URL: https://arc.aiaa.org/doi/epdf/10.2514/6.2015-4460.

[21] Bill Bluethmann et al. “An active suspension system for lunar crew mobility”. In: *2010 IEEE Aerospace Conference*. 2010 IEEE Aerospace Conference. Mar. 2010, pp. 1–9. DOI: 10.1109/AERO.2010.5446895.

[22] Julie Townsend and Jeffrey Biesiadecki. “Sliding Gait Algorithm for the All-Terrain Hex-Limbed Extra-Terrestrial Explorer (ATHLETE)”. In: *Volume 3: Renewable Energy Systems; Robotics; Robust Control; Single Track Vehicle Dynamics and Control; Stochastic Models, Control and Algorithms in Robotics; Structure Dynamics and Smart Structures;* ASME 2012 5th Annual Dynamic Systems and Control Conference joint with the JSME 2012 11th Motion and Vibration Conference. Place: Fort Lauderdale, Florida, USA.

ASME, Oct. 17, 2012, pp. 51–58. ISBN: 978-0-7918-4531-8. DOI: 10.1115/DSCC2012-MOVIC2012-8505.

[23] David Wettergreen et al. “Operating Nomad during the Atacama Desert Trek”. In: *Field and Service Robotics*. Ed. by Alexander Zelinsky. Place: London. Springer, 1998, pp. 82–89. ISBN: 978-1-4471-1273-0. DOI: 10.1007/978-1-4471-1273-0_14.

[24] Dimitrios Socrates Apostolopoulos. “Analytical configuration of wheeled robotic locomotion”. PhD thesis. United States – Pennsylvania: Carnegie Mellon University, 2001. 126 pp. URL: https://www.proquest.com/docview/276041474/abstract/C4434CF75F364E2CPQ/1.

[25] Paul Bartlett et al. “Design of the Scarab Rover for Mobility & Drilling in the Lunar Cold Traps”. In: (Feb. 1, 2008). DOI: 10.1184/R1/6552563.v1.

[26] Florian Cordes et al. “Design and field testing of a rover with an actively articulated suspension system in a Mars analog terrain”. In: *Journal of Field Robotics* 35.7 (2018), pp. 1149–1181. ISSN: 1556-4967. DOI: 10.1002/rob.21808.

[27] Florian Cordes et al. *An Active Suspension System for a Planetary Rover*. 2014. URL: http://robotics.estec.esa.int/i-SAIRAS/isairas2014/Data/Session%204a/ISAIRAS_FinalPaper_0061.pdf.

[28] Florian Cordes et al. “Static force distribution and orientation control for a rover with an actively articulated suspension system”. In: *2017 IEEE/RSJ International Conference on Intelligent Robots and Systems (IROS)*. 2017 IEEE/RSJ International Conference on Intelligent Robots and Systems (IROS). Sept. 2017, pp. 5219–5224. DOI: 10.1109/IROS.2017.8206412. URL: https://ieeexplore.ieee.org/document/8206412.

[29] Yue Zhu and Jiangming Kan. “Prediction of the lateral stability of a forestry chassis with an articulated body and fitted with luffing wheel-legs”. In: *Biosystems Engineering* 224 (Dec. 1, 2022), pp. 143–160. ISSN: 1537-5110. DOI: 10.1016/j.biosystemseng.2022.10.007.

[30] Zhibo Sun et al. “Optimum Design and Trafficability Analysis for an Articulated Wheel-Legged Forestry Chassis”. In: *Journal of Mechanical Design* 144.13301 (July 19, 2021). ISSN: 1050-0472. DOI: 10.1115/1.4051539.

[31] NASA. *Live From Mars Marsokhod Images*. 1997. URL: http://quest.arc.nasa.gov/lfm/background/marsoimages.html.

[32] Jan Philipp Hakenberg. “Mobility and autonomous reconfiguration of Marsokhod”. PhD thesis. Digitala Vetenskapliga Arkivet: Helsinki University of Technology, 2009. URL: https://urn.kb.se/resolve?urn=urn:nbn:se:ltu:diva-49398.

[33] Mark Maimone. *IROS’97 Planetary Rover Workshop*. Nov. 11, 1997. URL: https://www.cs.cmu.edu/~mwm/rover/iros97.html.

[34] John Bresina et al. “Increased Flexibility and Robustness of Mars rovers”. In: *5th International Syposium on AI, Robotics, and Automation in Space*. June 1, 1999.

[35] Earl Swift. *Across the Airless Wilds: The Lunar Rover and the Triumph of the Final Moon Landings*. Mariner Books, July 6, 2021. 384 pp. ISBN: 0-06-298653-8.

[36] Timothy Wasserman. “Simulation and Control of a Passively Articulated, Segmented-Body Rover”. PhD thesis. Space Systems Laboratory: University of Maryland, June 5, 2007. 94 pp. URL: https://drum.lib.umd.edu/items/abb80277-71f1-4ac7-83c3-67fa1e89c6a3.

[37] Weiping Fang et al. “Stability analysis of articulated dump truck based on eigenvalue method”. In: *IOP Conference Series: Materials Science and Engineering* 688.2 (Nov. 2019), p. 022024. ISSN: 1757-899X. DOI: 10.1088/1757-899X/688/2/022024.

[38] Huanyu Zhao et al. “Optimization of hydropneumatic suspension for articulated wheel loader based on kriging model and particle swarm algorithm”. In: *Advances in Mechanical Engineering* 10.11 (Nov. 2018). DOI: 10.1177/1687814018810648.

[39] David Rodríguez-Martínez et al. *Enabling Faster Locomotion of Planetary Rovers with a Mechanically-Hybrid Suspension*. Issue: arXiv:2307.04494. Nov. 23, 2023. arXiv: 2307.04494. URL: http://arxiv.org/abs/2307.04494.

[40] Guilin Wen et al. “A Four-Wheel-Rhombus-Arranged Mobility System for a New Lunar Robotic Rover”. In: *International Journal of Advanced Robotic Systems* 10.10 (Oct. 1, 2013), p. 370. ISSN: 1729-8806. DOI: 10.5772/56917.

[41] Alexandre Carvalho. “On multi-objective optimization of planetary exploration rovers applied to ExoMars-type rovers”. In: *ESA/ESTEC*. Jan. 1, 2011.

[42] Baichao Chen et al. “Design of a high performance suspension for lunar rover based on evolution”. In: *Acta Astronautica* 64.9 (May 1, 2009), pp. 925–934. ISSN: 0094-5765. DOI: 10.1016/j.actaastro.2008.11.009.

[43] Mahmoud Tarokh and Huy Dang Ho. “Kinematics-Based Simulation and Animation of Articulated Rovers Traversing Uneven Terrains”. In: *Robotica* 37.6 (June 2019), pp. 1057–1072. ISSN: 0263-5747, 1469-8668. DOI: 10.1017/S0263574718001431.

[44] Mohammad Reza Elhami and Iman Dashti. “Kinematics Analysis and Simulation of a Rocker Bogie Mobile Robot”. In: *ResearchGate*. International Conference on Advances in Civil, Structural and Mechanical Engineering. Vol. 2. ACSM, Oct. 19, 2015, pp. 266–271. DOI: 10.15224/978-1-63248-039-2-19. URL: https://www.researchgate.net/publication/324967753_Kinematics_Analysis_and_Simulation_of_a_Rocker_Bogie_Mobile_Robot.

[45] Chiara Cosenza et al. “Theoretical study on a modified rocker-bogie suspension for robotic rovers”. In: *Robotica* 41.10 (Oct. 2023), pp. 2915–2940. ISSN: 0263-5747, 1469-8668. DOI: 10.1017/S0263574723000656.

[46] Hong-an Yang et al. “Dynamic Rocker-Bogie: A Stability Enhancement for High-Speed Traversal”. In: *IAES International Journal of Robotics and Automation (IJRA)* 3.3 (Sept. 1, 2014), pp. 212–220. ISSN: 2722-2586. DOI: 10.11591/ijra.v3i3.pp212-220.

[47] Alexandre Carvalho Leite and Bernd Schäfer. “Planetary Rover Optimization Tool (ROT)”. In: *15th DINAME – International Symposium on Dynamic Problems of Mechanics*. Place: Buzios, Brasilien. 2013. URL: https://elib.dlr.de/80641/.

[48] A. C. Leite and B. Schäfer. “Multibody Modeling and Multi-Objective Optimization of a Six-Wheeled Steerable Vehicle and its Motion Controllers”. In: 2010. URL: https://www.semanticscholar.org/paper/Multibody-Modeling-and-Multi-Objective-Optimization-Leite-Sch%C3%A4fer/0a9281656e443b16e2d85e976f49

[49] A. C. Leite and B. Schäfer. “Mass, power and static stability optimization of a 4-wheeled planetary exploration rover”. In: *International Conference on Engineering Optimization*. International Conference on Engineering Optimization. Place: Lisbon, Portugal. 2010. URL: https://shorturl.at/UpulL.

[50] Alexandre C. Leite et al. “Parameter identification and contact modeling for planetary wheeled rovers in soft soil”. In: *IFAC Proceedings Volumes*. 16th IFAC Symposium on System Identification 45.16 (July 1, 2012), pp. 1707–1712. ISSN: 1474-6670. DOI: 10.3182/20120711-3-BE-2027.00350.

[51] Kang Wang et al. “Design of Integrated Suspension for Landing and Traveling of Manned Lunar Mobile System”. In: *2022 International Conference on Advanced Robotics and Mechatronics (ICARM)*. 2022 International Conference on Advanced Robotics and Mechatronics (ICARM). July 2022, pp. 769–773. DOI: 10.1109/ICARM54641.2022.9959652.

[52] Junyang Zhang et al. “Passive Suspension Design and Dynamics Analysis of Manned Lunar Rover”. In: *2024 10th International Conference on Mechatronics and Robotics Engineering (ICMRE)*. 2024 10th International Conference on Mechatronics and Robotics Engineering (ICMRE). Feb. 2024, pp. 155–160. DOI: 10.1109/ICMRE60776.2024.10532165.

[53] Renchao Lu et al. “Design and analysis of a high-speed planetary rover with an adaptive suspension and spring damper”. In: *Acta Astronautica* 211 (Oct. 1, 2023), pp. 827–843. ISSN: 0094-5765. DOI: 10.1016/j.actaastro.2023.07.019.

[54] Lanqing Hu et al. “Configuration design and kinematic performance analysis of a parallel wheelset suspension for a multi-wheeled pressurized lunar rover”. In: *Acta Astronautica* 217 (Oct. 22, 2024), pp. 162–180. DOI: 10.1016/j.actaastro.2024.01.013.

[55] Chiara Cosenza et al. “Spring-Loaded Rocker-Bogie Suspension for Six Wheeled Rovers”. In: *Advances in Italian Mechanism Science*. Ed. by Vincenzo Niola et al. Place: Cham. Springer International Publishing, 2022, pp. 94–101. ISBN: 978-3-031-10776-4. DOI: 10.1007/978-3-031-10776-4_12.

[56] Edgar Martínez-García and Rafael Torres-Córdoba. “4WD Skid-Steer Trajectory Control of a Rover with Spring-Based Suspension Analysis”. In: *Intelligent Robotics and Applications*. Ed. by Honghai Liu et al. Place: Berlin, Heidelberg. Springer, 2010, pp. 453–464. ISBN: 978-3-642-16584-9. DOI: 10.1007/978-3-642-16584-9_44.

[57] Baiyang Shi et al. “Performance enhancement of vehicle suspension system with geometrically nonlinear inerters”. In: *Archive of Applied Mechanics* 94.1 (Jan. 1, 2024), pp. 39–55. ISSN: 1432-0681. DOI: 10.1007/s00419-023-02502-4.

[58] Faiz Benamar and Christophe Grand. “Quasi-Static Motion Simulation and Slip Prediction of Articulated Planetary Rovers Using a Kinematic Approach”. In: *Journal of Mechanisms and Robotics* 5.21002 (Mar. 26, 2013). ISSN: 1942-4302. DOI: 10.1115/1.4023873.

[59] David P. Miller and Tze-Liang Lee. “High-Speed Traversal of Rough Terrain Using a Rocker-Bogie Mobility System”. en. In: *Space 2002 and Robotics 2002*. Albuquerque, New Mexico, United States: American Society of Civil Engineers, June 2002, pp. 428–434. ISBN: 978-0-7844-0625-0. DOI: 10.1061/40625(203)54.

[60] Feng Chen et al. “Dynamic modelling of wheeled planetary rovers”. In: *Proceedings of 2011 International Conference on Electronic & Mechanical Engineering and Information Technology*. Proceedings of 2011 International Conference on Electronic & Mechanical Engineering and Information Technology. Vol. 4. Aug. 2011, pp. 1667–1671. DOI: 10.1109/EMEIT.2011.6023421.

[61] Matteo Caruso et al. “Design and multi-body dynamic analysis of the Archimede space exploration rover”. In: *Acta Astronautica* 194 (May 1, 2022), pp. 229–241. ISSN: 0094-5765. DOI: 10.1016/j.actaastro.2022.02.003.

[62] Krzysztof Skonieczny et al. “Considering the Effects of Gravity When Developing and Field Testing Planetary Excavator Robots”. In: *Field and Service Robotics: Results of the 10th International Conference*. Ed. by David S. Wettergreen and Timothy D. Barfoot. Cham: Springer International Publishing, 2016, pp. 299–312. ISBN: 978-3-319-27702-8. DOI: 10.1007/978-3-319-27702-8_20. URL: https://doi.org/10.1007/978-3-319-27702-8_20.

[63] Y. Kuroda et al. “Mobility performance evaluation of planetary rover with similarity model experiment”. In: *IEEE International Conference on Robotics and Automation, 2004. Proceedings. ICRA ’04. 2004*. IEEE International Conference on Robotics and Automation, 2004. Proceedings. ICRA ’04. 2004. Vol. 2. Apr. 2004, 2098–2103 Vol.2. DOI: 10.1109/ROBOT.2004.1308133.

[64] Y. Kuroda et al. “Mobility performance evaluation of planetary rovers in consideration of different gravitational acceleration”. In: *2005 IEEE/RSJ International Conference on Intelligent Robots and Systems*. 2005 IEEE/RSJ International Conference on Intelligent Robots and Systems. Aug. 2005, pp. 2991–2996. DOI: 10.1109/IROS.2005.1545177.

[65] Runze Yuan et al. “An approach to simulating Lunar crewed vehicle motions on Earth using a scaled prototype with active compensation”. In: *Mechanism and Machine Theory* 182 (Apr. 1, 2023), p. 105221. ISSN: 0094-114X. DOI: 10.1016/j.mechmachtheory.2022.105221.

[66] Yansong Liu et al. “Gradeability of ‘Zhu Rong’ Mars rover based on the simulated Martian terrain”. In: *Journal of Terramechanics* 106 (Apr. 1, 2023), pp. 57–73. ISSN: 0022-4898. DOI: 10.1016/j.jterra.2023.01.002.

[67] Evan Graser et al. “Rimmed Wheel Performance on the Mars Science Laboratory Scarecrow Rover”. In: *2020 IEEE Aerospace Conference*. 2020 IEEE Aerospace Conference. Mar. 2020, pp. 1–12. DOI: 10.1109/AERO47225.2020.9172666. URL: https://ieeexplore.ieee.org/document/9172666.

[68] Olivier Toupet et al. “Terrain-adaptive wheel speed control on the Curiosity Mars rover: Algorithm and flight results”. In: *Journal of Field Robotics* 37.5 (2020), pp. 699–728. ISSN: 1556-4967. DOI: 10.1002/rob.21903.

[69] Dean B. Eppler and D. W. Ming. “Managing Science Operations During Planetary Surface: The 2010 Desert RATS Test”. In: *42nd Lunar and Planetary Science Conference*. 42nd Lunar and Planetary Science Conference. Place: The Woodlands, TX. Mar. 7, 2011. URL: https://ntrs.nasa.gov/citations/20110008120.

[70] M. Mader et al. “Geological exploration of other planets: Insights from terrestrial desert, sea, and polar field campaigns”. In: *65th International Astronautical Congress*. Vol. 6. Jan. 2014, pp. 4412–4425.

[71] Tamra George. *Lunar Surface Data Book*. Oct. 6, 2022. URL: https://ntrs.nasa.gov/citations/20220015275.

[72] Irina Troyanovskaya et al. “Static stability of articulated front loader”. In: *AIP Conference Proceedings* 2503.1 (Oct. 13, 2022), p. 050033. ISSN: 0094-243X. DOI: 10.1063/5.0099339.

[73] Dominic Jud et al. “Robotic embankment”. In: *Construction Robotics* 5.2 (June 1, 2021), pp. 101–113. ISSN: 2509-8780. DOI: 10.1007/s41693-021-00061-0.

[74] Angelo Ugenti et al. “Analysis of an all-terrain tracked robot with innovative suspension system”. In: *Mechanism and Machine Theory* 182 (Apr. 1, 2023), p. 105237. ISSN: 0094-114X. DOI: 10.1016/j.mechmachtheory.2023.105237.

[75] José Alejandro Aguirre-Anaya et al. “Optimization of a Passive Parallelogram Suspension System for a Planetary Rover Using Differential Evolution”. In: *IEEE Latin America Transactions* 19.8 (Aug. 2021), pp. 1366–1374. ISSN: 1548-0992. DOI: 10.1109/TLA.2021.9475867.

[76] Astrolab. “The bigger picture: Flex lunar rover”. In: *Engineering & Technology* 17.5 (June 2022), pp. 62–63. ISSN: 1750-9637. DOI: 10.1049/et.2022.0520.

[77] Hiroaki Inotsume et al. “FINDING ROUTES FOR EFFICIENT AND SUCCESSFULL SLOPE ASCENT FOR EXPLORATION ROVERS”. In: *International Symposium on Artificial Intelligence, Robotics and Automation in Space*. 2019.

[78] Charlie Hanner et al. “Earth-Analogue Roving System Development and Testing for Lunar Surface Exploration”. In: *ASCEND 2023*. ASCEND. American Institute of Aeronautics and Astronautics, Oct. 17, 2023. DOI: 10.2514/6.2023-4638. URL: https://arc.aiaa.org/doi/10.2514/6.2023-4638.

[79] Mathias Woydt and Rolf Wäsche. “The history of the Stribeck curve and ball bearing steels: The role of Adolf Martens”. In: *Wear* 268.11 (May 12, 2010), pp. 1542–1546. ISSN: 0043-1648. DOI: 10.1016/j.wear.2010.02.015.

[80] Bentley. *Shocks For Drivers*. June 9, 2014. URL: https://speedsecrets.com/product/shocks-for-drivers/,%20https://speedsecrets.com/product/shocks-for-drivers/.

[81] David Akin. *Akin’s Laws of Spacecraft Design*. Apr. 9, 2025. URL: https://spacecraft.ssl.umd.edu/akins_laws.html.